

UC Berkeley

UC Berkeley Electronic Theses and Dissertations

Title

Investigating Buried Interfaces and Liquid Carbon by Second Harmonic Scattering and X-ray Scattering

Permalink

<https://escholarship.org/uc/item/0sq193r7>

Author

Riffe, Erika

Publication Date

2024

Peer reviewed|Thesis/dissertation

Investigating Buried Interfaces and Liquid Carbon by Second Harmonic Scattering and X-ray Scattering

By

Erika Joan Riffe

A dissertation submitted in partial satisfaction of the
requirements for the degree of

Doctor of Philosophy

in

Chemistry

in the

Graduate Division

of the

University of California, Berkeley

Committee in charge:

Professor Richard J. Saykally, Chair

Professor Kristie Boering

Professor Roya Maboudian

Fall 2024

Abstract

Investigating Buried Interfaces and Liquid Carbon by Second Harmonic Scattering and X-ray Scattering

By

Erika J. Riffe

Doctor of Philosophy in Chemistry

University of California, Berkeley

Professor Richard J. Saykally, Chair

The chapters of this dissertation encompass two main projects. First is the study of ions and molecules at *buried* interfaces through further development of second-order nonlinear scattering spectroscopies. The goal of these studies, documented in Chapters 3-5, is to develop a more acute understanding of the role of solid-water interfaces for ocean chemistry, water purification, drug delivery, catalysis, and environmental sensors. The second project is the investigation of the liquid state of carbon using X-ray free electron laser scattering and is discussed in Chapter 6.

Chapter 1 provides a brief history of ion adsorption to the air-water interface, describing how the field of nonlinear spectroscopy has aided in the development of a general theorem, viz. that highly polarizable, weakly solvated ions have a propensity for the interface. I discuss how the techniques of Second Harmonic Generation have developed to study colloidal, buried interfaces, extending our understanding of adsorption of ions and molecules to solid-water interfaces. Finally, the investigation of the liquid state of carbon is motivated.

Chapter 2 discusses the methods used for the studies in this dissertation, starting with a general description of second-order nonlinear spectroscopy. Before detailing Second Harmonic Scattering (SHS), a review of Second Harmonic Generation is provided. The advancements in SHS techniques utilized in the remaining chapters, viz. competitive adsorption, angle-resolved SHS (AR-SHS), and polarization-resolved SHS are chronicled. Additionally, I include an introduction to Resonant Inelastic X-ray scattering (RIXS) for the purpose of probing the liquid carbon.

Chapter 3 reports a more robust picture of the adsorption mechanism for dye molecules to charged polystyrene interfaces by investigating the temperature-dependence of the SH signal. The enthalpy and entropy contributions to the free energy were separated. Despite the small changes in ΔG_{ads} across the charged polystyrene surfaces, the sign and magnitude of ΔH_{ads} changed as a function of temperature. We find that the sign of ΔH_{ads} is affected more by the charge of the surface than by the charge of the adsorbate, and attribute the sign change to different mechanisms for adsorption to charged polystyrene surfaces.

Chapter 4 extends our studies to porous colloidal interfaces, e.g. porous silica and metal organic framework (MOF) nanocrystals. We employ AR-SHS and polarization-resolved

measurements to elucidate the probable reorientation of malachite green dye as a function of concentration. I anticipate that the work in this chapter serves as preliminary data for the development of theories that explicitly describe a buried rough or porous interface.

Chapter 5 revisits the use of a competitive adsorption model for comparing the adsorption energy of non-resonant molecules to silica nanoparticles (SNP) and polystyrene beads (PSB). I find that employing the competitive displacement model with our SHS measurements permits resolving the difference in ΔG_{ads} for caffeine on SNP and PSB, which amounts to ~ 1 kcal/mol.

Chapter 6 details time-resolved RIXS and XES measurements of ultrananocrystalline diamond (UNCD) and amorphous carbon (a-C) to directly probe changes in the electronic structure of the samples following laser irradiation. However, we find no evidence of changes to the electronic structure and attribute decreases in the time-resolved intensities for a-C and UNCD to transition blocking, subsequent relaxation, and eventual ablation of the samples. A rich comparison of experimental parameters used in a multitude of X-ray spectroscopy techniques is discussed.

Acknowledgements

These acknowledgements could never represent a comprehensive list of the many thanks I owe to my family and friends for their endless support and love while I have worked towards this PhD.

First, I would like to thank my advisor, Rich. From the day I first met Rich, I knew I wanted to model my approach to science after his own. Rich, thank you for always reminding me and our group that the most important thing is to have fun. Your persistent child-like wonder for all things science continues to inspire me to keep asking questions.

Rich's guidance also supplied me with a plethora of awesome opportunities for collaboration. I am beyond appreciative that I have gotten to work alongside many talented scientists, including teams at SLAC and Berkeley. I am especially grateful towards Adrian Davey for introducing me to MOFs and their applications in chemical engineering. Moreover, I extend my gratitude to Professor Roya Maboudian, who allowed me a glimpse of applying my chemistry knowledge to real-world problems and offered fruitful discussions. To former members of the Saykally group; Walter Drisdell, Tony Rizzuto, and Craig Schwartz, thanks for coming back to visit and letting me tag along on some awesome experiments. Craig, thank you for letting me accompany you in Japan and teaching me the value of X-ray science.

To all the members of the Saykally group that I had the pleasure of crossing paths with no matter for how long, thanks for being great lab mates. Will Cole's work inspired my own and started me on the long journey of mastering second harmonic scattering. Chris Hull and Sumana Raj initiated the studies on liquid carbon. Sumana also, who briefly made me not the sole woman in the Saykally lab. Hikaru Mizuno's mentoring and friendship was paramount in helping me get started in the lab as a first year. Finally, Shane and Franky; thank you for letting me infiltrate your bro-ship. I will forever look back fondly on our time as the last of Rich's students.

Of course, none of this would have been possible without the support and friendship I was lucky enough to have at New College. My undergraduate advisor, Steve Shipman allowed me to hit the ground running as a freshman, and I haven't looked back since. To my Microwave Gang, bonds are a social construct, but ours are tangible and invaluable.

Outside of the lab, my support systems in Berkeley and in Florida have pushed me to keep going, especially when I felt I no longer could. Obtaining a PhD is a marathon, thanks for providing the motivation.

Shane and Scout, thanks for being great friends and hosts for the best parties over the years. Scout, thank you for opening your home every Wednesday night for craft night and holding me accountable for taking time for one of my passions.

Franky, thank you for being the best partner inside the lab and out. Thank you for helping me find a balance of work and fun. The experiences we have gotten to share during our time in Berkeley have been beyond meaningful to me.

To my mom, thank you for being my rock. These past years have been hard on us, but we persevered. I hope you know I feel this accomplishment is not only mine but yours. You have always been my biggest cheerleader. Thank you for instilling in me a love for learning right from the start, and always making it feel fun and exciting. Thank you for teaching me to take pride in my work. Thank you for modelling how a woman can be strong, independent, and successful all while being compassionate and kind.

Lastly, this dissertation is dedicated in loving memory to my dad, Danny Riffe, whose unwavering support throughout my academic career meant the world to me. Daddy, you always made it feel like there was nothing I couldn't do, so I did it!

Table of Contents

Section	Page
Chapter 1. Introduction	1
1.1 Brief History of Interfacial Ions	1
1.2 Surface-sensitive Nonlinear Spectroscopy	1
1.3 Studying the Colloidal Interface	2
1.4 Current Research	3
1.5 Investigations of Liquid Carbon	3
References	3
Chapter 2. Methods	6
2.1 Nonlinear Spectroscopy	6
2.2 Second Harmonic Generation	6
2.3 Second Harmonic Scattering	7
2.3.1 Competitive adsorption	9
2.3.2 Angle-resolved SHS (AR-SHS)	10
2.3.3 Polarization-resolved SHS	11
2.4 Resonant Inelastic X-ray Scattering	12
References	13
Chapter 3. Temperature-dependent Second Harmonic Scattering Evidences Different Mechanisms for Adsorption to Charged + or - Polystyrene Surfaces	15
3.1 Introduction	15
3.2 Materials and Methods	16
3.2.1 Sample Preparation	16
3.2.2 Experimental Design	16
3.2.3 Analysis Methods	17
3.2.4 Centrifuge Separation	18
3.3 Results and Discussion	18
3.3.1 MG adsorbed to (-)PSB	18
3.3.2 MG adsorbed to uncharged PSB	19
3.3.3 MG adsorbed to (+)PSB	19
3.3.4 Centrifuge Separation	20
3.3.5 Discussion	21
Supplemental Information	23
S1. Langmuir fits and linear NYS:(+)PSB	23
References	23
Chapter 4. Examining Porous Surfaces with Second Harmonic Scattering	27
4.1 Introduction	27

4.2 Materials and Methods	28
4.2.1 Experimental Design	28
4.2.2 Sample Preparation	28
4.3 Results and Discussion	28
4.3.1 Porous Silica Nanoparticles	28
4.3.2 ZIF-8	31
4.4 Conclusions	35
References	35
<i>Chapter 5. Investigating the adsorption of non-resonant molecules to buried interfaces</i>	38
5.1 Introduction	38
5.2 Materials and Methods	39
5.2.1 Experimental Design	39
5.2.2 Sample Preparation	39
5.2.3 Analysis Methods	39
5.3 Results and Discussion	39
5.3.1 Adsorption of resonant malachite green	39
5.3.2 Displacement Studies	41
5.4 Conclusions	43
References	44
<i>Chapter 6. Time-Resolved X-ray Emission Spectroscopy and Resonant Inelastic X-ray Scattering Spectroscopy of Laser Irradiated Carbon</i>	47
6.1 Introduction	47
6.2 Experimental Methods	50
6.3 Theoretical Methods	52
6.4 Amorphous Carbon	53
6.5 Ultrananocrystalline Diamond	57
6.6 Theory Results	61
6.7 Conclusions	66
References	67

Chapter 1. Introduction

Water, the universal solvent, is ubiquitous. Therefore, the importance of understanding the role of interfacial water cannot be understated. The air-water interface has garnered much interest in recent decades; specifically, the behavior of interfacial ions has been debated.

1.1 Brief History of Interfacial Ions

Currently, the most widely accepted doctrine is that large, polarizable, and weakly-solvated ions have an affinity for the water surface.^{1,2} A mechanistic picture that encompasses this concept, along with modern theories, viz., the instantaneous interface presented by Willard and Chandler, is continuously evolving along with the development of nonlinear spectroscopy experiments.³ Beyond the air-water interface, deeper understanding of adsorption of ions and molecules at water-solid interfaces is crucial for biological, environmental, energy, and catalytic applications.

Experimentally, classical ways of studying the air-water interface relied on surface tension measurements or kinetic studies of aerosols.⁴⁻⁸ More modern experiments, such as X-ray spectroscopy and scanning probe microscopy, have been employed to study aqueous interfaces.^{9,10} However, these techniques lack the surface specificity that second-order nonlinear spectroscopies provide. While, X-ray photoelectron spectroscopy supplies surface selective responses, its probe depth is determined by the kinetic energy of the expelled photoelectrons and is limited to $\sim 3\text{nm}$.¹¹⁻¹³ Eisenthal and co-workers reported the first experiments using second harmonic generation (SHG) to examine the orientation of water molecules at the air-water interface in 1988. It has since been determined that SHG and sum-frequency generation (SFG) selectively probe primarily the outermost interfacial layer, corresponding to probe depths as fine as $\sim 1\text{nm}$.

1.2 Surface-sensitive Nonlinear Spectroscopy

While vibrational SFG (VSFGS) offered important new insight on the structure of water at the interface, it didn't act as a direct probe of the ion population therein. To extend the use of nonlinear spectroscopies beyond the probing of water molecules, Petersen and Saykally developed deep ultraviolet SHG (DUV-SHG).¹⁴ Because many ions exhibit strong charge transfer to solvent (CTTS) transitions within the deep ultraviolet, DUV-SHG can act as a selective probe when the second harmonic is resonant with the CTTS transition. By directly detecting the spectrum of an ion at the interface, thermodynamic data of ions at the air-water interface were realized, e.g. Gibbs free energies of adsorption.¹⁵

By pairing temperature-dependent DUV-SHG and molecular simulations, Saykally and Geissler ascertained the mechanism for thiocyanate ion adsorption to the air/water interface to be driven by a favorable enthalpic contribution due to solvent repartitioning and an unfavorable entropic contribution from the pinning of capillary waves by the interface.¹⁶ To further develop our understanding of the thermodynamic forces that drive ions towards or away from the interface, many groups have worked towards utilizing nonlinear spectroscopies to elucidate a general mechanism for adsorption of ions at a multitude of interfaces. Again, by coupling molecular

dynamic simulations to DUV-SHG results, the Saykally group investigated the applicability of the aforementioned mechanistic picture of ion adsorption at the air-water interface to material-water interfaces.¹⁷ For the graphene-water interface, both the enthalpic and entropic contributions were reduced, resulting in a similar Gibbs free energy as that of the air-water interface, despite a qualitatively different mechanism for ion adsorption. From this study it was hypothesized that adsorption to the graphene-water interface represented a typical adsorption process to any hydrophobe-water interface.¹⁷

1.3 Studying the Colloidal Interface

One class of hydrophobe-water interfaces that has gained popularity in the literature is denoted as the *soft-matter*-water interface. *Soft matter* encompasses biological membranes, polymers, and liquid crystals. Obtaining a molecular-level appreciation of the interactions of soft-matter surfaces and interfacial water is relevant for applications such as water remediation and drug delivery. The ubiquity of soft-matter interfaces necessitates a similar approach in developing a generalized picture of the adsorption of ions and molecules. One such application, pertinent to current environmental concerns regarding the effects of microplastics in oceanic environments, considers the role polymeric micro or nano-sized plastics play as sinks of molecular pollutants. To study such systems, a way to selectively probe colloidal particles is needed.

In 1996, the Eisenthal group published the first SHG experiments on centrosymmetric particles in bulk aqueous solution.¹⁸ By adopting a scattering geometry, rather than the typical reflection geometry utilized for planar interfaces, they introduced the general approach to second harmonic scattering (SHS). Therefore, SHS acted as a probe of so-called *buried* interfaces, wherein the studied adsorbate molecules were separated by distances on the same order of the coherence length of the SH process. In 1998, it was shown that the SH signal as a function of adsorbate concentration at the colloidal interface can be fit to a Langmuir isotherm to determine the associated Gibbs free energy.¹⁹ Subsequent studies reported the first angular profiles of the SH scattered light from 1- μ m diameter colloidal polystyrene. The shape of the angular profiles was dependent on the polarization of the incident light. Yang et al. proposed that similar *angle-resolved* SHS (AR-SHS) measurements could provide a means to differentiate nonlinear contributions from the bulk and surface.²⁰⁻²⁴ Moreover, the SH signal is negligible in the forward direction and reaches a maximum at larger angles as the diameter of the particles decrease.

Indeed, it was shown that from AR-SHS experiments, the dominant nonlinear susceptibility tensor element, and thus the orientation of the adsorbate, can be determined when the correct polarization configuration is used.²⁵ Experiments that follow the scattering pattern as a function of the polarization angle of the incident light are often referred to as polarization-dependent. Kikteva et al reported on the upright orientation of malachite green spin-cast onto a planar fused silica surface as early as 2000.²⁶ A decade later, Roke and co-workers showed that this SHG method could also be extended to the study of the *buried* interface and concluded that an optimal angular range exists wherein orientational data are most accurate.²⁷ Gassin et al proved that the adsorbent

and adsorbate contributions to the signal are $\pi/2$ out of phase by analyzing the polarization-resolved SHG of MG on a silica wafer.²⁸ Therefore, SHS can be applied to elucidate the mechanism of ion and molecule adsorption to solid-water and soft-matter-water interfaces.

1.4 Current Research

To this end, the Saykally group employed AR-SHS to examine the adsorption of common molecular pollutants to a model micro-plastic surface: polystyrene microspheres. Following studies by Eisenthal and co-workers, a displacement methodology was used to probe pollutant molecules which lacked an accessible transition for resonant enhancement, viz., ascorbic acid and caffeine, providing a comparison of Gibbs free adsorption energies across the pollutants studied.²⁹ Herein, these studies are extended to answer the question of how different solid surfaces effect adsorption (Chapter 5). Additionally, temperature-resolved SHS measurements are employed to experimentally deduce the enthalpic and entropic contributions to the adsorption picture of charged interfaces (Chapter 3). There are limitations to the SHS methods mentioned above when applying them to colloidal *porous* materials e.g. porous silica microspheres and MOF nanoparticles (Chapter 4).

1.5 Investigations of Liquid Carbon

Analogous to the ubiquity of water is the ubiquity of carbon. While the gaseous and solid states of carbon have been extensively studied, the existence of liquid carbon has been a source of contention for decades, primarily due to the difficulty of preparing carbon in the liquid state. Despite this difficulty, liquid carbon is thought to be a precursor for novel carbon materials and is relevant in astrochemical systems. Laser-induced non-thermal melting has been used to drive highly ordered pyrolytic graphene (HOPG), diamond, and amorphous carbon (a-C) samples to an equilibrium liquid state. The variety of initial sample and laser conditions employed to prepare presumed liquid samples are discussed in Chapter 6. Time-resolved resonant inelastic X-ray scattering (RIXS) and X-ray emission spectroscopy (XES) were used as probes of the electronic structure of a-C and ultrananocrystalline diamond (UNCD).

References

- (1) Jungwirth, P.; Tobias, D. J. Molecular Structure of Salt Solutions : A New View of the Interface with Implications for Heterogeneous Atmospheric Chemistry. **2001**, 10468–10472. <https://doi.org/10.1021/jp012750g>.
- (2) Vrbka, L.; Mucha, M.; Minofar, B.; Jungwirth, P.; Brown, E. C.; Tobias, D. J. Propensity of Soft Ions for the Air/Water Interface. *Current Opinion in Colloid & Interface Science* **2004**, 9 (1), 67–73. <https://doi.org/10.1016/j.cocis.2004.05.028>.
- (3) Willard, A. P.; Chandler, D. Instantaneous Liquid Interfaces. *J. Phys. Chem. B* **2010**, 114 (5), 1954–1958. <https://doi.org/10.1021/jp909219k>.
- (4) Jones, G.; Ray, W. A. The Surface Tension of Solutions of Electrolytes as a Function of the Concentration. I. A Differential Method for Measuring Relative Surface Tension. *J. Am. Chem. Soc.* **1937**, 59 (1), 187–198. <https://doi.org/10.1021/ja01280a048>.

- (5) Heydweiller, A. Interdependence of the Physical Properties of Solutions. II. Surface Tension and Electrical Conductivity of Aqueous Salt-Solutions. *Ann. d. Physik* **1910**, 4 (33), 145–185.
- (6) Knipping, E. M.; Lakin, M. J.; Foster, K. L.; Jungwirth, P.; Tobias, D. J.; Gerber, R. B.; Dabdub, D.; Finlayson-Pitts, B. J. Experiments and Simulations of Ion-Enhanced Interfacial Chemistry on Aqueous NaCl Aerosols. *Science* **2000**, 288 (5464), 301–306. <https://doi.org/10.1126/science.288.5464.301>.
- (7) Hu, J. H.; Shi, Q.; Davidovits, P.; Worsnop, D. R.; Zahniser, M. S.; Kolb, C. E. Reactive Uptake of Cl₂(g) and Br₂(g) by Aqueous Surfaces as a Function of Br⁻ and I⁻ Ion Concentration: The Effect of Chemical Reaction at the Interface. *J. Phys. Chem.* **1995**, 99 (21), 8768–8776. <https://doi.org/10.1021/j100021a050>.
- (8) Hunt, S. W.; Roeselová, M.; Wang, W.; Wingen, L. M.; Knipping, E. M.; Tobias, D. J.; Dabdub, D.; Finlayson-Pitts, B. J. Formation of Molecular Bromine from the Reaction of Ozone with Deliquesced NaBr Aerosol: Evidence for Interface Chemistry. *J. Phys. Chem. A* **2004**, 108 (52), 11559–11572. <https://doi.org/10.1021/jp0467346>.
- (9) Schlesinger, I.; Sivan, U. New Information on the Hydrophobic Interaction Revealed by Frequency Modulation AFM. *Langmuir* **2017**, 33 (10), 2485–2496. <https://doi.org/10.1021/acs.langmuir.6b03574>.
- (10) Velasco-Velez, J.-J.; Wu, C. H.; Pascal, T. A.; Wan, L. F.; Guo, J.; Prendergast, D.; Salmeron, M. The Structure of Interfacial Water on Gold Electrodes Studied by X-Ray Absorption Spectroscopy. *Science* **2014**, 346 (6211), 831–834. <https://doi.org/10.1126/science.1259437>.
- (11) Lam, R. K.; Smith, J. W.; Rizzuto, A. M.; Karslıoğlu, O.; Bluhm, H.; Saykally, R. J. Reversed Interfacial Fractionation of Carbonate and Bicarbonate Evidenced by X-Ray Photoemission Spectroscopy. *Journal of Chemical Physics* **2017**, 146 (9). <https://doi.org/10.1063/1.4977046>.
- (12) Favaro, M.; Jeong, B.; Ross, P. N.; Yano, J.; Hussain, Z.; Liu, Z.; Crumlin, E. J. Unravelling the Electrochemical Double Layer by Direct Probing of the Solid/Liquid Interface. *Nat Commun* **2016**, 7 (1), 12695. <https://doi.org/10.1038/ncomms12695>.
- (13) Axnanda, S.; Crumlin, E. J.; Mao, B.; Rani, S.; Chang, R.; Karlsson, P. G.; Edwards, M. O. M.; Lundqvist, M.; Moberg, R.; Ross, P.; et al. Using “Tender” X-Ray Ambient Pressure X-Ray Photoelectron Spectroscopy as A Direct Probe of Solid-Liquid Interface. *Sci Rep* **2015**, 5 (1), 9788. <https://doi.org/10.1038/srep09788>.
- (14) Petersen, P. B.; Saykally, R. J. Confirmation of Enhanced Anion Concentration at the Liquid Water Surface. *Chemical Physics Letters* **2004**, 397 (1), 51–55. <https://doi.org/10.1016/j.cplett.2004.08.049>.
- (15) Petersen, P. B.; Saykally, R. J. Adsorption of Ions to the Surface of Dilute Electrolyte Solutions: The Jones–Ray Effect Revisited. *J. Am. Chem. Soc.* **2005**, 127 (44), 15446–15452. <https://doi.org/10.1021/ja053224w>.
- (16) Otten, D. E.; Shaffer, P. R.; Geissler, P. L.; Saykally, R. J. Elucidating the Mechanism of Selective Ion Adsorption to the Liquid Water Surface. *Proceedings of the National Academy of Sciences of the United States of America* **2012**, 109 (3), 701–705. <https://doi.org/10.1073/pnas.1116169109>.
- (17) McCaffrey, D. L.; Nguyen, S. C.; Cox, S. J.; Weller, H.; Alivisatos, A. P.; Geissler, P. L.; Saykally, R. J. Mechanism of Ion Adsorption to Aqueous Interfaces: Graphene/Water vs.

- Air/Water. *Proceedings of the National Academy of Sciences of the United States of America* **2017**, *114* (51), 13369–13373. <https://doi.org/10.1073/pnas.1702760114>.
- (18) Wang, H.; Yan, E. C. Y.; Borguet, E.; Eisenthal, K. B. *Second Harmonic Generation from the Surface of Centrosymmetric Particles in Bulk Solution*; 1996; Vol. 259, pp 15–20.
- (19) Wang, H.; Yan, E. C. Y.; Liu, Y.; Eisenthal, K. B. *Energetics and Population of Molecules at Microscopic Liquid and Solid Surfaces*; 1998. <https://pubs.acs.org/sharingguidelines>.
- (20) Yang, N.; Angerer, W. E.; Yodh, A. G. Angle-Resolved Second-Harmonic Light Scattering from Colloidal Particles. *Phys. Rev. Lett.* **2001**, *87* (10), 103902. <https://doi.org/10.1103/PhysRevLett.87.103902>.
- (21) Jen, S. H.; Gonella, G.; Dai, H. L. The Effect of Particle Size in Second Harmonic Generation from the Surface of Spherical Colloidal Particles. i: Experimental Observations. *Journal of Physical Chemistry A* **2009**, *113* (16), 4758–4762. <https://doi.org/10.1021/jp9009959>.
- (22) Jen, S.-H.; Dai, H.-L.; Gonella, G. The Effect of Particle Size in Second Harmonic Generation from the Surface of Spherical Colloidal Particles. II: The Nonlinear Rayleigh-Gans-Debye Model. <https://doi.org/10.1021/jp910144c>.
- (23) Schneider, L.; Schmid, H. J.; Peukert, W. Influence of Particle Size and Concentration on the Second-Harmonic Signal Generated at Colloidal Surfaces. *Applied Physics B: Lasers and Optics* **2007**, *87* (2), 333–339. <https://doi.org/10.1007/s00340-007-2597-7>.
- (24) Schürer, B.; Peukert, W. In Situ Surface Characterization of Polydisperse Colloidal Particles by Second Harmonic Generation. *Particulate Science and Technology* **2010**, *28* (5), 458–471. <https://doi.org/10.1080/02726351.2010.504131>.
- (25) Gonella, G.; Dai, H.-L. Determination of Adsorption Geometry on Spherical Particles from Nonlinear Mie Theory Analysis of Surface Second Harmonic Generation. *Phys. Rev. B* **2011**, *84* (12), 121402. <https://doi.org/10.1103/PhysRevB.84.121402>.
- (26) Kikteva, T.; Star, D.; Leach, G. W. Optical Second Harmonic Generation Study of Malachite Green Orientation and Order at the Fused-Silica/Air Interface. *J. Phys. Chem. B* **2000**, *104* (13), 2860–2867. <https://doi.org/10.1021/jp992728b>.
- (27) De Beer, A. G. F.; Roke, S. Obtaining Molecular Orientation from Second Harmonic and Sum Frequency Scattering Experiments in Water: Angular Distribution and Polarization Dependence. *Journal of Chemical Physics* **2010**, *132* (23), 234702–234702. <https://doi.org/10.1063/1.3429969>.
- (28) Gassin, P.-M.; Martin-Gassin, G.; Prelot, B.; Zajac, J. How to Distinguish Various Components of the SHG Signal Recorded from the Solid/Liquid Interface? *Chemical Physics Letters* **2016**, *664*, 50–55. <https://doi.org/10.1016/j.cplett.2016.09.081>.
- (29) Cole, W. T. S.; Wei, H.; Nguyen, S. C.; Harris, C. B.; Miller, D. J.; Saykally, R. J. Dynamics of Micropollutant Adsorption to Polystyrene Surfaces Probed by Angle-Resolved Second Harmonic Scattering. *Journal of Physical Chemistry C* **2019**, *123* (23), 14362–14369. <https://doi.org/10.1021/acs.jpcc.9b01146>.

Chapter 2. Methods

2.1 Nonlinear Spectroscopy

Chapters 3-5 of this dissertation discuss the use of second harmonic scattering (SHS). Throughout those chapters, development of spectroscopic techniques for addressing particular interfacial problems is discussed. To fully appreciate the complexities of new advances in SHS, a general understanding of second-order nonlinear spectroscopies is needed. Robert W. Boyd's text on Nonlinear Optics serves as a good introduction¹ In this chapter, I will reference this book often; the reader is referred to the full text for a more rigorous description.

The field of nonlinear optics was founded immediately after the demonstration of the first working laser. Generally, nonlinear spectroscopy refers to cases in which the response to light intensity incident on a material is not linear. Second harmonic generation (SHG) is a specific case in which the response scales quadratically with the intensity of the incident optical field.

In linear optics, we state that the polarization depends on the electric field strength as

$$P(t) = \epsilon_0 \chi^{(1)} E(t) \quad (2.1),$$

where $\chi^{(1)}$ is the linear susceptibility. Nonlinear optics complicates this relationship by stating that the total polarization is equivalent to a power series expansion in the applied electric field, $E(t)$.

$$P(t) = \epsilon_0 [\chi^{(1)} E(t) + \chi^{(2)} E^2(t) + \chi^{(3)} E^3(t) + \dots] \quad (2.2)$$

We can separate this expansion to consider only the second-order polarization:

$$P^{(2)}(t) = \epsilon_0 \chi^{(2)} E(t)^2 \quad (2.3)$$

Here $\chi^{(2)}$ is the second-order nonlinear susceptibility. Under the electric dipole approximation, $\chi^{(2)} = 0$ for centrosymmetric materials. This can be proven by showing that in a medium with inversion symmetry, changing the sign of the electric field term results in the following equation:

$$-P^{(2)}(t) = \epsilon_0 \chi^{(2)} [-E^2(t)]^2 = \epsilon_0 \chi^{(2)} E(t)^2 \quad (2.4)$$

$$P^{(2)}(t) = -P^{(2)}(t)$$

For this relation to hold, the second-order nonlinear susceptibility must equal 0. Only for non-centrosymmetric systems, such as an interface, in which inversion symmetry is inherently broken, is the second-order response non-zero. Because of this relation, second-order nonlinear spectroscopies are interface specific.

2.2 Second Harmonic Generation

Second harmonic generation (SHG) is one such second-order spectroscopy. Figure 2.1 shows the energy level diagram for the process. In second-order processes, two photons generate one photon at the sum of the two input frequencies. When the two incident photons are of different frequencies the process is called sum-frequency generation, but when the photons have the same frequency, $\omega_n + \omega_m = 2\omega_n$, the process is second harmonic generation.

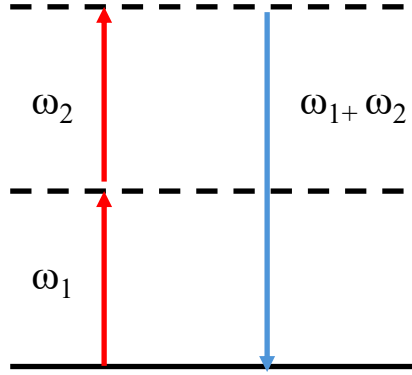


Figure 2.1. Energy level diagram for second order spectroscopy. Two incident photons with frequency ω_n , result in a single photon of frequency $\omega_{n+ \omega_m}$. The second-harmonic field is expressed by Equation 2.5.

$$E(t) = E e^{i\omega t} + E e^{-i\omega t} \quad (2.5)$$

We can incorporate the effect of this electric field on the second-order polarization by inserting Equation 2.5 into 2.3:

$$P^{(2)}(t) = 2\epsilon_0\chi^{(2)}EE^* + (\epsilon_0\chi^{(2)}E^2e^{-i2\omega t} + c.c.) \quad (2.6)$$

The first term of Equation 2.6 represents a static electric field, while the second term includes a contribution that leads to the generation of radiation at the second-harmonic frequency. For highly efficient SHG processes, nearly all the power at the input frequency is converted to radiation at twice that frequency. For the work discussed in this dissertation, the source of our incident photons is an 800 nm beam from an oscillating laser. We therefore detect the second-harmonic at half the wavelength, 400 nm. By probing molecules and ions at the interface with light that is resonant with one of the molecular transitions, SHG can be a molecule-specific spectroscopy. The frequency of light can match either the fundamental or second-order frequency to supply resonant enhancement.

2.3 Second Harmonic Scattering

Typically, an interface is studied with SHG in a reflection geometry, in which the resulting reflected second harmonic radiation is detected at an angle from a planar surface normal. This is ideal for observing gas-liquid interfaces. However, to observe colloidal solid-liquid interfaces, a transmission geometry may be used, as the second-harmonic light generated on the multi-particles interface is scattered. Wang et al. were the first to report on the ability to observe SHS from the surface of micron-sized centrosymmetric particles in solution. They observed that the nonlinear polarizations of adsorbed molecules constructively interfere, generating SH signal as long as the diameter of the particle is on the same order as the SHG coherence length.² To further prove that the signal was originating from the adsorption of molecules on the surface and not from the bulk, they utilized an adsorption isotherm. Similarly to SHG at a planar interface, the isotherm should show a quadratic dependence of the signal on the concentration of molecules adsorbed.

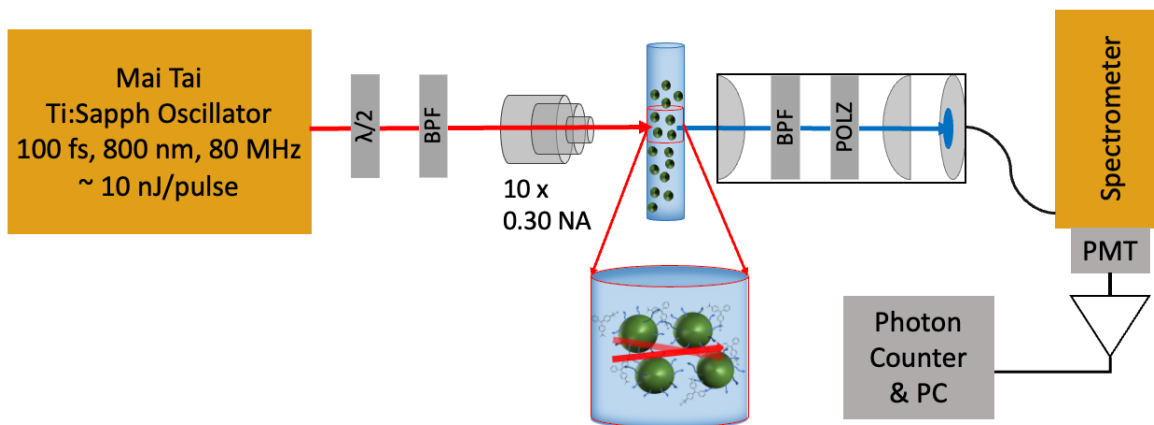
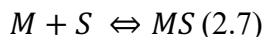


Figure 2.2. SHS setup. 800 nm light is filtered, and a half-wave plate is used to set the incident polarization. The light is then tightly focused into a vial (diameter of 4mm.) with a microscope objective. The resulting SH signal is observed with a detection arm consisting of a collimating lens, band pass filter, polarizer, focusing lens, and finally, a fiber coupler that directs the SH photons to a photomultiplier tube (PMT).

A modified Langmuir isotherm is used to determine the thermodynamics of dye adsorption to colloidal surfaces, including the free energies of adsorption. The approach makes three important assumptions about the system: it assumes no interactions occur between the adsorbates, that all sites are energetically equivalent, and that only monolayer adsorption occurs. The Langmuir model equation describes the following reaction:



The equilibrium constant for the adsorption of molecules M from the bulk to the empty surface sites S , resulting in molecules adsorbed to those sites (MS) is given by Equation 2.8:

$$K_{ads} = \frac{[MS]}{[M][S]} \quad (2.8)$$

The Langmuir equation is equivalent to expressing the fractional coverage, θ where the fractional coverage is the ratio of filled sites ($[MS]$) to the total number of sites ($[MS] + [S]$).

$$\theta = \frac{[MS]}{[S] + [MS]} \quad (2.9)$$

By solving equation 2.8 for $[MS]$ and inserting that relation into Equation 2.9, we can obtain the fractional coverage as a function of molecule concentration, $[M]$ (Equation 2.10).

$$\theta = \frac{K_{ads}[M]}{1 + K_{ads}[M]} = \frac{1}{1 + \frac{1}{K[M]}} \quad (2.10)$$

Equation 2.10 gives the classic Langmuir expression, which engenders the additional assumption that the concentration of molecules in the bulk is much larger than the concentration of molecules adsorbed to the surface. Wang et al. modify this classical Langmuir model to account for the

decrease in concentration of molecules in the bulk as they adsorb to the interface. If we express the kinetic equation for the reaction (Equation 2.7) as

$$\frac{dN}{dt} = k_1 \frac{(C-N)}{55.5} (N_{max} - N) - k_{-1} N \quad (2.11)$$

the term $\frac{(C-N)}{55.5}$ represents the bulk concentration of molecules as a mole fraction, while $N_{max} - N$ represents the number of empty sites, [S] where $N = [MS]$ and N_{max} is the number of all possible adsorption sites. From Equation 2.11, at equilibrium we can obtain the following expression:

$$\theta = \frac{N}{N_{max}} = \frac{\left(C + N_{max} + \frac{55.5}{K}\right) - \sqrt{\left(C + N_{max} + \frac{55.5}{K}\right)^2 - 4CN_{max}}}{2N_{max}} \quad (2.12)$$

The fractional coverage can then be plotted against the concentration, C and the equilibrium constant K is obtained from the fit. We can then use K to determine the Gibb's free energy of the adsorption process (Equation 2.13):

$$\Delta G = -RT \ln K \quad (2.13)$$

2.3.1 Competitive adsorption

We briefly discussed the importance of probing adsorbates that have a transition which is resonant with either the fundamental or second-harmonic frequency. This leads to limitations for the types of systems we can study with SHS. Without a resonant adsorbate, the signal from the adsorbing species is often too weak to be detected by SHS optics and detectors. To observe adsorbates, such as organic pollutants, to plastic surfaces a "competitive adsorption" method is utilized.³ Eisenthal and co-workers introduced the idea of competitive displacement as a means for using SHS techniques to study surfactants on colloidal polymer surfaces.⁴ Surfactants and pollutants often lack a chromophore and are not as highly polarizable as malachite green (MG), which is two-photon resonant in most SHG experiments. The method works by first saturating the surface with the resonant molecule (MG) and then increasing the concentration of the non-resonant molecule of interest to displace the MG. As a result, the SH signal decreases with increasing concentration of the non-resonant molecule.

The free energy of adsorption can be determined with slight changes to the fractional coverage term described in Section 2.3:

$$\theta = \frac{x}{1 + x + y}$$

$$x = K_D \times \frac{(C_D - N_{max}^D)}{55.5}, \quad y = K_C \times \frac{(C_C - N_{max}^C)}{55.5} \quad (2.14)$$

The fractional coverage relates the terms for competing molecules, K_C , C_C , and N_{max}^C , as well as those for the resonant dye molecule K_D , C_D , and N_{max}^D . This model again relies on the same assumptions as the Langmuir model discussed earlier. It is important to emphasize that the model still assumes that a single surface site may only accommodate a single species, either dye or

competitor, that these molecules are assumed to not interact with one another, and that all the surface sites are energetically equivalent.

2.3.2 Angle-resolved SHS (AR-SHS)

So far, we have discussed a simple SHS system in which the SH signal is detected in transmission geometry; however, the angle at which there is maximum SH signal is dependent on the size of the particle being probed. The maxima occur at larger angles for smaller diameter particles. Angle-resolved measurements are also unique in that they detect the SHG scattering anisotropy.^{5,6} Incident light that is s-polarized and a SH signal that is detected as p-polarized produce a scattering profile in which there is no signal at 0 degrees, or true transmission. When the SH signal is detected as s-polarized, the signal is flat. This allows for further separation of signal from the buried interface vs signal from the bulk.

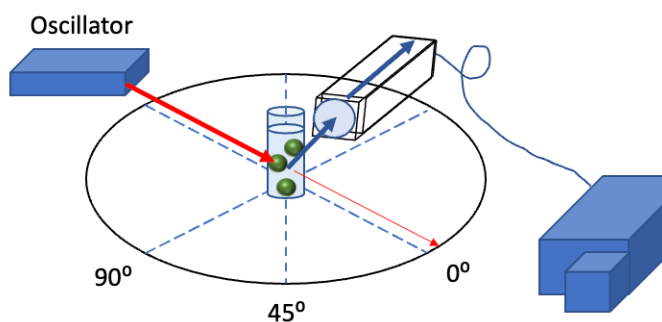


Figure 2.3. AR-SHS setup. The detection arm rotates 180 degrees around the sample vial.

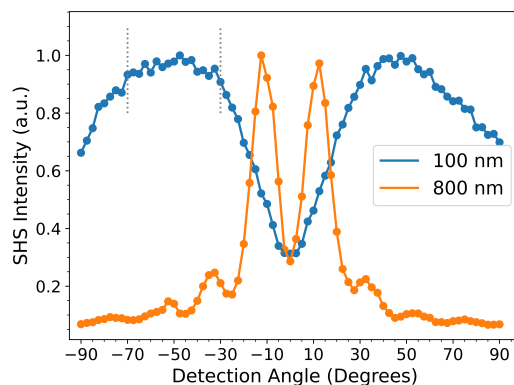


Figure 2.4. Angle-resolved scattering profile for the adsorption of MG to 100 nm (blue) and 800 nm (orange) polystyrene microspheres. The larger the particle, the closer the maximum signal is to transmission, viz. 0 degrees.

Angle-resolved measurements were automated for all the data reported in this thesis. The detection arm was set on a rotational stage controlled with a LabView script to collect the scattered signal in steps of 2.5 degrees. To obtain a free energy of adsorption for angle-resolved measurements, the signal is averaged near the maxima, for example from -30 to -70 degrees for the 100 nm data in Figure 2.4. Angle-resolved profiles are collected at each concentration and the average signal as a function of concentration is fit to a Langmuir isotherm, as described earlier in this chapter. The maxima represent the optimal angular region in which to make polarization-dependent measurements that are most sensitive to the adsorbate orientation.⁷

Angle-resolved measurements also provide information about the shape of the colloidal particles. While spherical particles produce scattering patterns that are symmetric, an ensemble of ellipsoidal particles would result in scattering patterns that are asymmetric and lose the secondary maxima peaks visible at larger scattering angles for spherical particles. Further, de Beer et al.⁸ showed the theoretically determined scattering patterns for a sphere, cylinder, tetrapod, and even a horse. The scattering patterns for the tetrapod and horse feature broadly increased intensity at higher detection angles due to the substructures (points of the tetrapod, legs of the horse) (Figure 2.5).

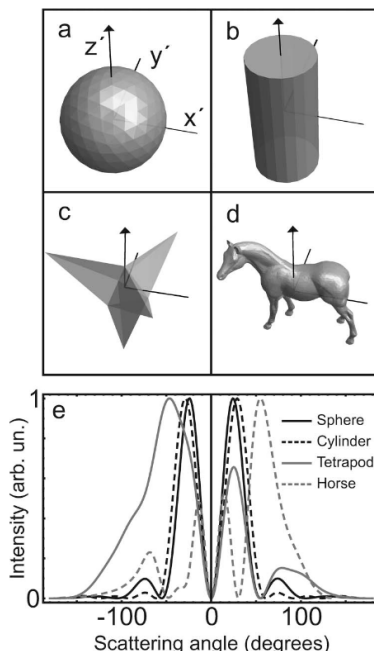


Figure 2.5. The calculated scattering patterns for (a) a sphere, (b) a cylinder, (c) a tetrapod, and (d) a horse. Reprinted with permission from Ref 8. Copyright 2011 Optical Society of America.

2.3.3 Polarization-resolved SHS

Polarization-resolved SHS can be used to simultaneously detect adsorbate molecules still in the bulk, and molecules adsorbed to these particles. Gassin et al. found that the intensity of the vertically polarized second harmonic signal can be broken down into two terms, one describing the hyper-Rayleigh scattering (HRS) of the free molecules in solution, and one describing SH signal from the adsorbed molecules.⁹

$$I^{2\omega}(\gamma, V) = I_{HRS}^{\lambda}(\gamma, V) + K_{SHS}^{\lambda} \sin^2(2\gamma) \quad (2.15)$$

Here γ is the angle of the input polarization and K_{SHS}^{λ} is proportional to $\chi^{(2)}$.

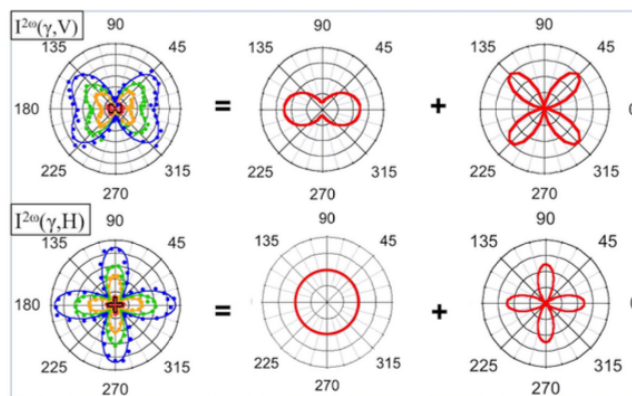


Figure 2.6. The global polarization-resolved SH signal is shown in the first column. The right hand side of the figure shows the signal decomposed into HRS and SHS from the molecules in the bulk and those adsorbed to the interface, respectively. Reprinted with permission from Ref 9. Copyright 2017 American Chemical Society.

Additionally, AR-SHS can be extended to study the orientation of adsorbates on the surface by observing the amplitudes of the scattering pattern as a function of polarization schemes. P polarized light refers to light that propagates parallel to the plane of incidence and S refers to light that propagates perpendicular to the plane of incidence. In this picture we consider the surface susceptibility $\chi^{(2)}$ as a tensor made up of the orientationally-averaged sum of the hyperpolarizability tensor, $\beta^{(2)}$ of the surface molecules (Equation 2.16).

$$\chi^{(2)} = N\langle\beta^{(2)}\rangle \quad (2.16)$$

Here N is the concentration of molecules at the interface. Gonella and Dai showed that the scattering patterns resulting from polarization-resolved AR-SHS measurements can be fit using Nonlinear Mie Theory. This analysis can be used to determine the adsorption geometry. For example, they show that MG adsorbed to a polystyrene surface is most likely standing upright, with the dimethylamino groups either facing towards or away from the interface.¹⁰

2.4 Resonant Inelastic X-ray Scattering

Resonant inelastic X-ray scattering (RIXS) and the non-resonant counterpart X-ray emission spectroscopy (XES) are photon-hungry techniques that take advantage of the recent evolution of free-electron lasers (FELs) as instruments that can supply high flux, and advantageous time and spectral resolution.¹¹⁻¹³ Both RIXS and XES are “photon-in, photon-out” techniques. This scheme differs from the more familiar picture of photoelectron spectroscopies such as X-ray photoelectron spectroscopy (XPS), in which photons are adsorbed by the material or system, and core electrons are ejected. XPS provides the binding energies, related to the energy of the incoming photon, which can be used to determine the composition, electronic structure, and chemical state of the elements. RIXS/XES differ from XPS in that an incoming photon excites an electron from a core level into an unoccupied orbital, subsequently, a valence electron decays to fill the core hole left behind by the absorption process. As energy is conserved, this results in the emission of a photon of matching energy.

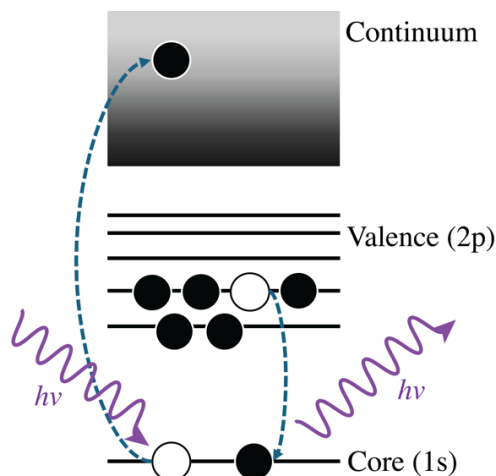


Figure 2.7. Energy level diagram for the XES process. An incoming photon excites an electron from the core (1s) into the continuum. An electron from a lower-lying valence band then relaxes to fill the electron hole. A photon is emitted.

XES therefore provides information about the occupied electronic orbitals, while RIXS spectra report on both the empty and occupied electronic states. RIXS gets the “resonant” part of its name from the resonance between the energy of the incident photon and the atomic x-ray transition being probed. XES lacks this correlation. This resonance allows for increased inelastic scattering cross-section of the x-ray photons off the sample. RIXS is unique in its ability to probe charge, magnetic, and orbital degrees of freedom, allowing for a full picture of the elementary excitations of a material. Understanding these elementary excitations dictate the understanding of a material’s physical properties. Moreover, RIXS is element-specific and bulk-sensitive.¹² In the soft X-ray regime utilized in Chapter 6, RIXS has a general probe depth of ca. 100 nm. While being photon-hungry, only small sample volumes are required due to the strength of photon-matter interactions and intensity of the FEL sources, permitting the study of surfaces and thin films, like ultranocrystalline diamond.

References

- (1) Boyd, R. W. *Nonlinear Optics*, Third edition.; Elsevier, Academic Press: Amsterdam Heidelberg, 2008.
- (2) Wang, H.; Yan, E. C. Y.; Borguet, E.; Eisenthal, K. B. *Second Harmonic Generation from the Surface of Centrosymmetric Particles in Bulk Solution*; 1996; Vol. 259, pp 15–20.
- (3) Cole, W. T. S.; Wei, H.; Nguyen, S. C.; Harris, C. B.; Miller, D. J.; Saykally, R. J. Dynamics of Micropollutant Adsorption to Polystyrene Surfaces Probed by Angle-Resolved Second Harmonic Scattering. *J. Phys. Chem. C* **2019**, *123* (23), 14362–14369. <https://doi.org/10.1021/acs.jpcc.9b01146>.
- (4) Wang, H.; Troxler, T.; Yeh, A. G.; Dai, H. L. In Situ, Nonlinear Optical Probe of Surfactant Adsorption on the Surface of Microparticles in Colloids. *Langmuir* **2000**, *16* (6), 2475–2481. <https://doi.org/10.1021/la9909087>.
- (5) Eisenthal, K. B. Second Harmonic Spectroscopy of Aqueous Nano- and Microparticle Interfaces. *Chem. Rev.* **2006**, *106* (4), 1462–1477. <https://doi.org/10.1021/cr0403685>.

- (6) Yang, N.; Angerer, W. E.; Yodh, A. G. Angle-Resolved Second-Harmonic Light Scattering from Colloidal Particles. *Phys. Rev. Lett.* **2001**, *87* (10), 103902. <https://doi.org/10.1103/PhysRevLett.87.103902>.
- (7) De Beer, A. G. F.; Roke, S. Obtaining Molecular Orientation from Second Harmonic and Sum Frequency Scattering Experiments in Water: Angular Distribution and Polarization Dependence. *J. Chem. Phys.* **2010**, *132* (23), 234702–234702. <https://doi.org/10.1063/1.3429969>.
- (8) de Beer, A. G. F.; Roke, S.; Dadap, J. I. Theory of Optical Second-Harmonic and Sum-Frequency Scattering from Arbitrarily Shaped Particles. *J. Opt. Soc. Am. B* **2011**, *28* (6), 1374–1374. <https://doi.org/10.1364/josab.28.001374>.
- (9) Gassin, P.-M. M.; Bellini, S.; Zajac, J.; Martin-Gassin, G. Adsorbed Dyes onto Nanoparticles: Large Wavelength Dependence in Second Harmonic Scattering. *J. Phys. Chem. C* **2017**, *121* (27), 14566–14571. <https://doi.org/10.1021/acs.jpcc.7b00703>.
- (10) Gonella, G.; Dai, H. L. Second Harmonic Light Scattering from the Surface of Colloidal Objects: Theory and Applications. *Langmuir* **2014**, *30* (10), 2588–2599. <https://doi.org/10.1021/la403570f>.
- (11) Park, S. H.; Yoon, J.; Kim, C.; Hwang, C.; Kim, D.-H.; Lee, S.-H.; Kwon, S. Scientific Instruments for Soft X-Ray Photon-in/Photon-out Spectroscopy on the PAL-XFEL. *J. Synchrotron Radiat.* **2019**, *26* (4), 1031–1036. <https://doi.org/10.1107/S1600577519004272>.
- (12) Ament, L. J. P.; Van Veenendaal, M.; Devereaux, T. P.; Hill, J. P.; Van Den Brink, J. Resonant Inelastic X-Ray Scattering Studies of Elementary Excitations. *Rev. Mod. Phys.* **2011**, *83* (2), 705–767. <https://doi.org/10.1103/RevModPhys.83.705>.
- (13) Qiao, R.; Li, Q.; Zhuo, Z.; Sallis, S.; Fuchs, O.; Blum, M.; Weinhardt, L.; Heske, C.; Pepper, J.; Jones, M.; et al. High-Efficiency *in Situ* Resonant Inelastic x-Ray Scattering (iRIXS) Endstation at the Advanced Light Source. *Rev. Sci. Instrum.* **2017**, *88* (3), 033106. <https://doi.org/10.1063/1.4977592>.

Chapter 3. Temperature-dependent Second Harmonic Scattering Evidences Different Mechanisms for Adsorption to Charged + or - Polystyrene Surfaces

3.1 Introduction

The mechanistic details of surface adsorption of atoms and molecules from aqueous solutions have comprised a vigorously debated subject with important environmental applications. e.g. atmospheric chemistry, water purification, electrochemistry, catalysis (“on-water”), biological processes, mineral growth.¹⁻⁴ Moreover, characterizing adsorption by *colloidal* surfaces is vital to current oceanic applications, including the roles that micro- and nanoplastics play as sinks for contaminants.⁵ While many experiments have been able to quantify the free energy of adsorption utilizing surface-specific nonlinear spectroscopies, e.g. second harmonic generation (SHG) and sum frequency generation (SFG)^{1,6-13}, few have experimentally quantified the other thermodynamic parameters (enthalpy and entropy) that permit a full mechanistic picture.^{14,15} Significantly fewer have extended the application of nonlinear techniques to elucidate the mechanistic details at buried interfaces, such as colloidal objects in aqueous environments.¹⁶

Previous studies have determined that the adsorption of thiocyanate ions to the air/water interface is driven by the repartitioning of the solvent energy. Simulations clarified that the negative changes in enthalpy and entropy observed when the adsorption process was measured by temperature-dependent UV second harmonic generation spectroscopy were microscopic in origin.¹⁴ Years later, when studying the impact of a material substrate at an aqueous interface, it was found that the free energy of adsorption of thiocyanate to the graphene-water interface was negligibly different from that of the air-water interface ($\Delta G_{\text{ads,graphene}} = -8.5 \pm 1.1$ kJ/mol and $\Delta G_{\text{ads,vap}} = -6.78 \pm 0.03$ kJ/mol, respectively).^{8,14} Once again, simulations were employed to establish the mechanism, finding that such similar adsorption free energies may not reflect a similar mechanism, but instead, revealing that the negative enthalpy resulted from a direct interaction between the ion and the polarizable graphene, while the negative entropic contributions resulted from impeding of the ion rotational motion by the graphene surface.⁸

More recently, water-liquid hydrophobe interfaces have been examined by measuring the SHG response in a reflection geometry, probing the buried interface. Again, a free energy of adsorption was determined to be within error of those reported for the water-vapor and water-graphene interfaces. However, simulations described a generalized picture of thiocyanate at hydrophobic interfaces, finding that entropic contributions dominated the adsorption process. In fact, enthalpic contributions were deemed negligible, as the loss in water hydration energy as the ion adsorbed to the oil interface is not counteracted by strong oil-ion interactions. Entropy in the system is increased as the ion travels into the oil and drags its solvation shell along, elongating capillary fluctuations into water “fingers”.⁶

Here we extend the study of adsorption processes to the solid-liquid interface by measuring the differences in enthalpy and entropy contributions during the adsorption of two chromophores to oppositely charged sub-micron diameter polystyrene beads. We utilize SHG in a scattering geometry (second harmonic generation scattering, SHGS) to probe the buried interface of the

charged colloidal polystyrene samples suspended in water. The polystyrene surface mimics an ideal spherical nano-plastic particle, a common sink for contaminants in polluted oceanic environments. Malachite green (MG) is a prototypical chromophore for second harmonic scattering experiments due to its resonance with the generated second harmonic wavelength at 400 nm.^{1,11,17-19} We have used MG as a model *cationic* dye in the adsorption to negatively charged polystyrene ((-)PSB) and previously reported on the adsorption of naphthol yellow S (NYS), a divalent *anionic* dye to positively charged polystyrene ((+)PSB), as published by Cole et al.¹ Once again, we observed a negligible change in the adsorption free energies ($\Delta G_{\text{ads, MG, nPSB}} = -10.9 \pm 0.2$ kcal/mol and $\Delta G_{\text{ads, NYS, pPSB}} = -10.27 \pm 0.09$ kcal/mol, respectively). In the present paper, we revisit these interfaces and employ temperature-dependent SHGS to quantify the enthalpic and entropic contributions to the molecular mechanism of adsorption. These results provide valuable preliminary estimates of thermodynamic parameters needed for a theoretical description of adsorption at a solid-liquid interface. Additionally, we examine the adsorption of malachite green to *uncharged* polystyrene beads (PSB) to decipher the impact of surface charge on the adsorption process.

3.2 Materials and Methods

3.2.1 Sample Preparation

All polystyrene beads were purchased from Thermo-Fisher Scientific and have a diameter of 100 nm. (-)PSB were functionalized with sulfate groups at $\text{pH} > 2$ by the manufacturer. (+)PSB are functionalized with aliphatic amine groups at $\text{pH} < 10$. The charged functional groups are responsible for a 5-10% charged surface. PSBs were not functionalized and contained no surfactants. Each polystyrene sample was prepared as a 0.03% w/w stock solution by diluting the purchased samples with ultrapure water, obtained from a Millipore Milli-Q water purification system (18.2 M Ω cm at 25 °C, 4 ppb TOC).

Malachite green (MG) and Naphthol Yellow S (NYS) were purchased from Sigma Aldrich. Stock solutions of each chromophore dye were prepared with ultrapure water and pH-adjusted using hydrochloric acid (Fisher Scientific, Certified grade).

For the temperature-dependent studies, a stock of ultrapure water, adjusted to the desired pH, was suspended in a water bath and heated to the desired temperature. Samples measured with SHS were prepared immediately before they were probed by further diluting the polystyrene solution to 0.01% w/w with the heated water and pipetting the appropriate amount of dye into the vial to reach sub-micromolar concentrations. These samples were then transferred from the vial to the sample cell in the setup before each scan.

3.2.2 Experimental Design

The output of a Ti:Sapphire oscillator (Spectra Physics Mai-Tai, 10 nJ, 80 MHz, 100 fs) centered at 800 nm is directed through a bandpass filter and half-wave plate to filter the beam and select the input polarization. The fundamental light is then focused into the sample cell by a microscope objective (10x, 0.25 NA). The sample cell (diameter = 4mm) is held at a constant temperature (+/- 0.5 degrees) by a heating cable secured at the top and base of the cell. The resulting scattered second harmonic light passes through an aperture before it is collimated, then directed through a polarizer, and focused onto a fiber coupler with a lens ($f = 38$ mm). All the optics preceding the sample cell are arranged on a rotating detection arm so that the most efficient

collection angle is achieved. In this experiment, the arm is set at 30 degrees normal to the transmission geometry. The generated second harmonic signal is directed to a PMT (Hamamatsu R212) via a fiber. The PMT is operated in photon counting mode. Each scan was collected with a counting time of 500 ms and represent the average of 240 separate collections. The average counts from 3 scans at each temperature are further averaged to improve error.

3.2.3 Analysis Methods

By fitting the relative intensity as a function of dye concentration to a modified Langmuir isotherm, the Gibbs free energy was determined. The standard isotherm used in fitting these data was first published by Wang et al:^{17,20}

$$I_{SHS} = B + [b + a \times \theta_D \times e^{i\phi}]^2 \quad (3.1)$$

The intensity of the relative SHS signal (I_{SHS}) is proportional to the fractional coverage of dye molecules (θ_D), in this case MG, and a phase factor squared. The fit constant B describes the constant non-resonant background (water), a describes the relative signal of dye molecules at the surface, and b describes any signal originating from the surface itself. Because the signal from the bare polystyrene beads in water is negligible, we set both b and the phase factor ϕ to zero, as described previously.^{1,17} We relate the Gibbs free energy (ΔG_{ads}) directly to I_{SHS} via the equilibrium constant of adsorption K_D , a value present in the fractional coverage term:

$$\theta_D = \frac{\left[(C_D + N_m^D + \frac{55.5}{K_D}) - \left\{ (C_D + N_m^D + \frac{55.5}{K_D}) - 4C_D N_m^D \right\}^{1/2} \right]}{2N_m^D} \quad (3.2)$$

The equilibrium constant describes the equilibrium state of free dye molecules (D), empty sites (S) and dye molecules adsorbed to sites (DS); here we assume single-layer adsorption:



Furthermore, C_D represents the concentration of dye in solution, and N_m^D constitutes the maximum surface number density of the dye molecule. Thus, by changing the dye concentration, we can fit the Langmuir curve and obtain values for N_m^D and K_D , the latter being used to derive ΔG_{ads} by the well-known relation:

$$\Delta G_{ads} = -RT \ln K_D \quad (3.4)$$

By fitting ΔG_{ads} as a function of temperature to a straight line, we obtain the enthalpic and entropic contributions to the mechanism of adsorption:

$$\Delta G_{ads} = \Delta H_{ads} - T\Delta S_{ads} \quad (3.5)$$

Here ΔH_{ads} , the enthalpy term, comes from the y-intercept of the line and ΔS_{ads} , the entropy, is represented by the slope.

3.2.4 Centrifuge Separation

It is not always possible to derive N_m^D values which are uncorrelated to K_D . To account for this, Eckenrode et al. utilize a centrifuge separation method that we also employ here.¹² Aliquots of MG dye and the various PSB surfaces are centrifuged for 20 minutes at 5000 rpm. The absorbance of the supernatant is observed at the MG S1 transition (~ 620 nm) and compared to the absorbance of aqueous MG at the same concentration. The difference in absorbance is used to calculate how much MG is adsorbed by the surfaces.

3.3 Results and Discussion

3.3.1 MG adsorbed to (-)PSB

We revisit the adsorption of MG to (-)PSB, previously published by Cole et al. to confirm the reproducibility of our methods and expand on the findings, supplying ΔH_{ads} and ΔS_{ads} . Figure 3.1(a) shows the calibration curve of the SHS response, which is fit to a modified Langmuir isotherm as described above. Despite outliers, we obtain a $\Delta G_{\text{ads}} = -10.83 \pm 0.11$ kcal/mol with a very small uncertainty of 0.11 kcal/mol. In fitting this data set, we found that exclusion of the data point resulted in a negligibly different ΔG_{ads} , and therefore choose to report it. Moreover, the ΔG_{ads} is within error of the value previously reported Cole et al. (-10.9 ± 0.2 kcal/mol). Figure 3.1(b) plots the line of best fit through our temperature-resolved ΔG_{ads} results. Additionally, we measured the SHGS signal intensity for the adsorption of MG to (-)PSB at two other temperatures, ~ 304 K and 321 K, and determined ΔG_{ads} values of -10.99 ± 0.28 and -11.90 ± 0.11 kcal/mol, respectively (Figure 3.1(b)). We observe that at temperatures near 304 K, the Gibbs free energy of adsorption remains within error of the room-temperature value previously reported by our group. However, at temperatures approaching 321 K, we see a decrease of around 1 kcal/mol, indicating that increasing the temperature increases the favorability of the adsorption of cationic dye to (-)PSB. The relatively large uncertainty at ~ 304 K is due to a less accurate fit to the Langmuir isotherm at that temperature.

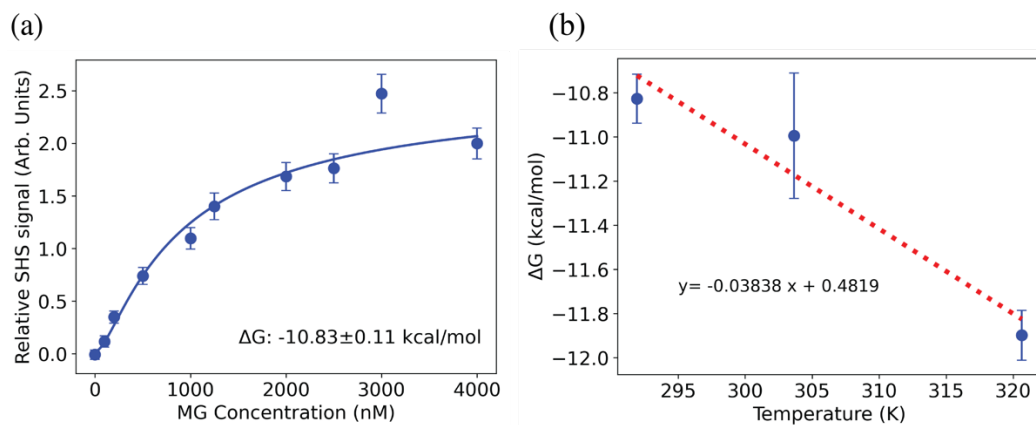


Figure 3.1. (a) Relative SHS signal as a function of the concentration of MG in solution with (-)PSB at 291 K. Error bars show the standard deviation in normalized SHGS intensity. The solid line represents the Langmuir isotherm fit. (b) ΔG_{ads} as a function of temperature. The error bars depict the uncertainty in the Langmuir fit for each temperature. The dotted red line is the line of best fit and provides ΔH_{ads} and ΔS_{ads} .

The negative slope represents a positive ΔS_{ads} of 0.0384 ± 0.0007 kcal/mol K, or ~ 160.7 J/mol K. The positive ΔH_{ads} of 0.48 ± 0.37 kcal/mol, indicates that adsorption of MG to (-)PSB is an endothermic process. The large uncertainty associated with ΔH_{ads} is a side effect of having to extrapolate the data to a $T = 0$ K. Controlling the temperature below 290 K caused condensation on the sample vial, limiting our ability to accurately determine the SHGS intensity and calculate ΔG_{ads} below room temperature.

3.3.2 MG adsorbed to uncharged PSB

We also measure I_{SHGS} , as a function of MG concentration in solution with plain (uncharged) PSB. At the uncharged surface, the ΔG_{ads} is slightly more positive (-10.19 ± 0.31 kcal/mol), and therefore less favorable than at the (-)PSB surface (Figure 3.2(a)). A decrease in favorability is expected as there are no longer charge/charge interactions between the negative functional groups on the surface of PSB and the positive charge of MG. Figure 3.2(b) shows the ΔG_{ads} for three different temperatures. The uncertainty of ΔG_{ads} is larger (~ 0.4 kcal/mol or ~ 1.7 kJ/mol) across all three temperatures relative to the uncertainty observed at the (-)PSB surface. Despite these larger uncertainties in ΔG_{ads} , the ΔH_{ads} of MG adsorption to plain PSB is still statistically different from the ΔH_{ads} of MG adsorption (-)PSB. We find that like the (-)PSB surface, the mechanism of adsorption of MG to the uncharged surface is endothermic, albeit slightly less favorable.

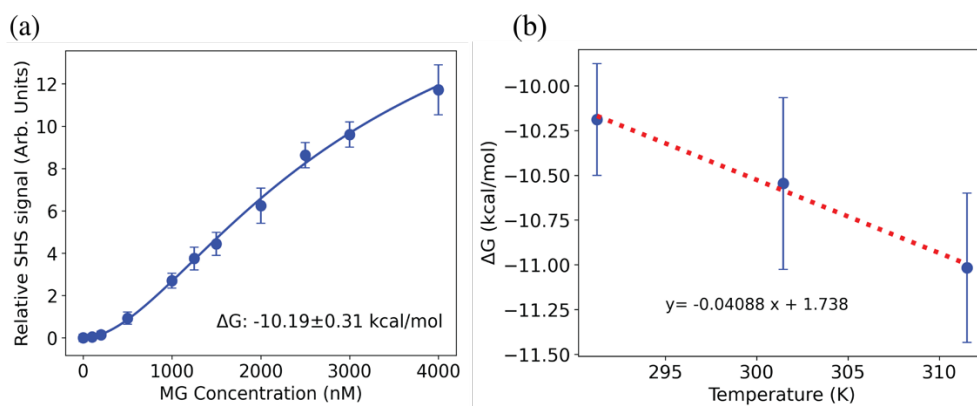


Figure 3.2. (a) Relative SHS signal as a function of the concentration of MG in solution with uncharged PSB at 291 K. Error bars show the standard deviation in normalized SHS intensity. The solid line represents the Langmuir isotherm fit. (b) ΔG_{ads} as a function of temperature. The error bars depict the uncertainty in the Langmuir fit for each temperature. The dotted red line is the line of best fit and provides ΔH_{ads} and ΔS_{ads} .

3.3.3 MG adsorbed to (+)PSB

To study all possible charge interactions on the surface, we repeated the temperature-dependent measurements on (+)PSB. Figure 3.3(a) shows that the ΔG_{ads} of cationic MG on the positively charged surface at 291 K was the least favorable of the systems examined herein (-9.38 ± 0.10 kcal/mol).

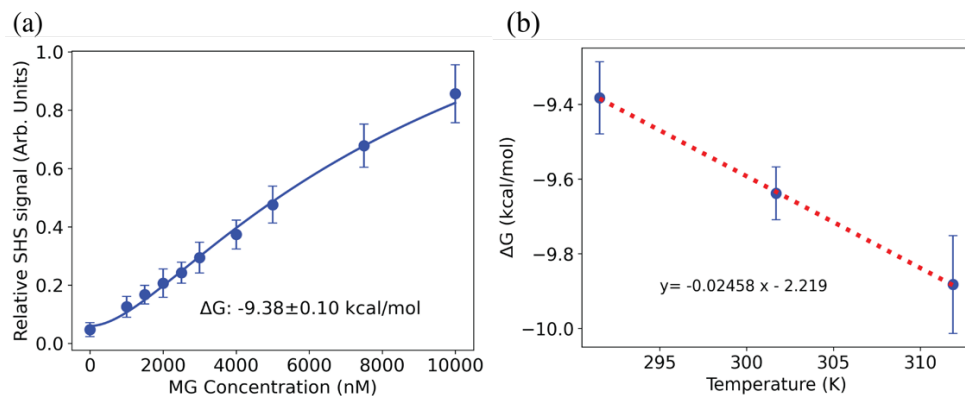


Figure 3.3. (a) Relative SHS signal as a function of the concentration of MG in solution with (+)PSB at 291 K. Error bars show the standard deviation in normalized SHS intensity. The solid line represents the Langmuir isotherm fit. (b) Determined ΔG_{ads} as a function of temperature. The error bars depict the uncertainty in the Langmuir fit for each temperature. The dotted red line is the line of best fit and provides ΔH_{ads} and ΔS_{ads} .

In contrast to the ΔH_{ads} values obtained for (-)PSB and plain PSB, the ΔH_{ads} for the (+)PSB surface is exothermic (-2.22 ± 0.41 kcal/mol). Although we report a high value of uncertainty, the sign of the ΔH_{ads} remains negative within error.

We summarize the thermodynamic values; ΔG_{ads} , ΔH_{ads} , and ΔS_{ads} for the adsorption of cationic MG to (-)PSB, plain PSB, and (+)PSB in Table 3.1. The sign of ΔS_{ads} does not change across the differently charged systems, indicating that they are all entropically-driven. We also report the thermodynamic parameters of the adsorption process for the *anionic* dye NYS to the (+)PSB surface (Figure S1).

Table 3.1. Experimentally determined thermodynamic values

System	Charges	ΔG_{ads} , at 291 K (kcal/mol)	ΔH_{ads} (kcal/mol)	ΔS_{ads} (kcal/mol K)
MG:(-)PSB	+/-	-10.83 ± 0.11	0.48 ± 0.37	0.0384 ± 0.0007
MG:PSB	+/0	-10.19 ± 0.31	1.74 ± 1.17	0.0409 ± 0.0053
MG:(+)PSB	+/+	-9.38 ± 0.10	-2.22 ± 0.41	0.0246 ± 0.0017
NYS:(+)PSB	-/+	-10.49 ± 0.04	-2.90 ± 1.37	0.0260 ± 0.0049

Table 3.1: Table of Gibbs free energy (ΔG_{ads}), entropy (ΔS_{ads}), and enthalpy (ΔH_{ads}) values describing the adsorption of chromophores to differently charged colloidal polystyrene surfaces.

3.3.4 Centrifuge Separation

Our fits to the modified Langmuir isotherm discussed above, did not allow for the determination of an uncorrelated N_m^D . Table 3.2 shows the values of N_m^D calculated via the centrifuge separation method outlined by Eckenrode et. al. for the adsorption of MG to each of our surfaces. We find that even though the favorability of the adsorption process is very similar among the surfaces studied, it does not correlate to the number of adsorption sites on each surface.

Table 3.2. Maximum surface number density of MG

System	Charges	N_m^D (nM)
MG:(-)PSB	+/-	537
MG:PSB	+/0	869
MG:(+)PSB	+/+	180

Table 3.2. N_m^D values determined from adsorption values of the supernatant following centrifuging 2 uM MG with (-)PSB and PSB and 5 uM MG with (+)PSB.

3.3.5 Discussion

We found that for all the systems studied herein, ΔG_{ads} became more negative, viz. more favorable, as the temperature was increased. This negative slope indicated that we had a positive ΔS_{ads} for adsorption to each surface (Table 3.1). We conclude that the adsorption of dye to all PSB interfaces is entropically driven. Previously, we have reported that the adsorption of the thiocyanate anion to a water-hydrophobe interface is similarly entropically driven, attributing the increase in entropy to the dragging of the anion through the oil/water barrier and the creation of “fingers” with the extension of the solvation shell of the ion.⁶ We doubt that picture extends to the solid-water interface that is probed in these experiments. Further, these ΔS_{ads} values are not comparable to that of the graphene-water interface or the air-water interface, which was found to be enthalpically controlled.¹⁴ Otten et al. experimentally determine a $\Delta S_{\text{ads,SCN}} = -17 \pm 3$ J/mol K for the adsorption of thiocyanate to the air-water interface utilizing temperature-resolved SHG. $\Delta S_{\text{ads,SCN}}$ is ~ 10 times smaller in magnitude, and opposite in sign from $\Delta S_{\text{ads,MG}}$, implying that the adsorption mechanism for the air-water interface clearly doesn’t describe the process occurring here at our solid-water interfaces. Instead, a new picture of the adsorption process at a plastic surface needs to be developed.

Typically, the adsorption of molecules and ions to a solid surface is considered entropically unfavorable, as the number of degrees of freedom decrease upon adsorption. However, this picture neglects changes in entropy occurring at the surface of the adsorbent or within the solvent.²¹ Favorable changes in entropy of the adsorbent can counteract the decrease in entropy due to adsorption of the dye molecules, specifically if the adsorption process may be classified as chemisorption, rather than physisorption. The large (positive) ΔS_{ads} values (Table 3.1) may be due to the displacement of previously ordered water by the adsorbing dye molecules. The displaced water molecules in turn gain a translational degree of freedom upon re-entry into the bulk solution.^{22,23} Further, water molecules around the aqueous bulk MG particles may be preferentially arranged, and these too may become more disordered upon adsorption of the dye.²⁴ This observation requires that a theoretical description defines water-solute, water-polystyrene, and solute-polystyrene interactions to correctly estimate the ΔS_{ads} . These experimental findings will inform such future theoretical work by limiting similar systems to entropically-driven mechanisms.

Adsorption processes can be further characterized as resulting from physisorption or chemisorption with reference to the magnitude of ΔG_{ads} and ΔH_{ads} . Humpola et al. assign ΔG_{ads} values ranging from -80 to -400 kJ/mol (~ -19 to -95 kcal/mol) to chemical adsorption processes, while the range of 0 to -20 kJ/mol (~ 0 to -7.2 kcal/mol) represents physical adsorption.²⁵ Kara et al. attribute ΔH_{ads} smaller than 40 kJ/mol (~ 9.6 kcal/mol) to physisorption.²⁶ Therefore, all of our determined values of ΔH_{ads} (Table 3.1) represent physical adsorption and imply that interactions

such as hydrogen bonding, van der Waals forces, and dipole-dipole interactions dominate our adsorption picture. Considering the adsorption of MG to (-)PSB, it is easy to assume that attractive Coulombic interactions drive the adsorption process. However, we observe very small changes in magnitude of ΔH_{ads} (Table 3.1) as we alter the charge at the surface. This small change does not align with the assumption that electrostatic interactions dominate these processes. Therefore, the charged surfaces studied herein must also bind adsorbate via weaker intermolecular forces. Eckenrode et al. come to a similar conclusion; they highlight that the similarities between the ΔG values don't reflect the large difference in energy expected for charge-charge vs. hydrophobic interactions.¹² Therefore, they suggest that other interactions are counteracting the lower free energies associated with van der Waals interactions between MG and the neutral or positive surface. At the pH used in our studies, the surface of (-)PSB and (+)PSB samples are only 5-10% surface charged, implying there may be gaps of bare PSB between functional groups.²⁷ The plain, uncharged PSB surface is a strong adsorber of MG (-10.19 kcal/mol). Further, the N_m^D values calculated by centrifuge separation (Table 3.2) show that there is a large difference in the number of available adsorption sites across each surface. From these data, we assume that van der Waals forces are occurring between portions of bare PSB surface and MG. Such intermolecular forces must exist between MG and all the surfaces studied herein. These findings can guide theoretical models to consider mechanisms that include both coulombic and intermolecular binding upon adsorption.

Unlike many of the thermodynamic parameters observed by the Saykally group for ion adsorption to an interface, the adsorption of chromophores is often endothermic despite the surface they are adsorbed to.²⁸⁻³² In our studies, we find that a small positive ΔH_{ads} describes the adsorption of MG to (-)PSB and PSB, whereas adsorption of MG to (+)PSB is exothermic. We find that the sign of ΔH_{ads} is affected more by the charge of the surface than by the charge of the adsorbate. This is shown in Table 1 by comparison of the adsorption of MG and NYS to (+)PSB. The adsorption of both the anionic NYS and cationic MG dye is exothermic, with similar ΔH_{ads} of -2.22 to -2.90 kcal/mol. This flip in the sign of ΔH_{ads} upon changing the surface charge highlights the balance between surface, solvent, and adsorbate interactions that comprise these complicated mechanisms. Wang et al. highlight the vital importance of understanding solvent-surface interactions for peptide adsorption to differently-treated solid surfaces. They find that a hydrophilic gold (Au) surface exhibits stronger water interactions than a hydrophobic graphite surface. The peptide has a similar propensity (shown by ΔG) for the Au and graphite surfaces. However, they find that the distribution of enthalpic and entropic contributions depend on these different water interactions.³³ Similarly, we find that the charge of the PSB surface influences the adsorption process through preferential ordering of water at the interface. For both (-)PSB and neutral PSB, water orients with the positive hydrogen facing the surface,³⁴ while water aligns its negative oxygen towards (+)PSB.³⁵ Obviously, these differences engender energetic differences for MG adsorption, reflected in the sign of ΔH_{ads} . Once again, these findings may inform a theoretical picture that weights the surface charge above the charge of the adsorbing species. Wang et al. model peptide adsorption by first developing a strong understanding of water at both hydrophobic and hydrophilic interfaces. They report that water has two regions of higher density near the surface.³³ This picture aligns with the leading modern understanding of the instantaneous interface.^{36,37} Our experimental findings may also extend to ion adsorption at electrochemical interfaces, in which stratification of interfacial water is likely.³⁶

While temperature-dependent SHS results do not themselves provide an unambiguous description for the general mechanism of dye adsorption to aqueous-solid interfaces, these

experimental results provide substantial guidance for the development of a theoretical model. As discussed in Chapter 2, SHGS is a surface-specific probe, and therefore provides quantitative thermodynamic information specific to the interface rather than to the bulk. These SHS results could be accompanied by Sum Frequency Generation Scattering measurements, which are also surface specific, to probe the change in interfacial water orientation upon adsorption at the differently charged interfaces^{34,35}, which we conclude to be vital for untangling enthalpic and entropic contributions to overall adsorption mechanism. Additionally, other SHS techniques discussed within this thesis, viz. angle-resolved and polarization-resolved methods, could provide information such as adsorbate orientation at the surface, but making these measurements concurrently would require robust changes to the experimental design presented here and would result in an increase in error. In any case, the determination of quantitative experimentally-obtained values which describe adsorption at the interface are invaluable for developing models of adsorption of pollutants to plastic interfaces (MG and PSB), as well as to other ubiquitous solid-liquid interfaces, viz. biological and soft-matter surfaces.

Supplemental Information

S1. Langmuir fits and linear NYS:(+)PSB

Here we repeat our experiments on the adsorption of naphthol yellow (NYS) to (+)PSB first reported by Cole et al, and again extend them by determining the enthalpy and entropy of adsorption. While the ΔG obtained in this experiment ($\Delta G = -10.49 \pm 0.04$) is slightly more negative than that which was previously reported ($\Delta G = -10.27 \pm 0.09$)¹, this small difference may be attributed to the lack of temperature control in the previous experiments.

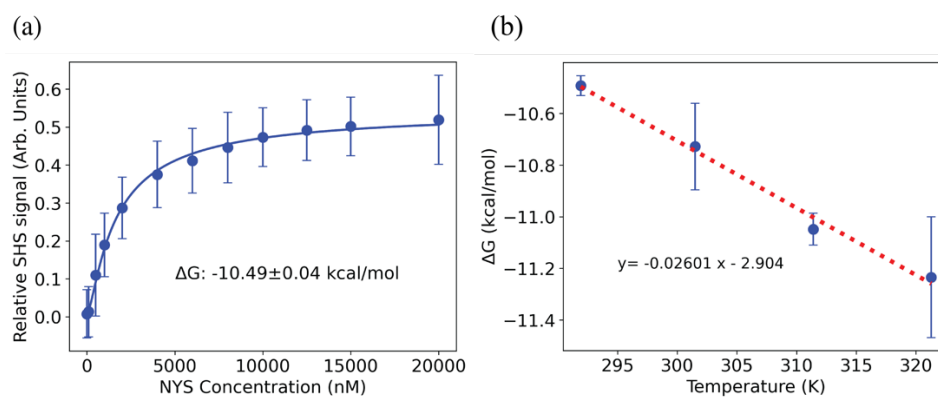


Figure S1. (a) Relative SHS signal as a function of the concentration of NYS in solution with (+)PSB at 291 K. Error bars show the standard deviation in normalized SHS intensity. The solid line represents the Langmuir isotherm fit. (b) ΔG_{ads} as a function of temperature. The error bars depict the uncertainty in the Langmuir fit for each temperature. The dotted red line is the line of best fit and provides ΔH_{ads} and ΔS_{ads} .

References

- (1) Cole, W. T. S.; Wei, H.; Nguyen, S. C.; Harris, C. B.; Miller, D. J.; Saykally, R. J. Dynamics of Micropollutant Adsorption to Polystyrene Surfaces Probed by Angle-Resolved Second Harmonic Scattering. *Journal of Physical Chemistry C* **2019**, *123* (23), 14362–14369. <https://doi.org/10.1021/acs.jpcc.9b01146>.

- (2) Gonella, G.; Dai, H. L. Second Harmonic Light Scattering from the Surface of Colloidal Objects: Theory and Applications. *Langmuir* **2014**, *30* (10), 2588–2599. <https://doi.org/10.1021/la403570f>.
- (3) Nguyen, D.; Casillas, S.; Vang, H.; Garcia, A.; Mizuno, H.; Riffe, E. J.; Saykally, R. J.; Nguyen, S. C. Catalytic Mechanism of Interfacial Water in the Cycloaddition of Quadricyclane and Diethyl Azodicarboxylate. *Journal of Physical Chemistry Letters* **2021**, *12* (12), 3026–3030. <https://doi.org/10.1021/acs.jpcclett.1c00565>.
- (4) Fairbrother, D. H.; Geiger, F. M. Environmental Processes at the Solid–Liquid Interface: What Constitutes New Physical Insights? *J. Phys. Chem. C* **2017**, *121* (32), 17045–17045. <https://doi.org/10.1021/acs.jpcc.7b07172>.
- (5) Al Harraq, A.; Bharti, B. Microplastics through the Lens of Colloid Science. *ACS Environ. Au* **2022**, *2* (1), 3–10. <https://doi.org/10.1021/acsenvironau.1c00016>.
- (6) Devlin, S. W.; Benjamin, I.; Saykally, R. J. On the Mechanisms of Ion Adsorption to Aqueous Interfaces: Air–Water vs. Oil–Water. *Proceedings of the National Academy of Sciences* **2022**, *119* (42), e2210857119. <https://doi.org/10.1073/pnas.2210857119>.
- (7) Devlin, S. W.; McCaffrey, D. L.; Saykally, R. J. Characterizing Anion Adsorption to Aqueous Interfaces: Toluene–Water versus Air–Water. *J. Phys. Chem. Lett.* **2021**, 222–228. <https://doi.org/10.1021/acs.jpcclett.1c03816>.
- (8) McCaffrey, D. L.; Nguyen, S. C.; Cox, S. J.; Weller, H.; Alivisatos, A. P.; Geissler, P. L.; Saykally, R. J. Mechanism of Ion Adsorption to Aqueous Interfaces: Graphene/Water vs. Air/Water. *Proceedings of the National Academy of Sciences of the United States of America* **2017**, *114* (51), 13369–13373. <https://doi.org/10.1073/pnas.1702760114>.
- (9) Onorato, R. M.; Otten, D. E.; Saykally, R. J. Measurement of Bromide Ion Affinities for the Air/Water and Dodecanol/Water Interfaces at Molar Concentrations by UV Second Harmonic Generation Spectroscopy. *J. Phys. Chem. C* **2010**, *114* (32), 13746–13751. <https://doi.org/10.1021/jp103454r>.
- (10) Mizuno, H.; Rizzuto, A. M.; Saykally, R. J. Charge-Transfer-to-Solvent Spectrum of Thiocyanate at the Air/Water Interface Measured by Broadband Deep Ultraviolet Electronic Sum Frequency Generation Spectroscopy. *Journal of Physical Chemistry Letters* **2018**, *9* (16), 4753–4757. <https://doi.org/10.1021/acs.jpcclett.8b01966>.
- (11) Eisenthal, K. B. Second Harmonic Spectroscopy of Aqueous Nano- and Microparticle Interfaces. *Chemical Reviews* **2006**, *106* (4), 1462–1477. <https://doi.org/10.1021/cr0403685>.
- (12) Eckenrode, H. M.; Jen, S. H.; Han, J.; Yeh, A. G.; Dai, H. L. Adsorption of a Cationic Dye Molecule on Polystyrene Microspheres in Colloids: Effect of Surface Charge and Composition Probed by Second Harmonic Generation. *Journal of Physical Chemistry B* **2005**, *109* (10), 4646–4653. <https://doi.org/10.1021/jp045610q>.
- (13) Eckenrode, H. M.; Dai, H.-L. Nonlinear Optical Probe of Biopolymer Adsorption on Colloidal Particle Surface: Poly-L-Lysine on Polystyrene Sulfate Microspheres. *Langmuir* **2004**, *20* (21), 9202–9209. <https://doi.org/10.1021/la048863j>.
- (14) Otten, D. E.; Shaffer, P. R.; Geissler, P. L.; Saykally, R. J. Elucidating the Mechanism of Selective Ion Adsorption to the Liquid Water Surface. *Proceedings of the National Academy of Sciences of the United States of America* **2012**, *109* (3), 701–705. <https://doi.org/10.1073/pnas.1116169109>.

- (15) Chase, H. M.; Ho, J.; Upshur, M. A.; Thomson, R. J.; Batista, V. S.; Geiger, F. M. Unanticipated Stickiness of α -Pinene. *J. Phys. Chem. A* **2017**, *121* (17), 3239–3246. <https://doi.org/10.1021/acs.jpca.6b12653>.
- (16) Hamal, P.; Subasinghe Don, V.; Nguyenhuu, H.; Ranasinghe, J. C.; Nauman, J. A.; McCarley, R. L.; Kumar, R.; Haber, L. H. Influence of Temperature on Molecular Adsorption and Transport at Liposome Surfaces Studied by Molecular Dynamics Simulations and Second Harmonic Generation Spectroscopy. *J. Phys. Chem. B* **2021**, *125* (37), 10506–10513. <https://doi.org/10.1021/acs.jpcc.1c04263>.
- (17) Wang, H.; Troxler, T.; Yeh, A. G.; Dai, H. L. In Situ, Nonlinear Optical Probe of Surfactant Adsorption on the Surface of Microparticles in Colloids. *Langmuir* **2000**, *16* (6), 2475–2481. <https://doi.org/10.1021/la9909087>.
- (18) Schürer, B.; Peukert, W. In Situ Surface Characterization of Polydisperse Colloidal Particles by Second Harmonic Generation. *Particulate Science and Technology* **2010**, *28* (5), 458–471. <https://doi.org/10.1080/02726351.2010.504131>.
- (19) Gonella, G.; Dai, H.-L. Determination of Adsorption Geometry on Spherical Particles from Nonlinear Mie Theory Analysis of Surface Second Harmonic Generation. *Phys. Rev. B* **2011**, *84* (12), 121402. <https://doi.org/10.1103/PhysRevB.84.121402>.
- (20) Wang, H.; Yan, E. C. Y.; Liu, Y.; Eisenthal, K. B. *Energetics and Population of Molecules at Microscopic Liquid and Solid Surfaces*; 1998. <https://pubs.acs.org/sharingguidelines>.
- (21) Thomas, J. M. The Existence of Endothermic Adsorption. *J. Chem. Educ.* **1961**, *38* (3), 138. <https://doi.org/10.1021/ed038p138>.
- (22) Teli, M. D.; Nadathur, G. T. Adsorptive Removal of Acid Yellow 17 (an Anionic Dye) from Water by Novel Ionene Chloride Modified Electrospun Silica Nanofibres. *Journal of Environmental Chemical Engineering* **2018**, *6* (6), 7257–7272. <https://doi.org/10.1016/j.jece.2018.10.005>.
- (23) Balankura, T.; Qi, X.; Fichthorn, K. A. Solvent Effects on Molecular Adsorption on Ag Surfaces: Polyvinylpyrrolidone Oligomers. *J. Phys. Chem. C* **2018**, *122* (26), 14566–14573. <https://doi.org/10.1021/acs.jpcc.8b03156>.
- (24) Somusundurun, P.; Huong, L. Thermodynamics of Adsorption of Surfactants at a Solid-Liquid Interface.
- (25) Húmpola, P. D.; Odetti, H. S.; Fertitta, A. E.; Vicente, J. L. Thermodynamic Analysis of Adsorption Models of Phenol in Liquid Phase on Different Activated Carbons. *J. Chil. Chem. Soc.* **2013**, *58* (1), 1541–1544. <https://doi.org/10.4067/S0717-97072013000100009>.
- (26) Kara, M.; Yuzer, H.; Sabah, E.; Celik, M. S. Adsorption of Cobalt from Aqueous Solutions onto Sepiolite. *Water Research* **2003**, *37* (1), 224–232. [https://doi.org/10.1016/S0043-1354\(02\)00265-8](https://doi.org/10.1016/S0043-1354(02)00265-8).
- (27) Williams, T.; Walsh, C.; Murray, K.; Subir, M. Interactions of Emerging Contaminants with Model Colloidal Microplastics, C₆₀ Fullerene, and Natural Organic Matter – Effect of Surface Functional Group and Adsorbate Properties. *Environ. Sci.: Processes Impacts* **2020**, *22* (5), 1190–1200. <https://doi.org/10.1039/D0EM00026D>.
- (28) Bello, O. S.; Ahmad, M. A.; Semire, B. Scavenging Malachite Green Dye from Aqueous Solutions Using Pomelo (*Citrus Grandis*) Peels: Kinetic, Equilibrium and Thermodynamic Studies. *Desalination and Water Treatment* **2015**, *56* (2), 521–535. <https://doi.org/10.1080/19443994.2014.940387>.

- (29) Bakry, A.; Darwish, M. S. A.; Hassanein, T. F. Adsorption of Methylene Blue from Aqueous Solutions Using Carboxyl/Nitro-Functionalized Microparticles Derived from Polypropylene Waste. *Iran Polym J* **2022**, *31* (2), 185–197. <https://doi.org/10.1007/s13726-021-00979-w>.
- (30) Lee, J. H.; Sim, S. J.; Kang, J. H.; Choi, S. S. Isotherm and Thermodynamic Modelling of Malachite Green on CO₂-Activated Carbon Fibers. *Chemical Physics Letters* **2021**, *780*, 138962. <https://doi.org/10.1016/j.cplett.2021.138962>.
- (31) Aljeboree, A. M.; Alkaim, A. F. Studying Removal of Anionic Dye by Prepared Highly Adsorbent Surface Hydrogel Nanocomposite as an Applicable for Aqueous Solution. *Sci Rep* **2024**, *14* (1), 9102. <https://doi.org/10.1038/s41598-024-59545-y>.
- (32) Nair, A.; Kumawat, Y. K.; Choudhary, S.; Nath, J.; Sharma, K.; Rasool, T.; Sharma, V.; Kumar, V. Malachite Green Dye Adsorption from Wastewater Using Pine Gum-Based Hydrogel: Kinetic and Thermodynamic Studies. *Journal of Molecular Structure* **2024**, *1295*, 136671. <https://doi.org/10.1016/j.molstruc.2023.136671>.
- (33) Wang, X.; Yang, X.; Chen, H.; Yang, X.; Xu, Z. Entropy–Enthalpy Compensation in Peptide Adsorption on Solid Surfaces: Dependence on Surface Hydration. *Langmuir* **2020**, *36* (36), 10822–10829. <https://doi.org/10.1021/acs.langmuir.0c01845>.
- (34) Strazdaite, S.; Versluis, J.; Bakker, H. J. Water Orientation at Hydrophobic Interfaces. *The Journal of Chemical Physics* **2015**, *143* (8), 084708. <https://doi.org/10.1063/1.4929905>.
- (35) Gonella, G.; Backus, E. H. G.; Nagata, Y.; Bonthuis, D. J.; Loche, P.; Schlaich, A.; Netz, R. R.; Kühnle, A.; McCrum, I. T.; Koper, M. T. M.; et al. Water at Charged Interfaces. *Nat Rev Chem* **2021**, *5* (7), 466–485. <https://doi.org/10.1038/s41570-021-00293-2>.
- (36) Litman, Y.; Chiang, K.-Y.; Seki, T.; Nagata, Y.; Bonn, M. Surface Stratification Determines the Interfacial Water Structure of Simple Electrolyte Solutions. *Nat. Chem.* **2024**, *16* (4), 644–650. <https://doi.org/10.1038/s41557-023-01416-6>.

Chapter 4. Examining Porous Surfaces with Second Harmonic Scattering

4.1 Introduction

Thus far, this dissertation has focused on understanding adsorption of molecules to solid colloidal interfaces; however, with the advent of more advanced material science design, *porous* colloidal particles are realized as another class of materials which act as excellent adsorbers. One such example is metal-organic frameworks (MOFs) nanoparticles, which are highly functionally tunable.¹ Many MOFs are being employed to capture gas, water, or pollutants because of their high porosity.²⁻⁹ Within this chapter, we examine one such colloidal MOF, a zeolitic imidazolate framework (ZIF-8) and its interactions with a prototypical dye, malachite green (MG). ZIF-8 has been realized by collaborators as part of a colorimetric sensor for the detection of CO₂ indoors at levels harmful to human health. Davey et al. present evidence that ZIF-8 acts in conjunction with ethylenediamine and phenolsulfonphthalein dyes to cause a color change when CO₂ is adsorbed by the framework.¹⁰ Here we simplify the system to ZIF-8 and MG dye to inform the location and adsorption thermodynamics of the dye. Understanding the interactions between the MOF and dye can provide valuable information for the design of future MOF-based sensors.

MOFs have dominated the literature at the cross-section of organic and inorganic synthesis in recent decades, with over 90,000 different MOFs having been reported to date.¹¹ MOFs are constructed by joining metal-containing molecules (nodes) with organic linkers, the numerous possible combinations allowing for the synthesis of materials with a vast array of functionality.^{1,11} In 1999, detailed characterization of MOF-5 provided proof that MOFs exhibit permanent porosity and increased surface area relative to other common porous materials, such as zeolites and activated carbon.¹² Almost a decade later, monodisperse nanocrystal MOFs were realized.¹³ The morphology of these nanocrystals is controlled by synthetic conditions, such as reaction temperature. This ease of control and multitude of choice allows researchers to optimize their sorption abilities, and therefore MOFs excel in chemical separations and gas capture. ZIF-8 belongs to a subsector of MOFs that are isostructural to zeolites. More than 150 ZIFs have been reported, and in 2009 ZIF-8 was the first reported nanocrystalline MOF.¹⁴ Colloidal MOFs, viz., ZIF-8, are particularly suited for drug delivery and pollutant removal.

To selectively probe MG at the surface of ZIF-8, we employ SHS; we rely on the n to π^* transition of MG to enhance our signal via two-photon resonant enhancement. By utilizing SHS in an angle-resolved scheme, we can determine the size and shape of the ZIF-8 particles.¹⁵ Calibration curves of MG concentration as a function of SHS signal show a discontinuity at certain concentrations. To better understand these observations, polarization-dependent SHS methods were employed. These polarization-dependent measurements give insight into the orientation of MG relative to the ZIF-8 surface.¹⁶ The complexity of the ZIF-8 surface was studied previously by SHS, where the authors utilized the nonlinear technique to track the morphology of ZIF-8 crystals in situ.¹⁷ However, the competing incoherent processes introduced by MG, which is needed to probe the surface at the wavelengths used in our SHS setup, complicate the analysis of this system.¹⁸ We therefore try to simplify the system by examining MG in solution with mesoporous silica nanoparticles (pSNP) of a similar size as ZIF-8.

Porous silica itself is an interesting interface, with uses in various environmentally relevant applications viz. wastewater remediation, air-cleaning, catalysis, and CO₂ capture.^{19–26} Herein, we compare the adsorption of MG to pSNP and nonporous silica. We utilize the data of MG with pSNP to inform our analysis of the ZIF-8 solutions.

4.2 Materials and Methods

4.2.1 Experimental Design

The details of the SHGS setup are outlined in Chapter 2 and Chapter 3. For the following experiments on colloidal porous surfaces, the second harmonic was measured by a rotating collection arm. Data were collected in steps of 2.5°, over a total of 180° centered about transmission. At each data point, 20 scans were measured and averaged with a counting time of 500 ms. Therefore, each concentration required 12 minutes of acquisition time. The resulting angle-resolved (AR) scattering patterns provide insight on the diameter of the particles being probed. Polarization-resolved measurements were made by detecting the scattered signal at a set angle (20°) and changing the polarization angle of the fundamental light with a half-wave plate before focusing into the sample vial. The output polarization is selected by a polarizer as either parallel (Pout) or perpendicular (Sout) to the plane of incidence. These measurements provide insight to the average orientation of the adsorbed dye on the colloidal porous surface.¹⁶

4.2.2 Sample Preparation

Porous samples of silica nanoparticles (SNP) and a metal-organic framework (MOF); ZIF-8 are prepared in a bulk solution with either water or methanol as a solvent, respectively. The porous SNP (pSNP) was purchased from Thermo Fisher Scientific and used as received. The pSNP particles have a diameter of 200 nm with 2-4 nm size pores. The ZIF-8 particles were synthesized at room-temperature following a common procedure in literature.¹⁰ Briefly, a 1:1 mass ratio of zinc nitrate hexahydrate and 2-methylimidazole dissolved in methanol is mixed and left to react overnight. The resulting crystals are washed three times with methanol and centrifuged. SEM characterization of the ZIF-8 particles indicates their diameter to be about 100 nm.¹⁰ ZIF-8 exhibits a pore aperture of 3.4 Å and a pore cavity diameter of 11.6 Å.²⁷ Suspensions were made from stock solutions of ZIF-8 or pSNP with malachite green (MG) dye. Concentration curves of MG in solution with the surface of the particles were made by taking AR-SHS measurements of aliquots of the suspensions immediately after sample preparation. ZIF-8:MG samples studied 24 hours after preparation were stored in light-safe containers to avoid possible photodegradation of MG.

4.3 Results and Discussion

4.3.1 Porous Silica Nanoparticles

To understand angle-resolved SHS of ZIF-8 or pSNP, we first observe how the diameter of the nanoparticles impacts the shape of the scattering pattern. In Figure 4.1, the scattering patterns from solutions of 800 nm microspheres and 100 nm nanospheres are compared. Larger particles scatter SH light closer to the transmission angle (0 °), while smaller particles scatter light more broadly over a range of larger angles. The angles corresponding to maxima of SH intensity are optimal for obtaining orientational information about adsorbate molecules via polarization-resolved measurements, discussed later. This optimal angular range can be calculated by

$$qR = 2k_0R \sin(\theta/2) \quad (4.1)$$

where q is the scattering vector, R is the radius of the particle, k_0 the wave vector of the scattered light and θ the angle the light is scattered.

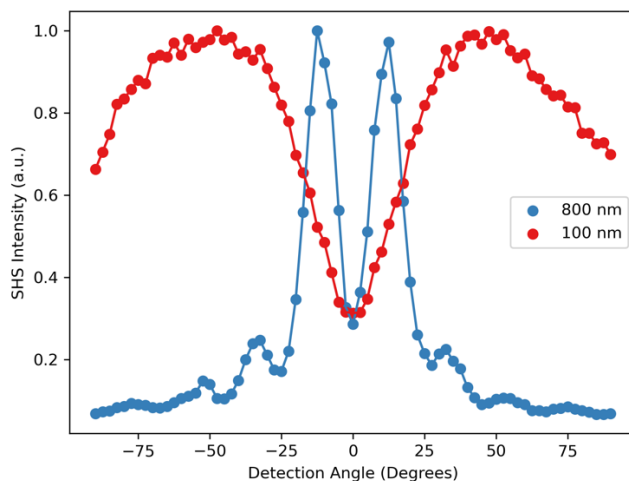


Figure 4.1. Angle-resolved scattering pattern for nanospheres with diameters of 100 nm (red) and 800 nm (blue). 800 nm particles have maximum SH intensity at $\pm 12.5^\circ$ and 100 nm particles have maximum SH intensity at $\pm 47.5^\circ$. Smaller colloids shift the maximum scattering intensity towards larger angles.

From these results and Equation 4.1, we assume that the pSNP particles, which have a diameter of 200 nm, should have maxima between 23 and 51° . Figure 2 (a) shows the scattering pattern for pSNP with 20 μM MG at the two polarization configurations SinSout and SinPout. The maximum intensity is instead closer to 0° , as it would be for particles larger than 800 nm, but for larger particles we would expect to see diminished SH intensity at 0° . The pSNP scattering pattern lacks both the local minima at 0° and the broad range of scattered light at larger angles. This implies that for porous nanospheres, the scattering pattern may not depend solely on the size of the nanosphere, but perhaps also on the total adsorption area available. Figure 4.2 (b) depicts the typical scattering results at the identified polarization configurations, at which there is very little scattering in the forward direction and negligible s-polarized output. This pattern is well-described by nonlinear Rayleigh-Gans-Debye (NLRGD) and nonlinear Mie (NLM) theories.^{15,28} Obviously, Figure 4.2 (a) is not similarly described. One explanation is that the p-polarized output is similarly negligible, and that we don't observe SH enhancement at the surface of pSNP. We continue our discussion of pSNP by comparing SH response from 60 μM MG in solution with pSNP and nonporous SNP, both with a diameter of 200 nm (Figure 4.3)

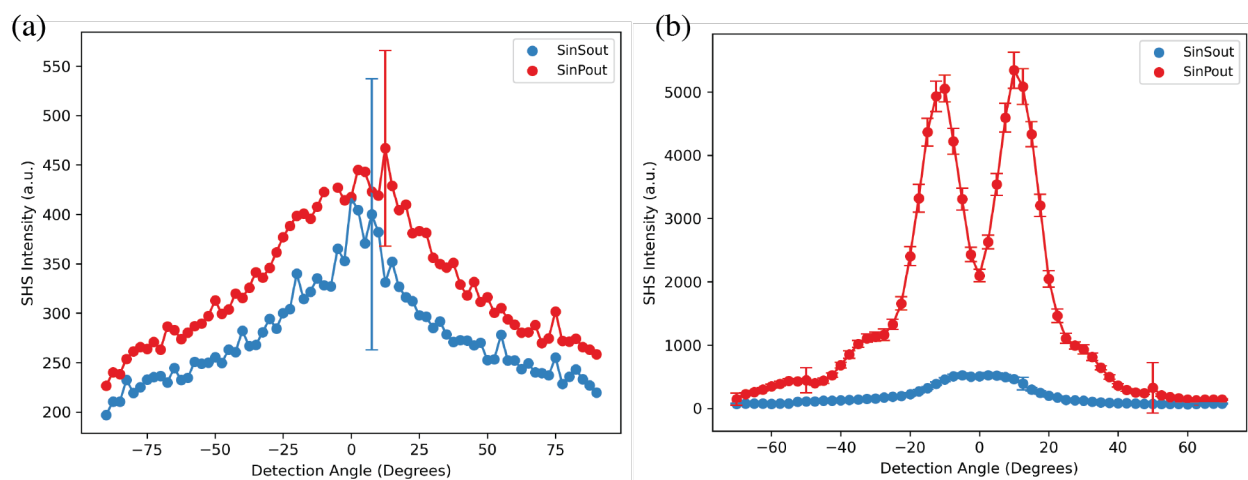


Figure 4.2. (a) AR s- and p- polarized scattering patterns of a solution of 20 uM MG and 200 nm pSNP. (b) AR s- and p- polarized scattering patterns of a solution of 30 uM MG and 800 nm nonporous nanospheres.

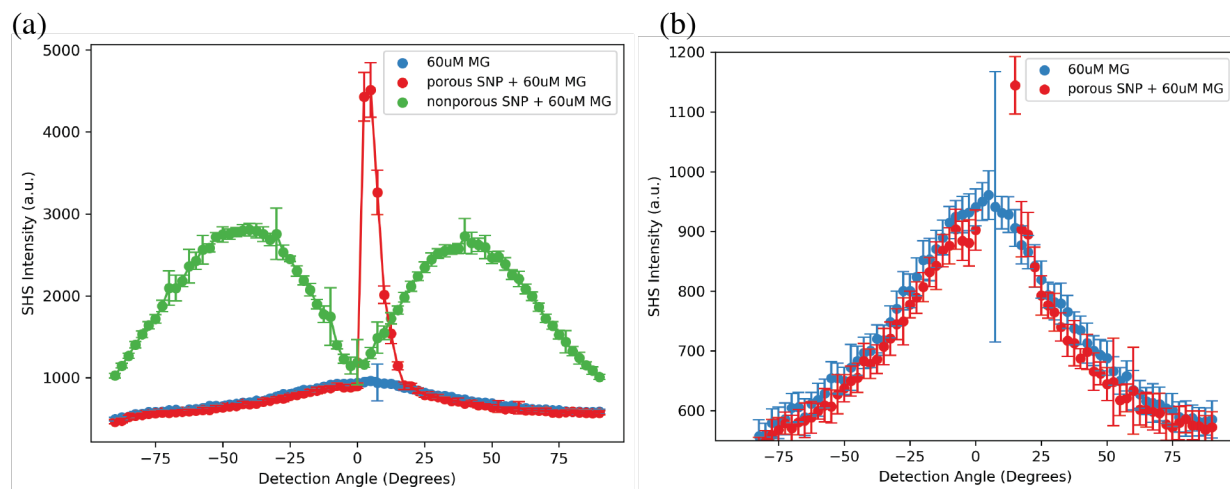


Figure 4.3. (a) Angle-resolved scattering pattern of 60 uM MG with and without porous or nonporous SNP, showing that a typical symmetric scattering pattern is only observed for nonporous SNP. (b) Zoomed-in depiction of 60 uM MG and porous SNP with 60 uM MG showing the similarity in counts for each solution.

Figure 4.3 (a) shows the scattering patterns for aqueous solutions of 60 uM MG (blue), 60 uM MG with porous SNP (red) and 60 uM MG with nonporous MG (green). The signal from aqueous MG is centered at transmission and represents hyper-Rayleigh scattering (HRS) from the molecules in the bulk. The green scattering pattern, representing 60 uM MG adsorbed to SNP, has peak SH intensity at about 40 degrees on either side of the angle of transmission. This symmetrical scattering pattern is typical of SHS from colloidal surfaces, as shown in Figure 4.1. The angle at which the SHS intensity reaches a maximum is dependent on the diameter of the particles being probed. Surprisingly, we see that for pSNP with 60 uM (red), the scattered signal rapidly increases near transmission, despite the diameter of the pSNP being the same as the nonporous SNP (green). Dadap et al. attribute similar “hot spots” or fluctuations in their SFS data to scattering from clusters of particles in solution. They highlight that SFS can discern between coherent and incoherent

sources of the fluctuations, whereas SHS is limited because the incoherent processes HRS and two-photon fluorescence (TPF) from MG may compete.¹⁸

Additionally, the scattered signal at larger angles is within error of the signal from aqueous MG, implying that the signal may represent MG in the bulk and not adsorbed to the surface (Figure 4.2 (b)). Across all the concentrations studied, aqueous MG had higher SH photon counts than MG with porous SNP. This is an odd observation, as MG on nonporous SNP exhibits great signal enhancement relative to an aqueous solution of MG at the same concentration. This could be a result of competing processes occurring for MG in solution with pSNP, which may cause the forward scattering and deconstructive interference. Moreover, higher concentrations of MG with porous SNP exhibit fewer fluctuations or “hot spots” than 60 μM MG with porous SNP. The concentration of 60 μM represents the concentration at which we assume maximum fractional coverage of nonporous SNP. If the fluctuations were due to the experimental setup, we would expect larger error bars than those shown in Figure 4.3 (a). This may be attributed again to competing incoherent processes of the HRS from MG and the signal from MG on SNP. The shift of scattering pattern towards 0 degrees, could indicate that the increase in adsorption sites introduced by the porous surface acts as a pseudo-larger diameter particle. However, we don't observe a dip in the SH intensity in the forward direction.

Overall, we find that even for our simplified pSNP system, the scattering results are difficult to analyze. We move on to a presentation of the SHS measurements of the microporous ZIF-8, which present similarly puzzling results.

4.3.2 ZIF-8

To study MG in solution with ZIF-8, we first optimized the detection angle for the highest intensity, finding that working at a detection angle of 20 ° provided the best signal-to-noise. We measured the SHS intensity as a function of increasing MG concentration. The first data set was taken with 0.5 mg/mL of ZIF-8, corresponding to 0.05% w/w, which is on the same order of magnitude of concentration that we utilize for all nanoparticles studies in this thesis (0.01% w/w). Knowing that porous surfaces can adsorb higher amounts of dye, we also utilized higher concentrations of MG. Figure 4.4 (a) shows our calibration curve for MG in solution with ZIF-8 at both Sin Pout and Sin Sout configurations. Surprisingly, the signal is greater for the s-polarized output, shown by red markers. Additionally, the calibration “curve” does not have the familiar sigmoidal shape. The SH intensity as a function of concentration remains nearly flat until a concentration of 900 μM , wherein the signal rapidly increases. At concentrations greater than 900 μM MG, the signal slowly decays. This discontinuity disrupted the plan to fit the calibration curve to a Langmuir isotherm in hopes of determining a Gibb's free adsorption value for the process. Instead, we hypothesized that the great increase in SH response could be evidence of the pores of ZIF-8 being filled. We repeated these experiments with less ZIF-8 (0.1 mg/mL, 0.01%) over concerns that the ZIF-8 itself was contributing too greatly to the SH signal. Figure 4.4 (b) shows the results. Again, we observe a relatively flat relationship between increasing MG concentration and SH intensity until 200 μM , wherein the signal rapidly increased, and subsequently decreased at higher MG concentrations. From these results, we conclude that the concentration at which the signal increases (900 and 200 μM) must be relevant to the process of the adsorption.

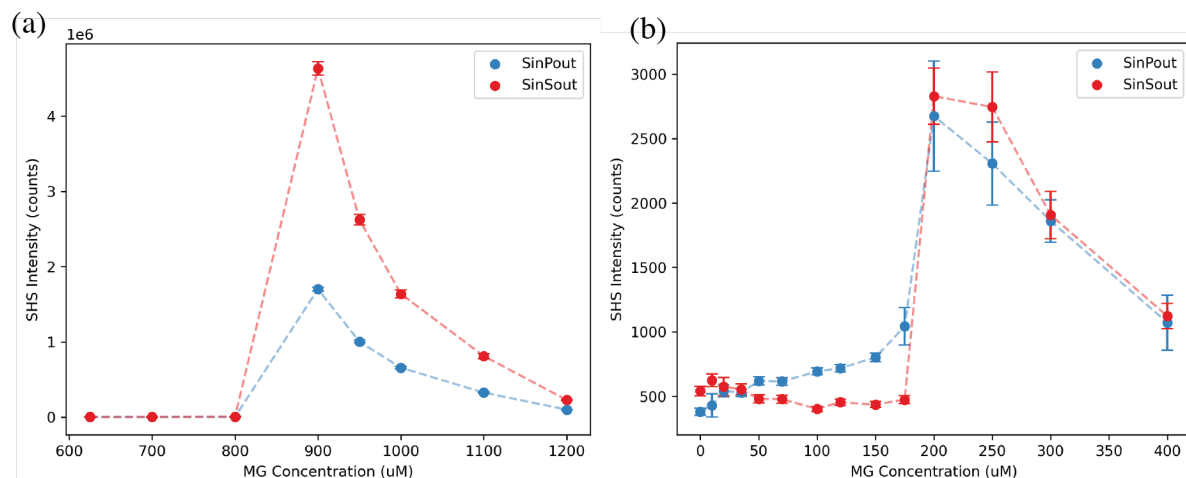


Figure 4.4. (a) SH intensity as a function of MG concentration for 0.5 mg/mL ZIF-8. The red data points represent the Sin Sout polarization configuration, and the blue points represent the Sin Pout polarization configuration. (b) Same as (a) but for lower concentration ZIF-8 (0.1 mg/mL).

The unusual, non-sigmoidal shape shown in Figure 4.4, indicates that the adsorption process cannot be described by the modified Langmuir isotherm used in previous chapters. The Langmuir isotherm assumes monolayer adsorption wherein the adsorbates do not interact. Kramer Campen et al. present other common isotherm shapes; our curves mostly match the “Type B” class, the shape of which they attribute to multi-layer adsorption, multi-site adsorption, or adsorbate dependent conformational changes.²⁹ However, our observed decrease in signal at higher concentrations is not typical of this class of isotherms. We assume that our isotherms represent an adsorption process that could include multi-layer adsorption, during which the pores of ZIF-8 may be filled first, and then dye is adsorbed in subsequent layers. It is also possible that multi-site adsorption is the cause of the atypical isotherm shape, as the chemistry at the pores may be energetically different than at other parts of the surface. However, it is important to note that the sizes of the pore apertures are less than half the size of the diameter of a MG molecule, 3.4 Å and 8.2 Å, respectively. It is possible that MG interacts with the pores despite this size difference. Previous SHG studies have shown 4-(4-diethylaminostyryl)- 1-methylpyridinium iodide (DAMPI) slowly aligns itself, with its pyridine ring into the pore like a “nail” into the pores of a zeolite material.³⁰ Similarly, MG could align one of its phenyl substituents into the pore aperture of ZIF-8. The alignment in the pore could also explain the change in dominate polarization configuration as a function of concentration. The adsorption mechanism of MG to a similar MOF, ZIF-67 has also been illustrated as $\pi - \pi$ stacking between the aromatic groups of MG and the imidazole linkers making up ZIF-67.³¹ Therefore, MG could be interacting with ZIF-8 in a similar way, lying parallel to the pore apertures. We conclude that the odd shape of the calibration curves may be caused by a complicated adsorption mechanism that is not easily explained under the assumptions we employ with the Langmuir model.

While SHS measurements are typically performed at equilibrium, time-dependent SHS measurements of MG adsorption to sulfate-functionalized polystyrene microspheres have been reported.³² These studies find that the adsorption process actually consists of two steps: a fast-step for the initial adsorption of MG via electrostatic interactions, and a slower step attributed to hydrophobic interactions between MG and the surface. Data presented in Figure 4.4 were measured immediately after sample preparation. To ascertain any differences in the SH intensity

as MG is left to interact with ZIF-8, we probed the same samples 24 hours later. A comparison of the data taken right after sample preparation and in the following day are shown in Figure 4.5.

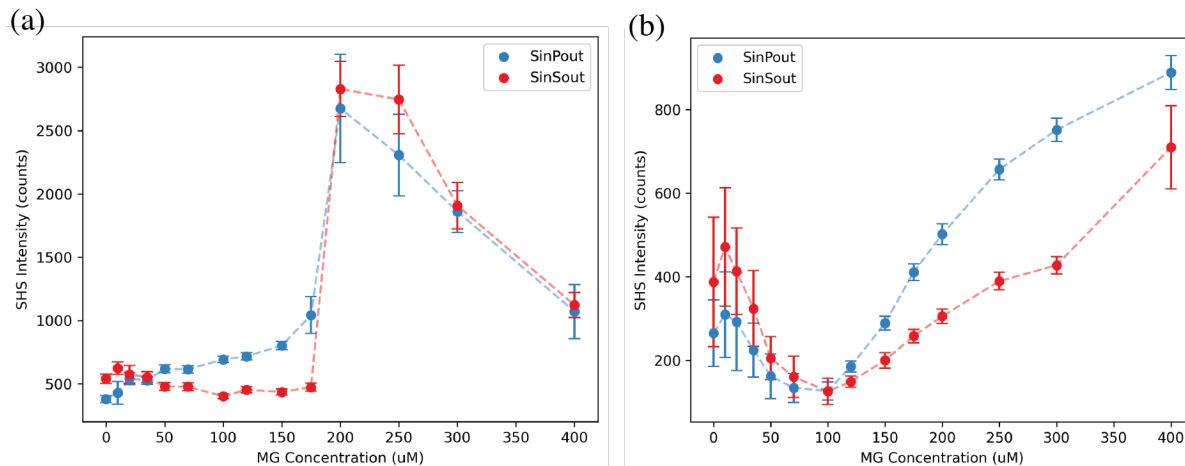


Figure 4.5. (a) SH intensity as a function of MG concentration for 0.1 mg/mL ZIF-8. The red data points represent the SinSout polarization configuration, and the blue points represent the SinPout polarization configuration. (b) Same as (a) but SH signal measured 24 hours after sample preparation.

The maximum observed in Figure 4.5 (a) (~ 200 uM) decays overnight and is replaced with a minimum at 100 uM. The SH intensity corresponding to MG concentrations greater than 100 uM increases with a more familiar S-shape, approaching a plateau at high concentrations, greater than 400 uM. We attribute the change of the calibration curve to the ZIF-8 and MG solutions reaching equilibrium. The minimum at 100 uM may be due to competing incoherent processes as discussed for pSNP, as the pores are filled and MG aligns in an optimal orientation. Also of note, the p-out polarized signal is greater than the s-out signal at concentrations higher than 100 uM, whereas it was lower than the s-out signal when measured immediately after sample preparation. This could indicate that after 24 hours, signal from MG at the surface dominates the response. Notably, in both calibration curves, Figure 4.5 (a) and (b), the polarization configuration that contributes the highest SH response changes after the maximum (200 uM) or minimum (100 uM). To better understand the importance of these polarization responses, we employed polarization-resolved SHS (Figure 4.6).

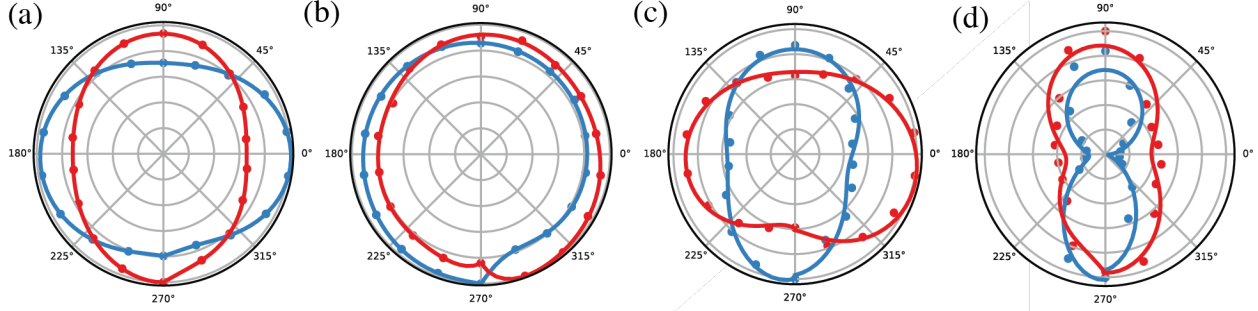


Figure 4.6. Polar plots of the SH response as a function of the polarization of the incident fundamental light at MG concentrations of (a) 50 uM, (b) 100 uM, (c) 200 uM, and (d) 250 uM. Red data points correspond to the p-out polarized response. Blue data points represent the s-out polarized response. Lines connecting the data serve only as a guide to the eye.

The polarization-dependent SH response for MG in solution with ZIF-8 was recorded for 4 different concentrations of MG by varying the laser incident polarization angle. At 50 uM MG, the s-polarized output reaches a maximum when the incident light is polarized 0 ° or 180 °, while the p-polarized output reaches a maximum at 90 ° or 270 °. For a solution containing 100 uM MG, the SH response is independent of polarization, shown by the circular polar plot in Figure 4.6 (b). When we probe a solution of ZIF-8 and 200 uM MG, the concentration at which the calibration curve exhibits a rapid increase in intensity, we observe an odd “flip” in the polarization-dependent SH response. The s-polarized response is most intense when the incident light is polarized 90 °, and the p-polarized response reaches a maximum when the incident light is polarized 0 °. Molecules with C_{2v} symmetry, e.g.. MG, exhibit a dipolar response like in Figure 4.6 (a). The second-order hyperpolarizability of MG ($\beta^{(2)}$) can be expressed as three independent tensor elements, β_{zzz} , β_{zxx} , and β_{xzx} due to the C_{2v} symmetry.³³ Kikteva et al. found that for a 800 nm fundamental incident field, two of the tensor elements dominate the polarization-dependent response, β_{zxx} , and β_{xzx} .³⁴ The nonlinear hyperpolarizability can be related to the nonlinear susceptibility by

$$\chi_s^{(2)} = N_s \langle \beta^{(2)} \rangle, \quad (4.2)$$

where N_s is the number of molecules adsorbed to the surface. A sum average over the orientations of those adsorbed molecules provides the total nonlinear susceptibility. This relation along with polarization-dependent measurements at 0 , 45 , and 90 ° polarized outputs has allowed for the determination of the orientation of MG at the Si-SiO₂ – water interface, as described by Gassin et al. as well as MG at the air-silica interface.^{33,34} While the data presented in Figure 4.6 don’t allow for a quantitative determination of MG orientation at the ZIF-8 surface, we can utilize Equation 4.2 to make some inferences about our results. The change in the polarization-dependence shown in Figure 4.6 implies that a change in $\chi_s^{(2)}$ occurs with increasing concentration. While an increasing concentration could increase N_s , the number of molecules is a scalar value, and therefore only effects the amplitude of $\chi_s^{(2)}$, and while we do observe changes in the amplitude, we are more interested in the changing polarization pattern. Thus, the “flip” in the polarization response is most likely due to the average hyperpolarizability or orientation of adsorbed molecules changing. Therefore, we attribute the polarization-dependence as a function of MG concentration to MG adopting an aligned or “preferred” orientation at 200 uM, corresponding to the

concentration at which maximum SH intensity was observed in the calibration curves (Figure 4.4 (b)).

4.4 Conclusions

Within this chapter, we discussed new methods for examining porous colloidal systems *in situ* with SHS. Angle-resolved SHS measurements of pSNP showed that the scattering pattern may not depend solely on the diameter of the studied particles. Moreover, the scattering patterns of porous surfaces may be more susceptible to exhibiting “hot spots”, or fluctuations, in the forward direction, which may be attributed to the formation of clusters or aggregates. In examining the SH response as a function of MG concentration in solution with microporous ZIF-8, we found that there were certain concentrations (200 or 900 μM) corresponding to the amount of ZIF-8, for which the SH response rapidly increased. A qualitative analysis of polarization-dependent measurements revealed that a change in the polarization dependence may be due to MG molecules preferentially aligning to the surface of ZIF-8 at 200 μM . To quantitatively describe the interactions between MG and ZIF-8, future work could resume the polarization-resolved experiments, measuring the SH response as a function of the laser incident polarization angle at all three output polarization angles, as described by Gassin et al. (0°, 45°, and 90°).³³ This would allow for fitting to an equation so that the dominant nonlinear susceptibility tensor elements may be determined. Relating these terms back to the hyperpolarizability can provide information about the tilt and azimuthal angle MG adopts at various interfaces. Still, theory that explicitly considers a rough or porous surface is needed to fully understand these systems. Ideally, this work and future nonlinear studies on MOFs or porous materials will inform development of such theories.

References

- (1) Furukawa, H.; Cordova, K. E.; O’Keeffe, M.; Yaghi, O. M. The Chemistry and Applications of Metal-Organic Frameworks. *Science* **2013**, *341* (6149), 1230444. <https://doi.org/10.1126/science.1230444>.
- (2) Mahajan, S.; Lahtinen, M. Recent Progress in Metal-Organic Frameworks (MOFs) for CO₂ Capture at Different Pressures. *Journal of Environmental Chemical Engineering* **2022**, *10* (6), 108930. <https://doi.org/10.1016/j.jece.2022.108930>.
- (3) Martínez-Ahumada, E.; Díaz-Ramírez, M. L.; Velásquez-Hernández, M. de J.; Jancik, V.; Ibarra, I. A. Capture of Toxic Gases in MOFs: SO₂, H₂S, NH₃ and NO_x. *Chem. Sci.* **2021**, *12* (20), 6772–6799. <https://doi.org/10.1039/D1SC01609A>.
- (4) Furukawa, H.; Gándara, F.; Zhang, Y.-B.; Jiang, J.; Queen, W. L.; Hudson, M. R.; Yaghi, O. M. Water Adsorption in Porous Metal–Organic Frameworks and Related Materials. *J. Am. Chem. Soc.* **2014**, *136* (11), 4369–4381. <https://doi.org/10.1021/ja500330a>.
- (5) Xu, W.; Yaghi, O. M. Metal–Organic Frameworks for Water Harvesting from Air, Anywhere, Anytime. *ACS Cent. Sci.* **2020**, *6* (8), 1348–1354. <https://doi.org/10.1021/acscentsci.0c00678>.
- (6) Samanta, P.; Desai, A. V.; Let, S.; Ghosh, S. K. Advanced Porous Materials for Sensing, Capture and Detoxification of Organic Pollutants toward Water Remediation. *ACS Sustainable Chem. Eng.* **2019**, *7* (8), 7456–7478. <https://doi.org/10.1021/acssuschemeng.9b00155>.
- (7) Yan, C.; Jin, J.; Wang, J.; Zhang, F.; Tian, Y.; Liu, C.; Zhang, F.; Cao, L.; Zhou, Y.; Han, Q. Metal–Organic Frameworks (MOFs) for the Efficient Removal of Contaminants from Water: Underlying Mechanisms, Recent Advances, Challenges, and Future Prospects. *Coordination Chemistry Reviews* **2022**, *468*, 214595. <https://doi.org/10.1016/j.ccr.2022.214595>.

- (8) Chao, Y.; Deng, N.; Zhou, Z. A Review of Recent Advances in Metal-Organic Frameworks Materials for Zero-Energy Passive Adsorption of Chemical Pollutants in Indoor Environments. *Science of The Total Environment* **2024**, *953*, 175926. <https://doi.org/10.1016/j.scitotenv.2024.175926>.
- (9) Karmakar, A.; Velasco, E.; Li, J. Metal-Organic Frameworks as Effective Sensors and Scavengers for Toxic Environmental Pollutants. *National Science Review* **2022**, *9* (7), nwac091. <https://doi.org/10.1093/nsr/nwac091>.
- (10) Davey, A. K.; Gao, X.; Xia, Y.; Li, Z.; Dods, M. N.; Delacruz, S.; Pan, A.; Swamy, S.; Gardner, D.; Carraro, C.; et al. Amine-Functionalized Metal-Organic Framework ZIF-8 toward Colorimetric CO₂ Sensing in Indoor Air Environment. *Sensors and Actuators B: Chemical* **2021**, *344*, 130313. <https://doi.org/10.1016/j.snb.2021.130313>.
- (11) Jones, C. W. Metal–Organic Frameworks and Covalent Organic Frameworks: Emerging Advances and Applications. *JACS Au* **2022**, *2* (7), 1504–1505. <https://doi.org/10.1021/jacsau.2c00376>.
- (12) Li, H.; Eddaoudi, M.; O’Keeffe, M.; Yaghi, O. M. Design and Synthesis of an Exceptionally Stable and Highly Porous Metal-Organic Framework. *Nature* **1999**, *402* (6759), 276–279. <https://doi.org/10.1038/46248>.
- (13) Cravillon, J.; Münzer, S.; Lohmeier, S.-J.; Feldhoff, A.; Huber, K.; Wiebcke, M. Rapid Room-Temperature Synthesis and Characterization of Nanocrystals of a Prototypical Zeolitic Imidazolate Framework. *Chem. Mater.* **2009**, *21* (8), 1410–1412. <https://doi.org/10.1021/cm900166h>.
- (14) Troyano, J.; Carné-Sánchez, A.; Avci, C.; Imaz, I.; Maspoch, D. Colloidal Metal–Organic Framework Particles: The Pioneering Case of ZIF-8. *Chem. Soc. Rev.* **2019**, *48* (23), 5534–5546. <https://doi.org/10.1039/C9CS00472F>.
- (15) Yang, N.; Angerer, W. E.; Yodh, A. G. Angle-Resolved Second-Harmonic Light Scattering from Colloidal Particles. *Phys. Rev. Lett.* **2001**, *87* (10), 103902. <https://doi.org/10.1103/PhysRevLett.87.103902>.
- (16) De Beer, A. G. F.; Roke, S. Obtaining Molecular Orientation from Second Harmonic and Sum Frequency Scattering Experiments in Water: Angular Distribution and Polarization Dependence. *Journal of Chemical Physics* **2010**, *132* (23), 234702–234702. <https://doi.org/10.1063/1.3429969>.
- (17) Van Cleuvenbergen, S.; Smith, Z. J.; Deschaume, O.; Bartic, C.; Wachsmann-Hogiu, S.; Verbiest, T.; van der Veen, M. A. Morphology and Structure of ZIF-8 during Crystallisation Measured by Dynamic Angle-Resolved Second Harmonic Scattering. *Nat Commun* **2018**, *9* (1), 3418. <https://doi.org/10.1038/s41467-018-05713-4>.
- (18) Dadap, J. I.; De Aguiar, H. B.; Roke, S. Nonlinear Light Scattering from Clusters and Single Particles. *The Journal of Chemical Physics* **2009**, *130* (21), 214710. <https://doi.org/10.1063/1.3141383>.
- (19) Flores, D.; Almeida, C. M. R.; Gomes, C. R.; Balula, S. S.; Granadeiro, C. M. Tailoring of Mesoporous Silica-Based Materials for Enhanced Water Pollutants Removal. *Molecules* **2023**, *28* (10), 4038. <https://doi.org/10.3390/molecules28104038>.
- (20) Baliś, A.; Lorens, D.; Gut, A.; Zapotoczny, S. Water-Dispersable Photoreactors Based on Core–Shell Mesoporous Silica Particles. *Sci Rep* **2024**, *14* (1), 11257. <https://doi.org/10.1038/s41598-024-61750-8>.
- (21) Brigante, M.; Pecini, E.; Avena, M. Magnetic Mesoporous Silica for Water Remediation: Synthesis, Characterization and Application as Adsorbent of Molecules and Ions of

- Environmental Concern. *Microporous and Mesoporous Materials* **2016**, *230*, 1–10.
<https://doi.org/10.1016/j.micromeso.2016.04.032>.
- (22) Delaney, P.; Healy, R. M.; Hanrahan, J. P.; Gibson, L. T.; Wenger, J. C.; Morris, M. A.; Holmes, J. D. Porous Silica Spheres as Indoor Air Pollutant Scavengers. *J Environ Monit* **2010**, *12* (12), 2244–2251. <https://doi.org/10.1039/c0em00226g>.
- (23) Wei, Y.; Yang, W.; Yang, Z. An Excellent Universal Catalyst Support-Mesoporous Silica: Preparation, Modification and Applications in Energy-Related Reactions. *International Journal of Hydrogen Energy* **2022**, *47* (16), 9537–9565. <https://doi.org/10.1016/j.ijhydene.2022.01.048>.
- (24) Yu, X.; Williams, C. T. Recent Advances in the Applications of Mesoporous Silica in Heterogeneous Catalysis. *Catal. Sci. Technol.* **2022**, *12* (19), 5765–5794.
<https://doi.org/10.1039/D2CY00001F>.
- (25) Cherevotan, A.; Raj, J.; Peter, S. C. An Overview of Porous Silica Immobilized Amines for Direct Air CO₂ Capture. *J. Mater. Chem. A* **2021**, *9* (48), 27271–27303.
<https://doi.org/10.1039/D1TA05961K>.
- (26) Kishor, R.; Ghoshal, A. K. Amine-Modified Mesoporous Silica for CO₂ Adsorption: The Role of Structural Parameters. *Ind. Eng. Chem. Res.* **2017**, *56* (20), 6078–6087.
<https://doi.org/10.1021/acs.iecr.7b00890>.
- (27) Zhang, H.; Hou, J.; Hu, Y.; Wang, P.; Ou, R.; Jiang, L.; Liu, J. Z.; Freeman, B. D.; Hill, A. J.; Wang, H. Ultrafast Selective Transport of Alkali Metal Ions in Metal Organic Frameworks with Subnanometer Pores. *Sci. Adv.* **2018**, *4* (2), eaaq0066.
<https://doi.org/10.1126/sciadv.aaq0066>.
- (28) Roke, S.; Gonella, G. Nonlinear Light Scattering and Spectroscopy of Particles and Droplets in Liquids. *Annual Review of Physical Chemistry* **2012**, *63*, 353–378.
<https://doi.org/10.1146/annurev-physchem-032511-143748>.
- (29) Kramer Campen, R.; Zheng, D. S.; Wang, H. F.; Borguet, E. Second Harmonic Generation as a Probe of Multisite Adsorption at Solid - Liquid Interfaces of Aqueous Colloid Suspensions. *Journal of Physical Chemistry C* **2007**, *111* (25), 8805–8813.
<https://doi.org/10.1021/jp061730h>.
- (30) van der Veen, M. A.; Valev, V. K.; Verbiest, T.; De Vos, D. E. In Situ Orientation-Sensitive Observation of Molecular Adsorption on a Liquid/Zeolite Interface by Second-Harmonic Generation. *Langmuir* **2009**, *25* (8), 4256–4261. <https://doi.org/10.1021/la8039785>.
- (31) Lin, K.-Y. A.; Chang, H.-A. Ultra-High Adsorption Capacity of Zeolitic Imidazole Framework-67 (ZIF-67) for Removal of Malachite Green from Water. *Chemosphere* **2015**, *139*, 624–631. <https://doi.org/10.1016/j.chemosphere.2015.01.041>.
- (32) Kim, J. H. Two-Step Adsorption Kinetics of Malachite Green on Anionic Polystyrene Microspheres in Aqueous Solution Probed by Second Harmonic Generation. *Phys. Chem. Chem. Phys.* **2017**, *19* (32), 21887–21892. <https://doi.org/10.1039/C7CP03088F>.
- (33) Gassin, P.-M.; Martin-Gassin, G.; Prelot, B.; Zajac, J. How to Distinguish Various Components of the SHG Signal Recorded from the Solid/Liquid Interface? *Chemical Physics Letters* **2016**, *664*, 50–55. <https://doi.org/10.1016/j.cplett.2016.09.081>.
- (34) Kikteva, T.; Star, D.; Leach, G. W. Optical Second Harmonic Generation Study of Malachite Green Orientation and Order at the Fused-Silica/Air Interface. *J. Phys. Chem. B* **2000**, *104* (13), 2860–2867. <https://doi.org/10.1021/jp992728b>.

Chapter 5. Investigating the adsorption of non-resonant molecules to buried interfaces

5.1 Introduction

It is well known that the adsorption of molecules to colloidal aqueous interfaces is hard to characterize from typical experiments. Quantification of thermodynamic parameters such as the free energy of adsorption can be paramount for understanding the adsorption behavior of molecules. Understanding the adsorption of molecules to interfaces is essential for important problems in chemical sciences, including biology, electrochemistry, material science, and environmental chemistry. Utilizing SHG in a scattering geometry, rather than reflection, has permitted the study of a variety of colloidal systems including polystyrene spheres^{1,2}, nanoparticles^{3,4}, droplets⁵⁻⁷, and biopolymers⁸⁻¹¹. While Second Harmonic generation scattering (SHS) fulfills the surface specificity required to probe adsorption to these interfaces, it has limitations regarding the type of adsorbate molecules that can be easily probed. Traditional SHS techniques require that the adsorbate possesses a resonant molecular transition at either the fundamental or second-harmonic frequency. In 1998, Eisenthal et al. developed a SHS technique that allows for the probing of “non-resonant” molecules, such as caffeine, which lack a molecular transition at the utilized 800 nm fundamental or 400 nm second harmonic. In these *competitive adsorption* experiments, malachite green (MG), a chromophore with a transition ~ 400 nm, is displaced from sites at the interface as the concentration of competing adsorbates is increased, resulting in a loss of SHS signal.¹²⁻¹⁶ Cole et al. later extended the technique to compare the propensity of seven organic pollutants or surfactants to adsorb onto colloidal polystyrene beads (PSB) functionalized with sulfate or amine groups. They found that the competitive displacement methodology provides precise ΔG_{ads} values for non-resonant molecules and could be extended to other surfaces.¹⁷ Surfactant adsorption at oil-water interfaces has also been evaluated by tracking the displacement of MG or water molecules with decreasing SHS intensity.^{18,19} The displacement of MG from the interface and through a permeable membrane was similarly studied.²⁰ Ideally, an index of thermodynamic parameters for a variety of molecules across a variety of surfaces could be created to inform the design of efficient materials, viz. water purification membranes.

This chapter discusses the extension of the method to the study of caffeine and ascorbic acid adsorption to silica nanoparticles (SNP). These two readily available molecules, included in the study by Cole et al. allow for a facile comparison of adsorption to the two different surfaces. The adsorption of caffeine and ascorbic acid to PSB were governed by both electrostatic and van der Waals forces. Despite the charge present on the functionalized PSB, van der Waals interactions were also important, this was attributed to the low surface charge density. Caffeine adsorbed to positively charged PSB more readily than the negative surface. Interestingly, the ΔG_{ads} for ascorbic acid was similar for both the negative and positive PSB.¹⁷ Cole et al. also utilized the angle-resolved spectra to investigate the orientation of MG and naphthol yellow S (NYS) at the interface. They highlight the general usefulness of SHS for studying non-resonant molecule adsorption to a variety of surfaces. The silica surface has been a popular choice for non-linear spectroscopy studies. We expect that adsorption to SNP will act like the adsorption to the sulfate-terminated PSB due to the negative charge at the silica interface, and we choose to compare the two surfaces in this chapter. Previous studies have accentuated the importance of the silica surface as a general

model for charged mineral surfaces.^{21–23} The abundance of silica in Earth’s crust makes it an ideal mimic for geochemical systems.^{24,25}

5.2 Materials and Methods

5.2.1 Experimental Design

The details of the SHS setup are outlined in Chapter 2 and Chapter 3. For the following competitive adsorption experiments, the second harmonic radiation was measured by a rotating collection arm. Data were collected in steps of 2.5°, over a total of 180° centered about transmission. At each data point, 20 scans were measured and averaged with a counting time of 500 ms. Therefore, each concentration required 12 minutes of acquisition time.

5.2.2 Sample Preparation

Water was used as the solvent for all solutions tested and was obtained from a Millipore Milli-Q water purification system (18.2 MΩ cm at 25 °C, 4 ppb TOC). The PSB and SNP were purchased from Thermo Fisher Scientific and used as received. SNP with a diameter of 500 nm were diluted from 2% w/w to 0.01% w/w. PSB with diameters of 100 nm were diluted from 8% w/w to 0.01% w/w. The PSB was functionalized with sulfate at pH > 2 by the manufacturer and have a charge density of 5 -10%. The adsorbate MG and competitor molecules (caffeine and ascorbic acid) were used as received from Sigma-Aldrich. Suspensions were made from stock solutions of water, SNP, MG, and the competitor molecules before each scan and adjusted to a pH of 9. Solutions containing PSB were instead adjusted to a pH of 4. Aliquots of the suspensions were pipetted into a 4 mm diameter cylindrical glass vial. For the MG calibration curves, the concentration of MG was slowly increased until the SH response plateaued. For the displacement studies, the concentration of MG was fixed to 60 uM for SNP and 1 uM for PSB. The concentration of caffeine and ascorbic acid were slowly increased until the SH response plateaued. After addition of competing adsorbate, the aliquot was shaken. Solutions containing caffeine were probed within two minutes of preparation, while those containing ascorbic acid were probed after 5 minutes.

5.2.3 Analysis Methods

The displacement studies require redefining the fractional coverage term, θ_D within the modified Langmuir isotherm (Equation 2.1) discussed in Chapter 2 and 3. Section 2.3.1 discusses the idiosyncrasies of the competitive adsorption fractional coverage.

5.3 Results and Discussion

5.3.1 Adsorption of resonant malachite green

To accurately determine ΔG_{ads} of caffeine and ascorbic acid to SNP and PSB surfaces, the ΔG_{ads} of the resonant, monovalent dye MG must first be evaluated. The second harmonic signal from 30 to 70 ° was averaged and plotted as a function of MG concentration (Figure 5.1). By fitting the plot to the modified Langmuir isotherm discussed in earlier chapters (Chapter 2 and 3), the ΔG_{ads} of MG to PSB was determined to be -10.83 kcal/mol (Table 5.1). This value was in great agreement with that reported by Cole et al.¹⁷ As shown in Figure 5.1 (a), the angle-resolved SHS response is symmetric around the transmission angle (0°) and there is little error depicted by the error bars at each angle. This implies that the PSB did not aggregate during the measurements. A pH of 4 for PSB solutions was chosen for this purpose; additionally, previous studies on MG at PSB were performed at a pH 4 and allowed for facile comparison.

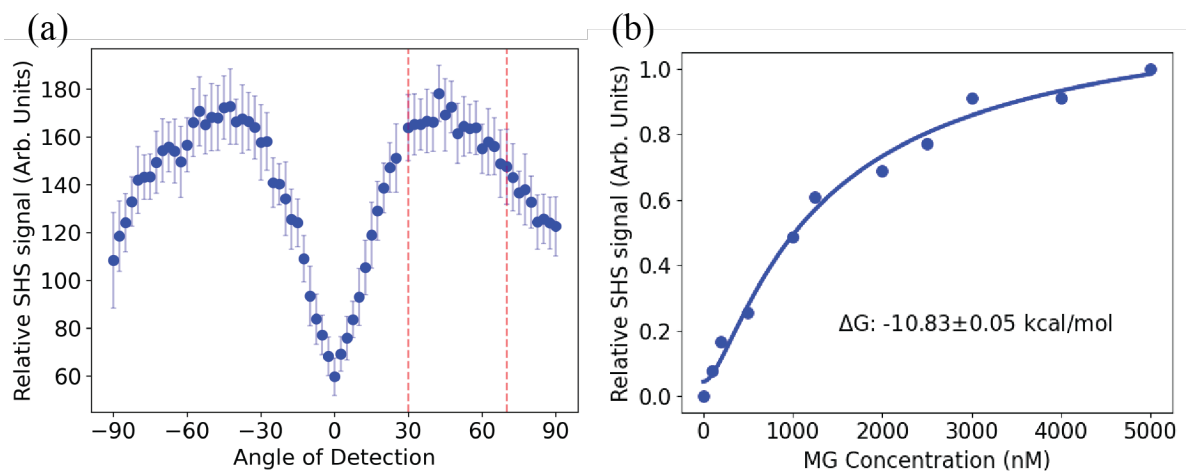


Figure 5.1. a) Angle-resolved SHS response of 1 μM MG on PSB. The scattered data in (b) represent the average of a sum over the angles of maximum SHS signal; the range is indicated by the red dashed lines ($30\text{-}70^\circ$). b) SHS intensity as a function of MG concentration. The solid line represents the fit to a Langmuir isotherm.

Similarly, the adsorption of MG to SNP was studied; the ΔG_{ads} of MG to SNP was determined to be -9.29 kcal/mol (Figure 5.2). The decrease in ΔG_{ads} can likely be attributed to the change in pH between the systems. While we expect both PSB and SNP to have negative adsorption groups, at high pH MG becomes colorless and neutral. This minimizes both the resonant enhancement from the transition at 400 nm and also results in weaker electrostatic interactions. In fact, the observed $\Delta G_{\text{ads,SNP}}$ is closer to the ΔG_{ads} of MG to positively charged PSB, reported in Chapter 3 ($\Delta G_{\text{ads,pPSB}} = -9.38$ kcal/mol). The maximum SHS signal shifts to slightly larger angles, requiring us to take an average of a sum over the angles $40 - 80^\circ$. Overall, the scatter intensity was greater for MG at the SNP surface due to the larger concentrations of MG needed to reach saturation of the surface. The error was so small that error bars are eclipsed by the data points plotted in Figure 5.2 (a). Fitting these preliminary data supplies the corresponding equilibrium constant (K_D) and maximum surface number density (N_m^D).

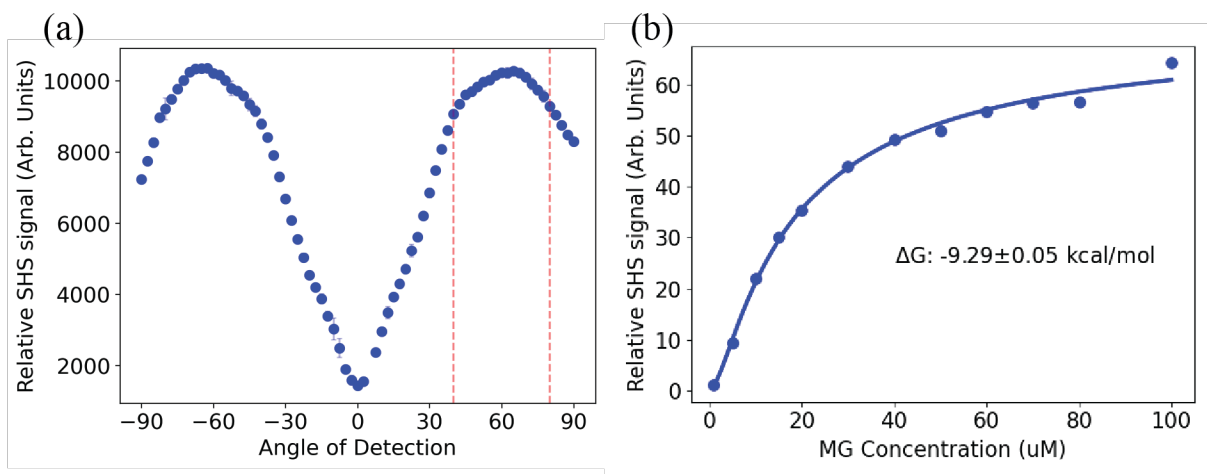


Figure 5.2. a) Angle-resolved SHS response of 60 uM MG on SNP. The scattered data in (b) represent the average of a sum over the angles of maximum SHS signal; the range is indicated by the red dashed lines (40-80°). b) SHS intensity as a function of MG concentration. The solid line represents the fit to a Langmuir isotherm.

5.3.2 Displacement Studies

To obtain the adsorption thermodynamic value ΔG_{ads} for non-resonant molecules viz. caffeine and ascorbic acid, adsorption to SNP and PSB, the displacement methodology was employed. Plots relating the concentration of non-resonant molecules to the SHGS signal are realized from the angle-resolved data as outlined above (Figure 5.3 and 5.4). The observed decrease in SHS signal with increasing concentration of caffeine or ascorbic acid reflects the displacement of previously adsorbed MG, which has a greater propensity for the surface than the competing molecules (Table 1).

Table 5.1. ΔG_{ads} of MG and competing adsorbates to SNP vs PSB

Adsorbate	SNP (pH 9)	PSB (pH 4)
MG	-9.29 ± 0.05 kcal/mol	-10.83 ± 0.05 kcal/mol
Caffeine	-5.51 ± 0.14 kcal/mol	-4.37 ± 0.22 kcal/mol
Ascorbic acid	-8.89 ± 0.20 kcal/mol	-5.81 ± 0.18 kcal/mol

To fit the modified Langmuir model to these seemingly inverted data, the fractional coverage term becomes:

$$\theta = \frac{x}{1 + x + y}$$

$$x = K_D \times \frac{(C_D - N_m^D)}{55.5}, \quad y = K_C \times \frac{(C_C - N_m^C)}{55.5} \quad (5.1)$$

Further details of the modified term (Equation 5.1) are included in Chapter 2. Briefly, the competitor molecules' equilibrium constant (K_C), is determined by setting $N_m^C = N_m^D$ in the fitting procedure when relatively large amounts of the competitor molecule are needed to displace MG. Under these limitations, the assumption that an adsorption site will only adsorb either MG or a

competing molecule is realized. Similar assumptions have been utilized in previous displacement studies and are proven to provide meaningful K_C values.^{8,17} The Langmuir isotherm, while valuable in its ability to accurately determine adsorption thermodynamics, greatly oversimplifies the true chemical nature of the surface environment. Additional assumptions made under this fitting scheme include defining all surface sites as chemically equivalent and neglecting any adsorbate-adsorbate or adsorbate-competitor interactions.

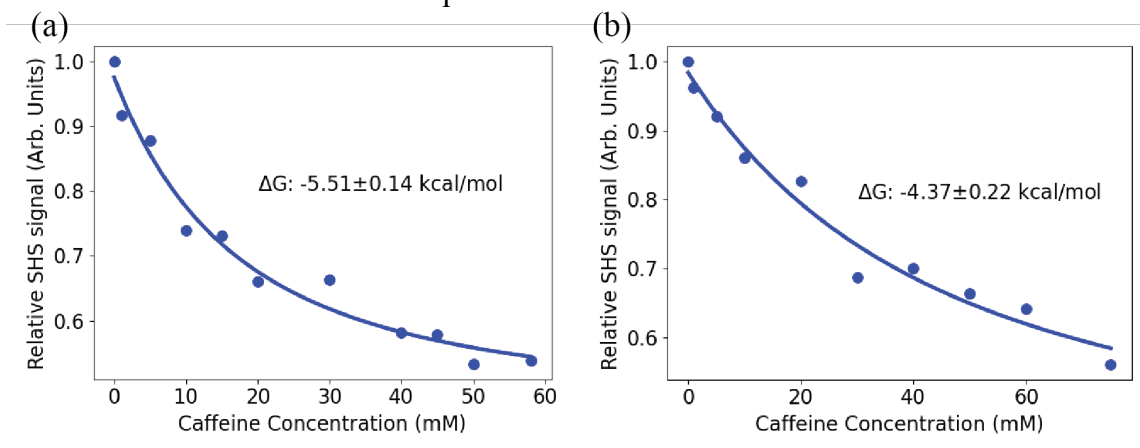


Figure 5.3. Adsorption of caffeine by displacement of MG to (a) SNP and (b) PSB.

The adsorption of caffeine is less favorable than the adsorption of MG to SNP and PSB (Figure 5.3). Additionally, the adsorption of caffeine is slightly enhanced at the SNP surface relative to the PSB surface. The difference in ΔG_{ads} is less than ~ 1 kcal/mol, which is on the order of uncertainty for ΔG_{ads} determined by other methods *viz.* adiabatic calorimetry and UV adsorption spectroscopy. The displacement method allows us to effectively probe non-resonant molecules across different surfaces, as our reported uncertainties are less than 0.25 kcal/mol (Table 5.1). Caffeine (Figure 5.5 (b)) is neutrally charged across all pHs used in this experiment. The small but notable difference in ΔG_{ads} must then be attributed to the difference in adsorption environment at the surface. While the negatively charged PSB surface has a charge density of only about 5-10%, implying more of the polystyrene backbone is available for van der Waals interactions with the caffeine, the ΔG_{ads} is more negative for adsorption to SNP. This may be because SNP has more functional silanol groups on the surface that can hydrogen bond to caffeine molecules.

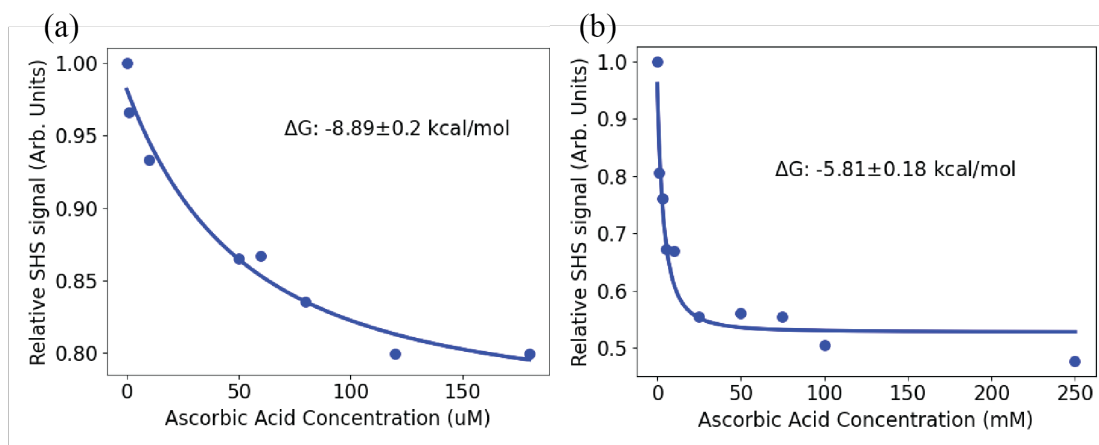


Figure 5.4. Adsorption of ascorbic acid by displacement of MG to (a) SNP and (b) PSB.

Second to the ΔG_{ads} of MG to PSB and SNP, adsorption of ascorbic acid to SNP was the most favorable, and surprisingly greatly enhanced relative to adsorption to PSB. The ΔG_{ads} differs by ~ 3 kcal/mol (Table 5.1). Ascorbic acid (Figure 5.5 (b)) has a $\text{pK}_a = 4.17$ and is deprotonated at the pH of the SNP suspensions. The deprotonated form, ascorbate anion, is stabilized by its resonance structures. Under these conditions, we would expect the ΔG_{ads} to be less favorable due to the repulsive electrostatic interactions between the negative charge on the ascorbic acid and the negative charge of the SNP surface. As discussed in Chapter 3, for systems lacking attractive electrostatic interactions, like when the adsorbate and surface are similarly charged, van der Waals interactions dominate the adsorption mechanism. The ΔG_{ads} of ascorbic acid for negatively charged PSB is -5.81 kcal/mol, which is closer to the ΔG_{ads} of ascorbic acid adsorbing to positively charged PSB, as reported by Cole et al. (-4.06 kcal/mol).¹⁷ Both of these systems were studied at a pH of 4 or less. This implies that the pH effect is responsible for the enhancement at the SNP surface, which may be attributed to ion pairing with the cationic MG. Ion pairing contradicts the assumptions we make in fitting the data to a Langmuir isotherm, which assumes that adsorbate molecules don't interact. Additionally, the formation of a MG-ascorbic acid complex would most likely result in noisy angle-resolved measurements, which were not observed for this experiment. It is also possible, that due to the delocalization of the negative charge, the repulsive electrostatics are small. We could reach a similar conclusion as discussed for caffeine adsorption to SNP, in which the carbonyl or alkoxide groups may hydrogen bond to the silica surface. However, the increase of available hydrogen bonding sites introduced by SNP only accounts for ~ 1 kcal/mol. Additional SHGS techniques could provide useful information that could deconvolute the enhancement of ascorbic acid, viz. the χ^3 method, which can discern the charge density or pK_a at the interface.^{24,26-28}

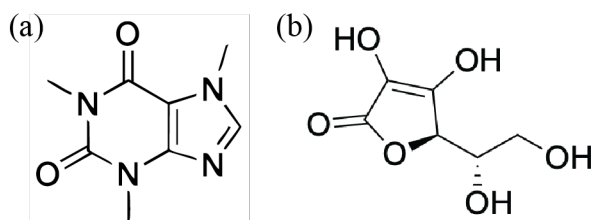


Figure 5.5. Chemical structures of caffeine (a) and ascorbic acid (b).

5.4 Conclusions

In summary, a comparison of the adsorption thermodynamics of non-resonant molecules across differently structured surfaces can be realized with a competitive displacement methodology. We find that we can resolve the difference in ΔG_{ads} for caffeine on SNP and negatively functionalized PSB, which amounts to ~ 1 kcal/mol. This result implies that this method is useful for developing a robust understanding of adsorption of non-resonant molecules at various functionalized interfaces. Interestingly, we conclude that ascorbic acid in alkaline solution has a very favorable adsorption to SNP despite the similar charge between the surface and adsorbate, and we attribute this observation to ion pairing.

References

- (1) Schürer, B.; Peukert, W. In Situ Surface Characterization of Polydisperse Colloidal Particles by Second Harmonic Generation. *Particulate Science and Technology* **2010**, *28* (5), 458–471. <https://doi.org/10.1080/02726351.2010.504131>.
- (2) Jen, S. H.; Gonella, G.; Dai, H. L. The Effect of Particle Size in Second Harmonic Generation from the Surface of Spherical Colloidal Particles. i: Experimental Observations. *Journal of Physical Chemistry A* **2009**, *113* (16), 4758–4762. <https://doi.org/10.1021/jp9009959>.
- (3) Gassin, P.-M. M.; Bellini, S.; Zajac, J.; Martin-Gassin, G. Adsorbed Dyes onto Nanoparticles: Large Wavelength Dependence in Second Harmonic Scattering. *Journal of Physical Chemistry C* **2017**, *121* (27), 14566–14571. <https://doi.org/10.1021/acs.jpcc.7b00703>.
- (4) Karam, T. E.; Haber, L. H. Molecular Adsorption and Resonance Coupling at the Colloidal Gold Nanoparticle Interface. *Journal of Physical Chemistry C* **2014**, *118* (1), 642–649. <https://doi.org/10.1021/jp410128v>.
- (5) Vácha, R.; Rick, S. W.; Jungwirth, P.; de Beer, A. G. F.; de Aguiar, H. B.; Samson, J.-S.; Roke, S. The Orientation and Charge of Water at the Hydrophobic Oil Droplet–Water Interface. *J. Am. Chem. Soc.* **2011**, *133* (26), 10204–10210. <https://doi.org/10.1021/ja202081x>.
- (6) de Aguiar, H. B.; de Beer, A. G. F.; Strader, M. L.; Roke, S. The Interfacial Tension of Nanoscopic Oil Droplets in Water Is Hardly Affected by SDS Surfactant. *J. Am. Chem. Soc.* **2010**, *132* (7), 2122–2123. <https://doi.org/10.1021/ja9095158>.
- (7) de Aguiar, H. B.; Strader, M. L.; de Beer, A. G. F.; Roke, S. Surface Structure of Sodium Dodecyl Sulfate Surfactant and Oil at the Oil-in-Water Droplet Liquid/Liquid Interface: A Manifestation of a Nonequilibrium Surface State. *J. Phys. Chem. B* **2011**, *115* (12), 2970–2978. <https://doi.org/10.1021/jp200536k>.
- (8) Eckenrode, H. M.; Dai, H.-L. Nonlinear Optical Probe of Biopolymer Adsorption on Colloidal Particle Surface: Poly-L-Lysine on Polystyrene Sulfate Microspheres. *Langmuir* **2004**, *20* (21), 9202–9209. <https://doi.org/10.1021/la048863j>.
- (9) Liu, J.; Subir, M.; Nguyen, K.; Eienthal, K. B. Second Harmonic Studies of Ions Crossing Liposome Membranes in Real Time. *J Phys Chem B* **2008**, *112* (48), 15263–15266. <https://doi.org/10.1021/jp806690z>.
- (10) Liu, Y.; Yan, E. C. Y.; Eienthal, K. B. Effects of Bilayer Surface Charge Density on Molecular Adsorption and Transport across Liposome Bilayers. *Biophysical Journal* **2001**, *80* (2), 1004–1012. [https://doi.org/10.1016/S0006-3495\(01\)76079-1](https://doi.org/10.1016/S0006-3495(01)76079-1).
- (11) Srivastava, A.; Eienthal, K. B. Kinetics of Molecular Transport across a Liposome Bilayer. *Chemical Physics Letters* **1998**, *292* (3), 345–351. [https://doi.org/10.1016/S0009-2614\(98\)00662-9](https://doi.org/10.1016/S0009-2614(98)00662-9).
- (12) Wang, H.; Yan, E. C. Y.; Borguet, E.; Eienthal, K. B. *Second Harmonic Generation from the Surface of Centrosymmetric Particles in Bulk Solution*; 1996; Vol. 259, pp 15–20.
- (13) Wang, H.; Yan, E. C. Y.; Liu, Y.; Eienthal, K. B. *Energetics and Population of Molecules at Microscopic Liquid and Solid Surfaces*; 1998. <https://pubs.acs.org/sharingguidelines>.
- (14) Wang, H.; Troxler, T.; Yeh, A. G.; Dai, H. L. In Situ, Nonlinear Optical Probe of Surfactant Adsorption on the Surface of Microparticles in Colloids. *Langmuir* **2000**, *16* (6), 2475–2481. <https://doi.org/10.1021/la9909087>.

- (15) Eisenthal, K. B. Second Harmonic Spectroscopy of Aqueous Nano- and Microparticle Interfaces. *Chemical Reviews* **2006**, *106* (4), 1462–1477. <https://doi.org/10.1021/cr0403685>.
- (16) Salafsky, J. S.; Eisenthal, K. B. Protein Adsorption at Interfaces Detected by Second Harmonic Generation. *J. Phys. Chem. B* **2000**, *104* (32), 7752–7755. <https://doi.org/10.1021/jp001294d>.
- (17) Cole, W. T. S.; Wei, H.; Nguyen, S. C.; Harris, C. B.; Miller, D. J.; Saykally, R. J. Dynamics of Micropollutant Adsorption to Polystyrene Surfaces Probed by Angle-Resolved Second Harmonic Scattering. *Journal of Physical Chemistry C* **2019**, *123* (23), 14362–14369. <https://doi.org/10.1021/acs.jpcc.9b01146>.
- (18) Sang, Y.; Yang, F.; Chen, S.; Xu, H.; Zhang, S.; Yuan, Q.; Gan, W. Molecular Interactions at the Hexadecane/Water Interface in the Presence of Surfactants Studied with Second Harmonic Generation. *The Journal of Chemical Physics* **2015**, *142* (22), 224704. <https://doi.org/10.1063/1.4922304>.
- (19) Liang, Y.; Zhang, S.; Wu, W.; Yang, F.; Gan, W.; Jia, H.; Chen, S.; Zhu, X.; Yuan, Q. Lyophobicity May Not Be the Main Driving Force for Long Chain Surfactants from the Bulk Phase to the Interface. *Phys. Chem. Chem. Phys.* **2018**, *20* (15), 10165–10172. <https://doi.org/10.1039/C7CP07322D>.
- (20) Sharifian Gh., M.; Wilhelm, M. J.; Dai, H.-L. Azithromycin-Induced Changes to Bacterial Membrane Properties Monitored *in Vitro* by Second-Harmonic Light Scattering. *ACS Med. Chem. Lett.* **2018**, *9* (6), 569–574. <https://doi.org/10.1021/acsmchemlett.7b00499>.
- (21) Olson, A. L.; Alghamdi, A. O.; Geiger, F. M. NaCl, MgCl₂, and AlCl₃ Surface Coverages on Fused Silica and Adsorption Free Energies at pH 4 from Nonlinear Optics. *J. Phys. Chem. A* **2024**, *128* (11), 2162–2168. <https://doi.org/10.1021/acs.jpca.4c00514>.
- (22) Ma, E.; Geiger, F. M. Divalent Ion Specific Outcomes on Stern Layer Structure and Total Surface Potential at the Silica:Water Interface. *J. Phys. Chem. A* **2021**, *125* (46), 10079–10088. <https://doi.org/10.1021/acs.jpca.1c08143>.
- (23) Bañuelos, J. L.; Borguet, E.; Brown, G. E.; Cygan, R. T.; DeYoreo, J. J.; Dove, P. M.; Gaigeot, M.-P.; Geiger, F. M.; Gibbs, J. M.; Grassian, V. H.; et al. Oxide– and Silicate–Water Interfaces and Their Roles in Technology and the Environment. *Chem. Rev.* **2023**, *123* (10), 6413–6544. <https://doi.org/10.1021/acs.chemrev.2c00130>.
- (24) Rehl, B.; Rashwan, M.; DeWalt-Kerian, E. L.; Jarisz, T. A.; Darlington, A. M.; Hore, D. K.; Gibbs, J. M. New Insights into $\chi^{(3)}$ Measurements: Comparing Nonresonant Second Harmonic Generation and Resonant Sum Frequency Generation at the Silica/Aqueous Electrolyte Interface. *J. Phys. Chem. C* **2019**, *123* (17), 10991–11000. <https://doi.org/10.1021/acs.jpcc.9b01300>.
- (25) Malin, J. N.; Holland, J. G.; Saslow, S. A.; Geiger, F. M. U(VI) Adsorption and Speciation at the Acidic Silica/Water Interface Studied by Resonant and Nonresonant Second Harmonic Generation. *J. Phys. Chem. C* **2011**, *115* (27), 13353–13360. <https://doi.org/10.1021/jp203091x>.
- (26) Geiger, F. M. Second Harmonic Generation, Sum Frequency Generation, and $\chi^{(3)}$: Dissecting Environmental Interfaces with a Nonlinear Optical Swiss Army Knife. *Annual Review of Physical Chemistry* **2009**, *60* (Volume 60, 2009), 61–83. <https://doi.org/10.1146/annurev.physchem.59.032607.093651>.

- (27) Zhao, X.; Ong, S.; Wang, H.; Eiseenthal, K. B. New Method for Determination of Surface pKa Using Second Harmonic Generation. *Chemical Physics Letters* **1993**, *214* (2), 203–207. [https://doi.org/10.1016/0009-2614\(93\)90082-C](https://doi.org/10.1016/0009-2614(93)90082-C).
- (28) Ong, S.; Zhao, X.; Eiseenthal, K. B. Polarization of Water Molecules at a Charged Interface: Second Harmonic Studies of the Silica/Water Interface. *Chemical Physics Letters* **1992**, *191* (3), 327–335. [https://doi.org/10.1016/0009-2614\(92\)85309-X](https://doi.org/10.1016/0009-2614(92)85309-X).

Chapter 6. Time-Resolved X-ray Emission Spectroscopy and Resonant Inelastic X-ray Scattering Spectroscopy of Laser Irradiated Carbon

This work is adapted from Erika J. Riffe,¹ Franky Bernal,^{1,2} Chinnathambi Kamal,^{3,4} Hikaru Mizuno,^{1,2} Rebecca K. Lindsey,^{5,6} Sebastien Hamel,⁵ Sumana L. Raj,^{1,2} Christopher J. Hull,^{1,2} Soonnam Kwon,⁷ Sang Han Park,⁷ Jason K. Cooper,^{2,8} Feipeng Yang,⁹ Yi-Sheng Liu,⁹ Jinghua Guo,⁹ Dennis Nordlund,¹⁰ Walter S. Drisdell,^{2,8} Michael W. Zuerch,^{1,11} Heather D. Whitley,⁵ Michael Odelius^{12*}, Craig P. Schwartz^{2,13*}, and Richard J. Saykally^{1,2*}. “Time-Resolved X-ray Emission Spectroscopy and Resonant Inelastic X-ray Scattering Spectroscopy of Laser Irradiated Carbon” *J. Phys. Chem. B*. 2024. <https://doi.org/10.1021/acs.jpcc.4c02862>

6.1 Introduction

While the solid and gaseous states of carbon have been extensively studied, our knowledge of the liquid state is substantially less well-developed.¹ The unique ability of carbon atoms to form single, double, and triple covalent bonds through different types of hybridization effects considerable variability in the structure, and physical properties. This accounts for the variety of known allotropes, permitting industrial and technological applications ranging from industrial lubricants and batteries, to moderators in nuclear reactors.²⁻⁴ Novel carbon materials, including ultra-hard solids and carbon nanotubes, are thought to be formed from a liquid carbon state precursor.⁵⁻⁸

A better understanding of the liquid state could provide additional routes for the synthesis of novel carbon materials, analogous to how the study of small carbon clusters led to the discovery of fullerenes. The liquid state is challenging to prepare, as to obtain ‘equilibrium’ liquid carbon, transient methods such as ultrafast laser-induced non-thermal melting, must be utilized. This was first demonstrated by Malvezzi et al in the mid-1980s.⁹ Other experiments, which include x-ray absorption, and reflectivity studies at both extreme ultraviolet (EUV) and optical wavelengths, have been performed to characterize the liquid state of carbon.⁹⁻¹⁵ The literature on these “non-thermally melted” samples often reaches opposing conclusions, potentially due to the differences in sample preparation, as shown in Table 1.⁹⁻¹⁶ Note the variety of both initial sample and laser conditions employed to prepare putative liquid samples.

Optical reflectivity experiments reported by Malvezzi et al. and Reitze et al.^{9,10} were among the first reports on ultrafast non-thermal melting of carbon. Malvezzi et al.⁹ melted graphite targets with a 20 ps, 532 nm pulse from a Nd-YAG laser, and probed them using optical pulses at 532, 1064, and 1900 nm wavelengths with various delay times. Malvezzi et al. concluded that a phase transition occurred and that the resulting liquid acted as an insulator, due to the observed fluence-dependent decrease in reflectivity. The decrease was observed at fluences above 0.14 J/cm², a threshold for the surface melting.

These conclusions were challenged by Reitze et al.¹⁰ in 1989, who utilized a femtosecond laser system at similar fluences. With the improved time resolution, they observed an instantaneous increase in signal that was followed by a decay in optical reflectivity. The authors attributed the initial increase in signal (which remained for ~ 5 ps) to the formation of a liquid carbon state and argued that the increased reflectivity was evidence of a metal, rather than an insulator. Further, it

was argued that the decrease in reflectivity observed at longer time delays in their experiment was wrongfully assigned as a feature of the liquid in Malvezzi's work. Instead, the signal decrease was attributed to ablated liquid carbon, indicating that the phase transition occurred earlier.

Reitze et al.¹² repeated these femtosecond optical reflectivity experiments on diamond, utilizing a higher fluence (0.63 J/cm^2), as needed to melt the harder sample. Once again, an initial increase in reflectivity was observed, supporting the notion that liquid carbon formed from both graphite and diamond comprised a metallic state upon melting. However, Malvezzi et al.¹¹ defended their previous work by repeating the optical reflectivity experiments utilizing picosecond ellipsometry. By measuring the reflectivity with two different polarizations, the real and imaginary parts of the index of refraction of the putative liquid were obtained. The observed reduction of both the real and imaginary parts of the index of refraction indicated that the liquid phase is less metallic than the solid, and again, acts more like an insulator. The contradictions reached in these studies underscores the need for further investigation of the liquid state.

Johnson et al. studied the electronic properties of liquid carbon via x-ray absorption spectroscopy (XAS) using a synchrotron slice source.¹⁴ These early time-resolved (tr-) XAS experiments concluded that the bonding properties of the melt depended on the density of the carbon target. At lower densities, sp bonds are dominant, and as the density increases, a mixture of sp, sp² and sp³ bonding occurs. This was determined by calculating the π^* states/site and comparing the area of the π^* peak to that of the π^* peak of fullerene, which has a π^* state/atom ratio of 1 due to its purely sp² carbon bonding network. Johnson et al. also estimated a bond length change of $-0.07 \pm 0.02 \text{ \AA}$ for the highest density liquid from a blue shift in the 295.5 eV peak of solid amorphous carbon. This was confirmed by simulations in which the bond length changed from 1.45 to 1.40 \AA at 2.76 g/cm^3 and 6000 K. This shortening of the bond length was judged as being consistent with the formation of a liquid state.

In 2014, Brown et al.¹⁷ published a different pump-probe x-ray experiment on carbon, utilizing the FEL at LCLS in a warm-dense matter regime. They compared the resulting structure factor for the unheated sample (FEL pulse only) and the structure factor at various delay times to show that there is an increase in the diffraction density at 3.4 \AA^{-1} , indicating a structural change away from the initial hexagonal structure of the cold graphite sample. This peak in the structure factor reaches a maximum at $t > 30 \text{ ps}$. At this time delay, a crystalline structure should have time to form from an intermediate and influence the measurement; however, they observe no evidence of a bcc lattice or a liquid, and conclude that a glassy carbon state exists, instead of a liquid.

More recent tr-XAS experiments on liquid carbon utilized the FERMI free electron laser (FEL) facility for sub-ps time resolution. In these experiments,¹⁵ liquid carbon was determined to have metallic character because of the appearance of numerous unsaturated carbon bonds. The high-density liquid (2.0 g/cm^3) obtained by fs-driven non-thermal melting of an a-C foil was assumed to have sp hybridization, a chain-like carbon network, and a C-C bond length of ca. 1.5 \AA at extreme conditions (14200 K, 0.5 Mbar). The formation of the liquid phase occurred faster than previously reported, viz. only 0.1 ps after the melting pulse, and equilibrated within 0.3 ps. This ultrafast rearrangement of the atomic structure is due to the transformation of the electronic structure, as sp² hybridization quickly collapses and sp hybridization prevails.

Recent advances in x-ray FELs may be useful in resolving such controversies regarding the intermediate state of liquid carbon. These facilities can now supply the time-resolution, spectral-resolution, and high flux required to study samples by more photon-hungry techniques, such as x-ray emission spectroscopy (XES) and resonant inelastic x-ray scattering (RIXS).¹⁸ Both XES and RIXS are excellent probes of the electronic structure of a material. Both techniques involve the emission of an x-ray photon as a core-hole is filled by a valence electron, wherein the absorption of an X-ray photon promotes an electron from the core level into the continuum (XES), or to an empty valence band (RIXS). Furthermore, the resonance with a valence state in RIXS allows for the simultaneous determination of empty electronic states and occupied states. Here we define RIXS as measurements resonant with states below the second band gap of the target material. Therefore, XES and RIXS are sensitive to the melting dynamics and changes in bonding character of a system, as observed for the water/ice phase transition¹⁹ or the liquid-liquid transition in silicon.²⁰ These techniques have been employed previously in the study of graphite, but lacked the modern time-resolution capabilities. Herein, we present the results of an optical pump – soft x-ray probe experiment on diamond and amorphous carbon samples, accompanied by XAS and XPS measurements of the unmelted samples, and theoretical simulations. We also report the first time-resolved RIXS (tr-RIXS) and time-resolved XES (tr-XES) experiments performed on laser-melted carbon, and their spectra. Variable temperature and pressure conditions are examined by scanning different delay times between the optical melting pulse and the soft x-ray probe pulse, providing insight into the dependence of the liquid structure on temperature, pressure, and density.

Table 6.1. Reported Literature Values for non-thermal melting of carbon.

Sample	Sample Thickness	Melting Pulse wavelength	Pulse duration	Fluence (J/cm ²)	Time Delay(s) (ps)	Experiment	Reference
HOPG	---	532 nm	20 ps	0.14	60, 100, 200	Optical Reflectivity	[10]
HOPG	---	620 nm	90 fs	0.13		Optical Reflectivity	[11]
HOPG	>30 um	1060 nm	30 ps	50-350 W/cm ²	0, 60, 120	Optical Reflectivity	[12]
diamond	250 um	620 nm	90 fs	0.63	-5 – 25	Optical Reflectivity	[13]
a-C	500 Å	800 nm	150 fs	0.7-2.0	100	XAS	[15]
graphite foil	1 um	800 nm	300 fs	10 ¹⁵ W/cm ²	0 – 40	X-ray Scattering	[18]
a-C	70 nm	260 nm	100 fs	0.6	-1 - 10	EUV Reflectivity	[14]
a-C	100 nm	250 nm	130 fs	0.63		EUV Reflectivity	[17]
a-C foil	80 nm	390 nm	50-80 fs	0.4	0.52	XAS	[16]
a-C	100 nm	800 nm	65 fs	0.82	+1 - 50	Tr-RIXS	This paper
UNCD	400 nm	800 nm	65 fs	0.88	-1 - 100	Tr-RIXS	This paper

HOPG = Highly oriented pyrolytic graphite, a-C = amorphous carbon, UNCD = ultrananocrystalline diamond

6.2 Experimental Methods

Amorphous carbon (a-C) films with a thickness of 100 nm, roughness of 0.80 nm, and density of $\rho = 2.1 \text{ g cm}^{-3}$, purchased from Incoatec GmbH, were deposited on silicon <100> wafers. Ultrananocrystalline diamond (UNCD) films with a thickness of ca. 400 nm, purchased from John Crane Inc., were also deposited on silicon <100> wafers.

Tr-RIXS/tr-XES experiments were performed on both a-C and UNCD near the carbon K-edge, at the soft x-ray scattering and spectroscopy beamline at Pohang Accelerator Laboratory (PAL) x-ray FEL.¹⁸ A Ti:Sapphire laser system provided the 800 nm, 65 fs non-thermal melting pulses used in this experiment. The optical pulse had a spot size of $200 \times 200 \text{ um}^2$, much larger than the probe pulses used ($50 \times 50 \text{ um}^2$ for amorphous carbon and $80 \times 80 \text{ um}^2$ for UNCD). The pulses were roughly collinear with the PAL-XFEL pulses and were focused onto the sample surface with an incidence angle of ca. 45 degrees with respect to the sample surface normal, as shown in Figure 1. RIXS/XES performed at soft x-ray regimes has a general probe depth of 100 nm and is dependent on the sample. The samples were raster-scanned and the scattered x-ray photons were collected in a reflection geometry using a RIXS/XES spectrometer with an Andor Newton DO 940 CCD detector.

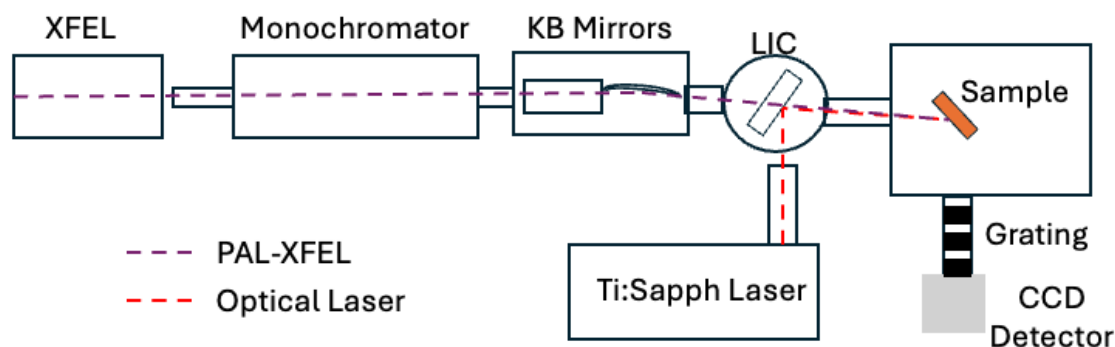


Figure 6.1. Experimental setup at the PAL-XFEL. Sample thin films are mounted on a control stage and non-thermally melted using the optical laser pulse, and then probed with the XFEL pulse. The signal is collected as a 1 x 2048-pixel image with the CCD at approximately a right angle to the laser beams.

Tr-RIXS spectra of non-thermally melted a-C samples were collected at incidence energies of 289 eV, 297 eV and 298 eV as a function of time delay between the melting pulse and PAL-XFEL pulse, ranging from $\Delta t = +1$ to $+50$ ps with a resolution of ca. 150 fs. Tr-XES/tr-RIXS spectra of non-thermally melted UNCD thin film samples were collected at incident energies of 294 eV, 303 eV, and 308 eV as a function of delay between the melting pulse and PAL-XFEL pulse, ranging from $\Delta t = -1$ to $+100$ ps. Each dataset comprised 10,000-100,000 FEL shots, with each shot saved as a 1×2048 -pixel image file. To analyze the spectra, background removal and signal filtering were performed based on the methods developed by Nowak et al.²¹ The filtered spectra were normalized by the number of shots and FEL intensity, binned, and smoothed using a smoothing spline fit. The widths of the spectra were determined by fitting them to a Gaussian and measuring the full width at half max (FWHM). The widths at each time delay were averaged and the standard deviation was calculated to quantify the narrowing or broadening across time delays.

XAS measurements of the unmelted a-C and UNCD thin films were performed at the Stanford Synchrotron Radiation Lightsource (SSRL) and the Advanced Light Source (ALS), respectively, by bulk-sensitive drain current measurements.^{22,23} Additional characterization of the unmelted samples, including XES/RIXS and x-ray photoemission spectroscopy (XPS), were also performed on BL8.0.1 at the ALS. XPS measurements were performed with a commercial $K\alpha$ x-ray photoelectron spectrometer (Thermo Fisher Scientific).

Table 6.2. Laser parameters for tr-RIXS and tr-XES experiments at PAL-XFEL.

	PAL-XFEL	Melting Laser	
		tr-RIXS a-C	tr-RIXS/XES UNCD
Spot size, fwhm (μm)	80 μm	200 μm	200 μm
Energy	289, 294, 297, 298, 303, 308 eV (pink beam)	1.55 eV / 800 nm	1.55 eV / 800 nm
Pulse duration (fs)	< 50	65	65
AOI	45°	45°	45°
Pulse Energy (μJ)	--	528	565
Peak Fluence (J cm^{-2})	--	0.82	0.88
Peak power (W cm^{-2})	--	1.3×10^{13}	1.4×10^{13}

6.3 Theoretical Methods

Periodic DFT-based electronic structure calculations, within the generalized gradient approximation given by Perdew-Burke-Ernzerhof (PBE), including a van der Waals correction using Grimme's D3 method²⁴, have been performed using the CP2K package²⁵ to simulate the carbon *K*-edge XAS and XES spectra for diamond, graphite, and amorphous carbon using configurations from the MD trajectories. A Gaussian Augmented Plane Wave (GAPW) method to perform all-electron calculations with a 6-311Gdp basis set and an energy cut-off of 500 Ry using a multi-grid framework consisting of five grids was employed. Super-cells of $5 \times 5 \times 5$ (1000 atoms), $8 \times 8 \times 3$ (768 atoms), and a ~ 17 Å sized cubic box (500 atoms) for diamond, graphite, and a-C were used, respectively. Representative configurations for amorphous carbon were generated using the LAMMPS²⁶ molecular dynamics (MD) simulator with a Chebyshev Interaction Model for Efficient Simulation (ChIMES)²⁷ potential for liquid carbon. The ChIMES model accounts for two- and three-body interactions by fitting linear combinations of Chebyshev polynomials through force matching to trajectories from Kohn-Sham density functional theory (DFT).²⁸ The ChIMES model employed here was parameterized based on force matching DFT simulations at temperatures of 5,000-20,000 K and densities of 1.0-3.6 g/cc, and has recently been further refined and validated for a variety of scenarios involving carbon at extreme conditions.²⁹ Trajectories were obtained at a density of 2.1 g/cc, based on the initial density of amorphous carbon in the experiments, at temperatures of 7000 K, 14000 K, and 17000 K. We sampled 100 snapshots of 500 atoms per simulation, with a spacing of 250 fs between snapshots. This specific set of conditions was chosen based on 1) estimated temperatures generated after laser-heating of the sample and 2) the assumption that the timescale of the experiment is too short to allow for significant hydrodynamic evolution of the sample so that the density remains close to the initial density throughout the duration of the experiment.

The DFT spectral simulations were carried out for fully optimized, lowest energy structures of diamond and graphite and for a few snapshots from ChIMES MD trajectory of a-C system at 7000 K. For all these calculations, we have considered the Γ point of super cells. To account for the possible C 1s core hole relaxation effects on spectra, we have used the transition potential

method with the half core-hole (TPHH) approximation, and the results obtained were compared with ground state calculations (which excludes relaxation effects). Separate spectral simulations were performed for each carbon atom present in the a-C cell and only for inequivalent atoms in diamond and graphite cells. To facilitate easy comparison with experimental data, the discrete theoretical spectra were convoluted with normalized Gaussian function having broadening parameters (σ) of 0.8 and 1.0 eV for graphite and diamond, respectively. Furthermore, we rigidly shifted the XES of graphite and diamond by -0.5 and 1.2 eV to match the peaks of theoretical spectra with those of experiments.

In addition, we also study and characterize the influence of structural variations, both in long range as well as short (local) distortion, on the XAS/XES spectra, which will be useful for providing possible rationalization of the experimental data. For the purpose of the former, we have applied the tensile and compressive mechanical strains for both diamond and graphite cells by $\pm 10\%$. The XES spectra for diamond and graphite under mechanical strains (compressive (-10%) and tensile (+10%)) were calculated by changing the simulation cell parameters uniformly using fixed internal coordinates of the atoms.

In addition, we used the following procedure to model the local distortions. A C_5 unit of carbon atoms (a center carbon atom with 4 nearest neighbors) was selected in a $5 \times 5 \times 5$ supercell (1000 atoms) of diamond and the unit was allowed to move in the frozen diamond environment. From the phonon calculations, we have obtained 15 normal modes of vibration, and these were used to create local distortions with displacement amplitudes of 0.05 and 0.15 Bohr. Simulations of XES spectra for distortions along each vibrational mode were performed using the TPHH approximation at DFT level, and then compared to the XES spectra of the undistorted C_5 geometry. Spectral simulations based on molecular orbital and orbital energies from the TPHH method, instead of the electronic ground state, for both the XAS and XES spectra, allow for an accurate description of both absorption and emission energies and spectral shape.

6.4 Amorphous Carbon

Samples of a-C were first characterized by XAS, XES, RIXS, and XPS to provide a benchmark of the pristine targets. There are two salient features in the K-edge XAS spectrum: a pre-edge absorption at 285 eV and a broad absorption near 290 eV. The pre-edge absorption has been attributed to the excitation of core electrons into π^* states, while the broader feature represents excitation into σ^* states.^{14,30}

The emission spectra were taken with selected excitation energies: Before and after the pre-edge adsorption (284.8 and 287.7 eV), at the start of the broad feature (290.6 eV), and at the tail of the broad feature (308.9 eV), as shown in Figure 2a. The resulting XES/RIXS spectra have two main features, a peak centered at 278 eV and a high energy shoulder at 282 eV, attributed to the σ and π occupied orbitals, respectively.^{31,32} The XES spectrum of solid a-C can be qualitatively compared to that of graphite, which features sharper σ and π peaks. The peaks arise from the sigma bonds that form the hexagonal planes of graphite and the pi bonds which extend between layers which together form the sp^2 -hybridized carbon network, respectively. While the *peak positions* of the RIXS spectra depend only slightly on the excitation energy, (there are no obvious spectral shifts) the *intensities* of the features do depend on the excitation energy, indicating that the emission processes are dependent on the absorption process.³³ The spectra are in excellent

agreement with previously reported spectra of a-C and act as a reference to the tr-RIXS measurements discussed below.

The XPS spectrum can be deconvoluted to obtain the percentage of sp^2 and sp^3 character at the surface (probe depth ~ 3 nm), shown in Figure 2b. The peak at 285.2 eV represents sp^3 -bonded carbon atoms, and the area under the curve is used to calculate the sp^3 content percentage, which is ca. 26%. The binding energy peak at 284.3 corresponds to sp^2 carbon atoms and accounts for nearly double the percentage sp^3 content, resulting in a 2:1 sp^2/sp^3 ratio, agreeing with typical ratios determined for a-C samples with similar densities.³⁴

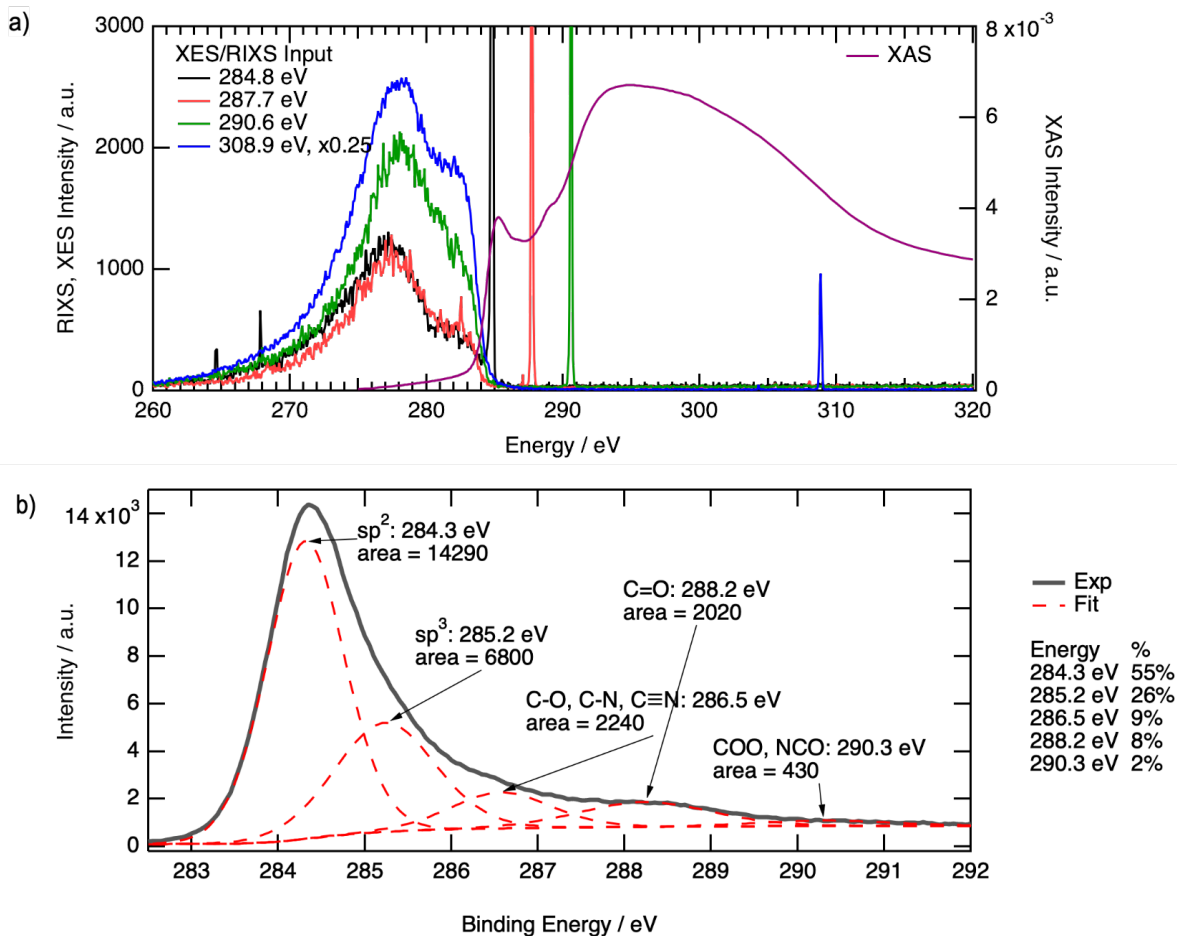


Figure 6.2. a) Carbon K -edge XES, RIXS, and XAS spectra of unmelted amorphous carbon film. The sharp peaks present in the RIXS and XES spectra are elastic scattering peaks. b) Deconvolution of X-ray photoelectron spectra of C 1s peaks of unmelted amorphous carbon. Peaks at 284.3 eV (FWHM 1.05 eV) and 285.2 eV (FWHM 1.37 eV) correspond to sp^2 - and sp^3 - carbon atoms. The sp^2/sp^3 ratio was calculated to be about 2.1.

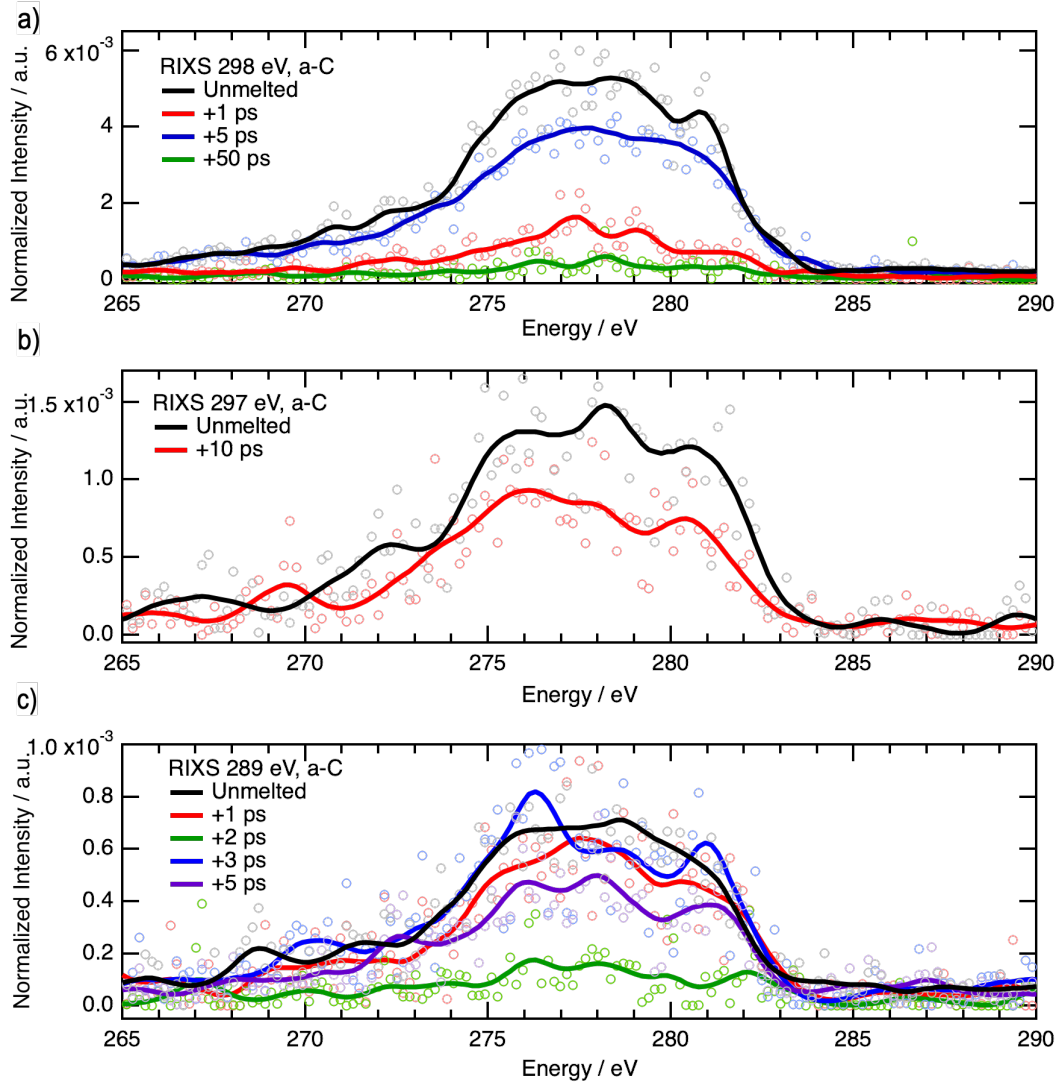


Figure 6.3. Tr-RIXS spectra of a-C at three input energies: (a) 298 eV, (b) 297 eV, and (c) 289 eV. Time delays between the melting pulse and the RIXs pulse varied between 1ps and 50ps. The spectra are filtered, normalized, and smoothed. The average FWHM of the spectra is 8.29 ± 0.18 eV.

Time-resolved RIXS spectra of the a-C samples were collected at 289 eV (near the XAS sp^2 transition), 297 eV, and 298 eV (near the broad XAS sp^3 transition) (Figure 6.3). The formation of liquid carbon should see an increase in intensity at 289 eV, indicative of increased sp^2 character, and a decay at 297 or 298 eV representing a loss of sp^3 character. To better discern changes in the RIXS intensity, the change in the integrated area of each spectrum was plotted as a function of delay time from the optical melting pulse. When utilizing excitation energies of 289 and 298 eV, a decay of ca. 75% in the initial RIXS signal was observed within 2 ps of the optical melting pulse. This decay is likely due to transition blocking, as the optical pulse causes the electrons in the valence band to occupy the conduction band states that the x-ray pulse would otherwise excite into, reducing the absorption of the incident x-ray energy, and consequently leading to an overall decreased emission signal.³⁵ After the initial decrease, there is a subsequent increase in the intensity of the spectra at 5 and 3 ps for 298 and 289 eV, respectively. Following the initial effects

of transition blocking on the emission spectra, we speculate that optically excited electrons relax and return to the valence band at these intermediate delay times, at which point much of the lost signal is regained. After 5 ps and beyond, we see the intensity decay across all probe energies. At longer time delays, it is likely that we are ablating the samples, as noted by Reitze et al. We therefore attribute the overall fluctuations seen in the intensity to relaxation and ablation of the sample.¹⁰ The solid lines in Figure 3 represent data that were averaged, normalized, and smoothed. We are not able to resolve the features observed in the transient tr-RIXS spectra; however, we can draw conclusions from the lack of peak broadening or narrowing. The widths of the emission spectra remain invariant at various incident energies and time delays (ca. 8 eV FWHM), with a standard deviation of less than 0.2 eV; moreover, there is no spectral blue or red shift, indicating little to no change in the electronic structure or bonding from the unmelted sample. This is further supported by theoretical modelling presented below, wherein the spectral differences induced by changes to the local environment are examined.

6.5 Ultrananocrystalline Diamond

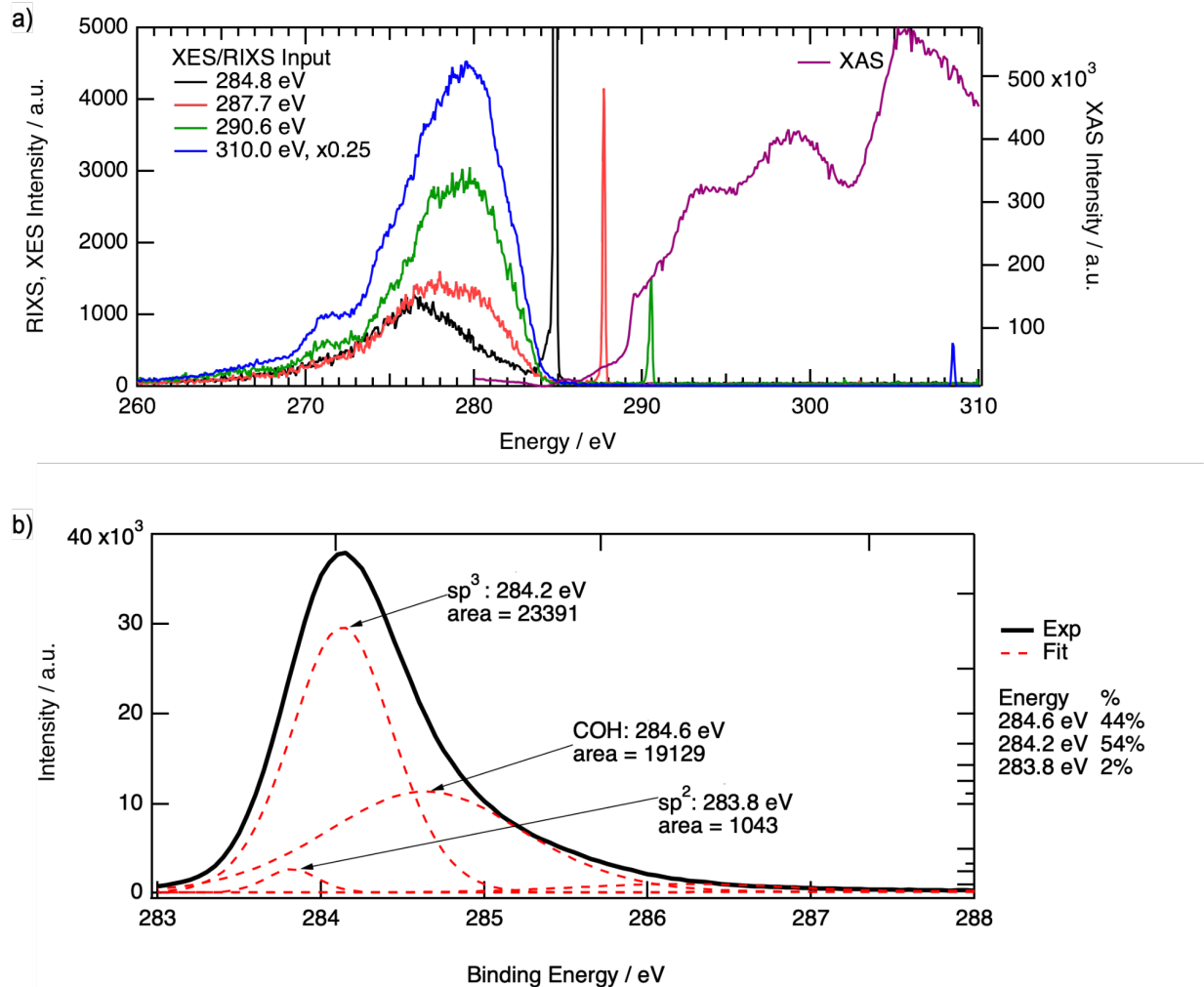


Figure 6.4. a) Carbon *K*-edge XES, RIXS, and XAS spectra of unmelted UNCD. The sharp peaks present in the RIXS and XES spectra are elastic scattering peaks. b) Deconvolution of X-ray photoelectron spectra of C 1s peaks of unmelted UNCD. Peaks at 283.8 eV and 284.2 eV correspond to sp²- and sp³ – carbon atoms. The sp³/sp² ratio was calculated to be about 22. The peak at 284.6 eV corresponds to carbon-hydroxyl (COH) groups in the near-surface region.

The suite of x-ray spectroscopies, XAS, XES, RIXS, and XPS, was also used to benchmark the unmelted UNCD thin films, as shown in Figure 6.4. The XAS spectrum of UNCD exhibits more features than a-C. A pronounced dip in the spectrum at 303 eV is indicative of the second band gap in the diamond band structure.³⁶ The shoulder at ca. 289 eV marks the C 1s core exciton resonance.³⁷ The broad features before the dip at 303 eV have been attributed to σ^* states of sp³ bonded carbon.³⁸

The XES spectra of UNCD exhibit a broad feature near 279 eV, and a lower energy shoulder near 272 eV, observed only at higher input energies (290.6 eV and 310 eV). The

intensities of these features are sensitive to the excitation energy. For example, the shoulder at 272 eV is nearly depleted at lower excitation energies of 284.8 and 287.7 eV, which correspond to the a-C K-edge. When we probe closer to features observed in the UNCD XAS (290.6 and 310 eV), the shoulder at 272 eV is prominent, indicating that we are observing emission from a path in the band structure unique to the sp^3 -dominant diamond structure. The peak near 277 eV is stronger for excitation energies preceding the K-edge, and substantially weaker for excitation energies beyond the K-edge. These changes in peak intensity can be used for band structure mapping; the main features in the XES and XAS spectra can be assigned to critical symmetry points of the band structure, as outlined in Ma et al.³³ For example, excitation energies near the K-edge may promote electrons to the X_1 point of the conduction band, because momentum is conserved in RIXS; a valence electron at the X_4 area will relax into the core hole. At excitation energies just beyond the K-edge (290.6 eV), the absorption is assigned to the promotion of an electron to the K_3 point in the conduction band. The most energetically favorable relaxation is to the K_2 point of the valence band, which is assigned to energies near 280 eV.³³ As a result, we observe more intensity around 280 eV than in the 290.6 eV excited RIXS spectra (green line, Figure 6.4 (a)). The spectra are in excellent agreement with previously reported spectra of diamond and act as a reference to the tr-RIXS measurements discussed later.

Peaks in the XPS spectrum (Figure 6.4 (b)) of UNCD were fit to obtain a sp^3 carbon content percent of 53.7 with only 2.4% of the carbon being sp^2 hybridized, giving a sp^3/sp^2 ratio of 22.4, and indicating that the sample is overwhelmingly 'diamond-like.' However, there is a large contribution from C-O-H in the near-surface region probed by XPS (284.6 eV), which is likely from surface termination and grain boundaries.³⁹ The grain boundaries of nanocrystalline diamond will contain sp^2 -carbon, defects, and hydrogen, so the XPS spectrum is not expected to exactly match that of a pristine diamond crystal.⁴⁰ This should not have a significant effect on the bulk-sensitive XAS, XES and RIXS measurements.

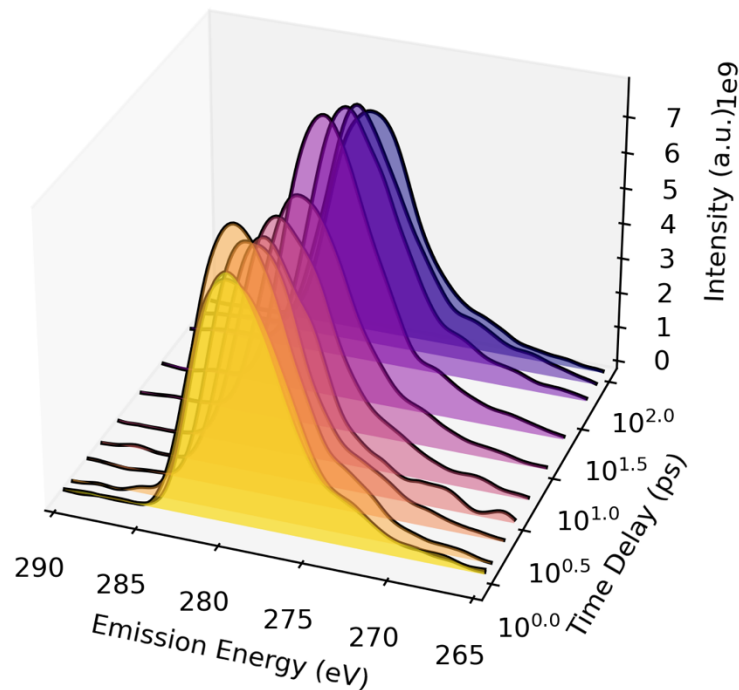


Figure 6.5. tr-XES spectra of UNCD at 308 eV. Spectral changes are very minor across all time delays.

Time-resolved XES spectra from UNCD films were collected at 308 eV, beyond the second band gap in diamond (Figure 6.5). Changes in the tr-XES spectra of UNCD are not as apparent as those observed in a-C, because of the thickness of the UNCD films (4 times thicker than a-C samples), leading to a mismatch between pump and probe depth, i.e. not all the sample was melted. The normalized integrated intensities of the tr-XES spectra were plotted as a function of delay time to show the fluctuations more clearly (Figure 6.6). The intensity of the XES increases within the first 0.5 ps by 25% and then slowly returns to the initial intensity 3 ps after the melting pulse. The intensity fluctuates, changing by less than 3% between 3 and 10 ps after the melting pulse. From 10 - 20 ps, the signal increases again, reaching an intensity about 18% greater than that at $t = 0$ ps. From 20 ps onward, the XES intensity slowly decays, dipping below the initial intensity after >80 ps. The overall loss in intensity was only 3%, less than the change of intensity between negative delay times and 0 ps (4.8%). This indicates that changes to the intensity that are less than about 5% are most likely negligible and cannot be separated from changes in the intensity resulting from instrumental noise. As such, the fluctuations observed from 3 ps to 10 ps cannot be separated readily from experimental noise. Our discussion will instead focus on the larger changes in intensity which occurred at 0.5 ps and 20 ps after the optical melting pulse. The increase in intensity at 0.5 ps may indicate that some change to the XES spectra was induced by the melting pulse, however; the change must only affect the intensity of the XES spectra at 308 eV and not induce changes to the peaks position or width. This eliminates most structural changes that might occur if the sample were to be forming a liquid state. The normal mode analysis performed on the C_5 unit within the diamond lattice shows that vibrational distortions, such as C-C symmetrical stretching or bending can be responsible for oscillations in the intensity of the XES spectra.

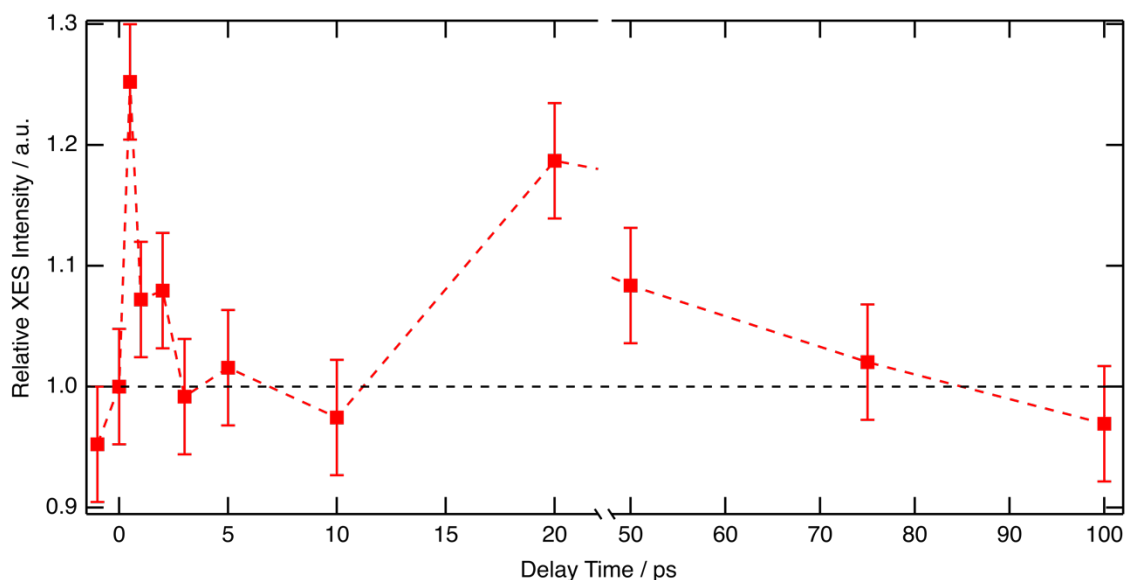


Figure 6.6. The intensity of the integrated UNCD emission spectrum as a function of delay time after the optical melting pulse. Error bars represent experimental noise.

While in this experiment, the increase in signal is not preceded by a decrease, which often represents the onset of sample ablation, it is valuable to remember that not all the sample is melted due to the thickness of the UNCD films, and unmelted sample will be contributing to the signal even after ablation. This means that at long times, when ablation has occurred, the signal will represent unmelted sample as well as whatever structures remain following the ablation. Interestingly, since another increase in signal is observed at a delay time of 20 ps, recovery in signal can be attributed to the formation of new structures, such as nanoscale structures in the ablation plume, previously described by the ultrafast grazing incidence X-ray scattering of laser-ablated silicon measured by Hull et al.⁴¹ Those measurements showed the formation of nanoscale inhomogeneities, reminiscent of nanoparticle structures 20 ps after non-thermal melting.⁴¹

Tr-RIXS spectra of UNCD were collected at incidence energies of 294 and 303 eV (Figure 6.7). At both energies the relative RIXS energy increases with increasing delay time from the melting pulse. At 294 eV, the increase follows a decrease in the short-time regime. This initial decrease (before 2 ps) may again be attributed to transition blocking. The resulting tr-RIXS spectra don't show a decrease in signal relative to unmelted UNCD. Again, the increase in signal within a 20 ps delay time can be attributed to the formation of new structures, as the sample expands, cools, and ablates and considering that the sample is still thick enough to absorb all the X-rays after ablation.

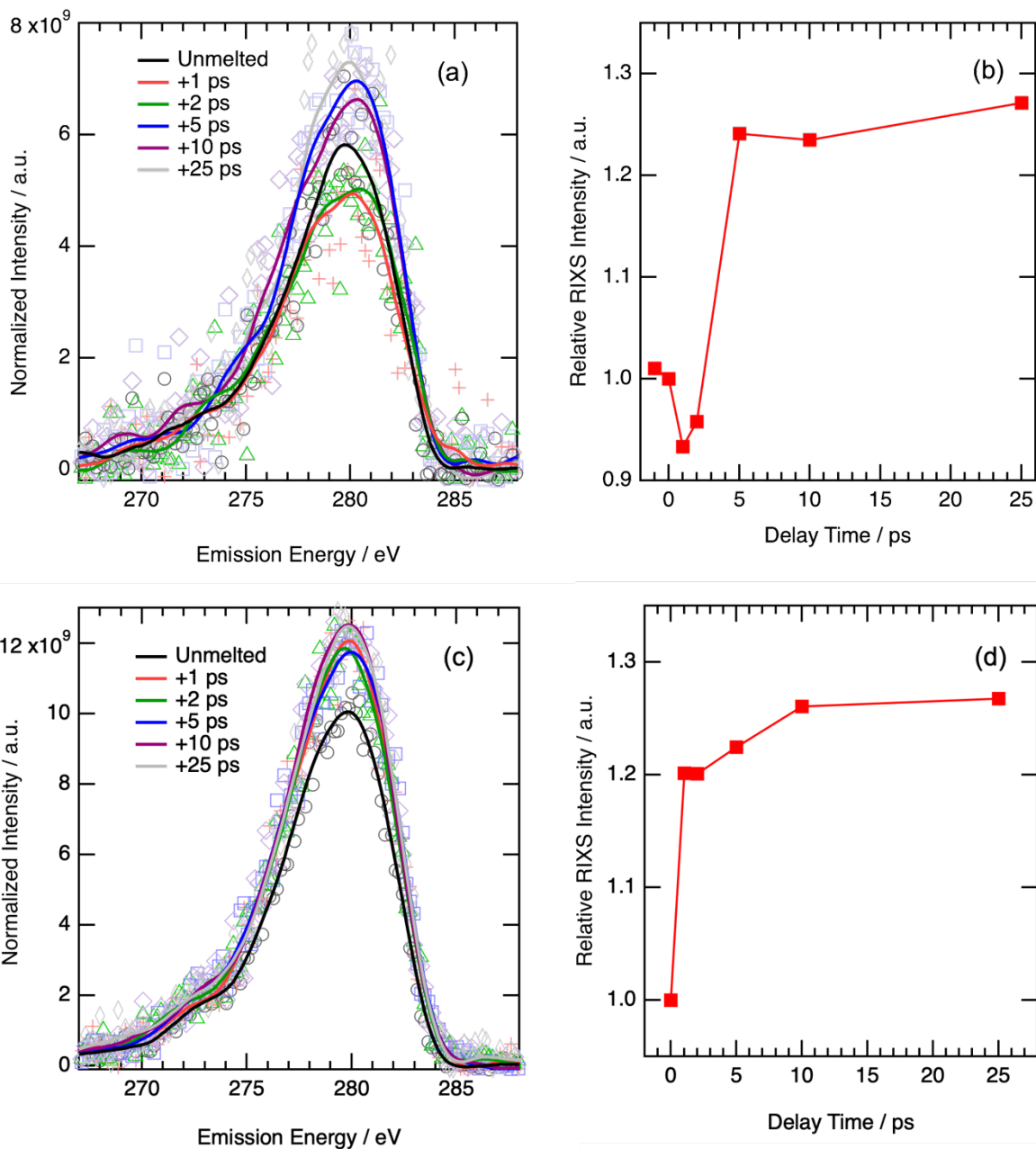


Figure 6.7. tr-RIXS spectra of the unmelted UNCD films and the signal from the sample after varying delay times at input energy of (a) 294 eV and (b) 303 eV. The intensity of the integrated UNCD emission spectra as a function of delay time is also shown to exemplify the plateau in signal following an initial decrease when using an excitation energy of 303 eV (d) and the sharp increase and plateau when using a higher energy excitation of 294 eV (b).

6.6 Theory Results

Carbon K-edge x-ray absorption spectra (XAS) (Figure 6.8) and emission spectra (XES) (Figure 6.9) were simulated for diamond, graphite, and amorphous carbon from the MD trajectories at 7000 K. A cutoff radius of 1.6 Å was used to separate the spectral contributions

based on local geometry (coordination) of the core-excited atom. Figure 8 shows that with increasing coordination number (number of neighbors), the main peak of the spectrum undergoes a blue shift. Furthermore, the average spectrum, representing the average of all atoms in the MD snapshot, is dominated by contributions from doubly-coordinated carbon atoms, consistent with the coordination expected in a liquid. However, the experimental amorphous carbon (a-C) spectrum is best reproduced by 3- and 4- coordinated carbon. This indicates that the experimental XAS of a-C is predominantly sp^2 and sp^3 hybridized. We would expect samples heated to 7000 K to have spectra similar to the doubly-coordinated XAS (green line).

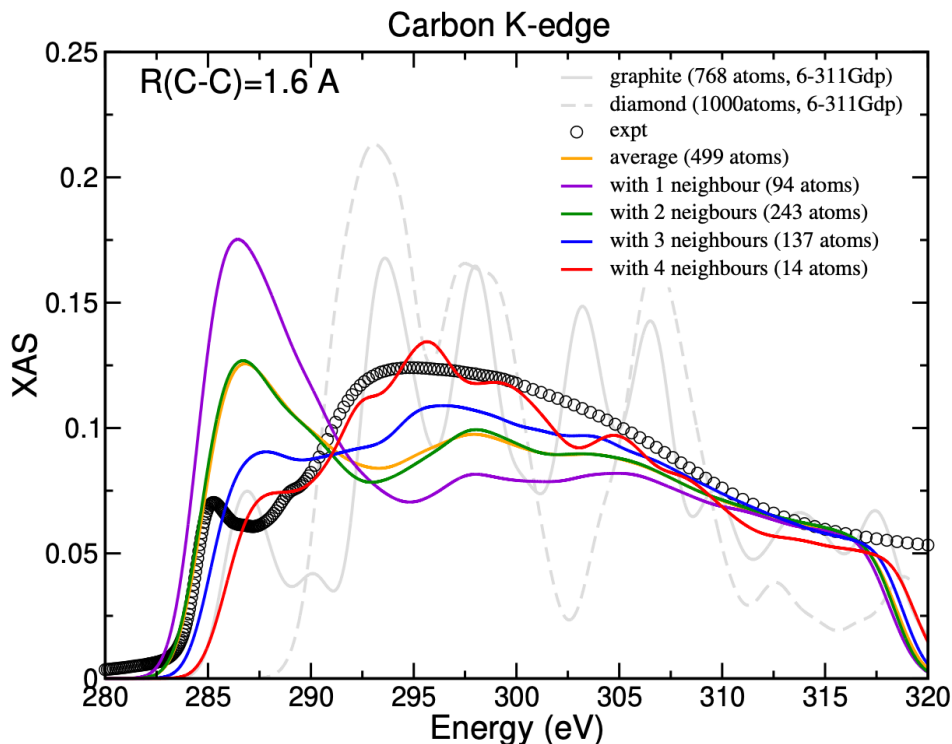


Figure 6.8. The experimental Carbon K-edge spectra of amorphous carbon is compared to the modeled XAS spectra of the carbon K-edge. A cutoff radius of 1.6 \AA is used to find the neighbors. The calculated spectra for graphite and diamond are supplied for comparison.

Similarly, the modeled XES spectra is separated by coordination number of the core-excited atom in Figure 6.9. In contrast to the XAS spectra presented above, the XES spectra undergo a red shift with increasing coordination number but show that the average spectrum is still dominated by contributions from doubly-coordinated carbon. While the 3- and 4- coordinated spectra are once again a better match to the experimental data, they resemble the calculated spectra under compressive strain (-10%) depicted in Figure 6.10.

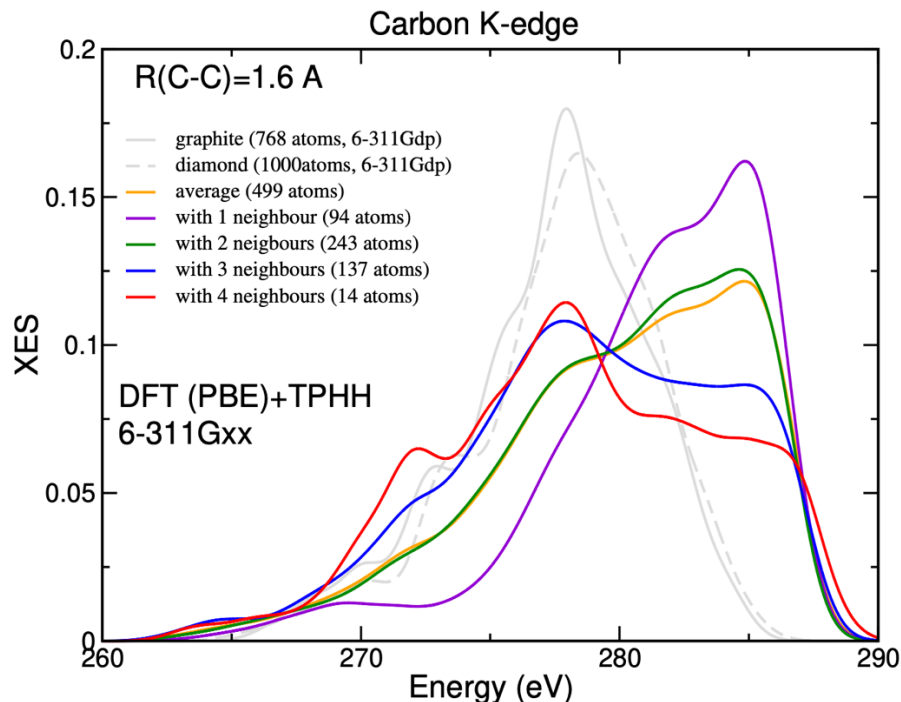


Figure 6.9. Carbon K-edge XES are categorized into different groups based on number of nearest neighbors of core excited atom. The cutoff radius of 1.6 Å has been used to find the neighbors.

To better understand and augment the experimental results, we have also carried out DFT based electronic structure calculations at the GGA (PBE) level to simulate the XES spectra for graphite and diamond using both ground state Kohn-Sham orbitals (GND) and transition potential with half-core holes (TPHH) methods, for which results are presented in Figure 6.10 (solid lines). It is clear that DFT calculations with the TPHH method produced spectra comparable to experiment, capturing the overall spectral features of graphite and diamond.

Since the melting pulse is expected to cause a structural change in the carbon samples and XES is sensitive to both the long and short (local) distance changes in the environment, additional TPHH calculations incorporating mechanical strain, both compressive and tensile, were performed. The resulting spectra demonstrate that both graphite and diamond experience a spectral red shift and broadening under compressive strain (-10%) and a spectral blue shift and narrowing under tensile strain (+10%) (Figure 6.10). These shifts are $> 1\text{eV}$ and should be easily observable with the reported XES/RIXS resolution of at least 0.6 eV within 200-1200 eV.¹⁸ While the TPHH calculated spectra capture the unmelted samples well, they indicate spectral shifts-broadening, or narrowing-that are not observed at $t > 0$ ps in the experimental data, and therefore do not represent the observed transient RIXS and XES results.

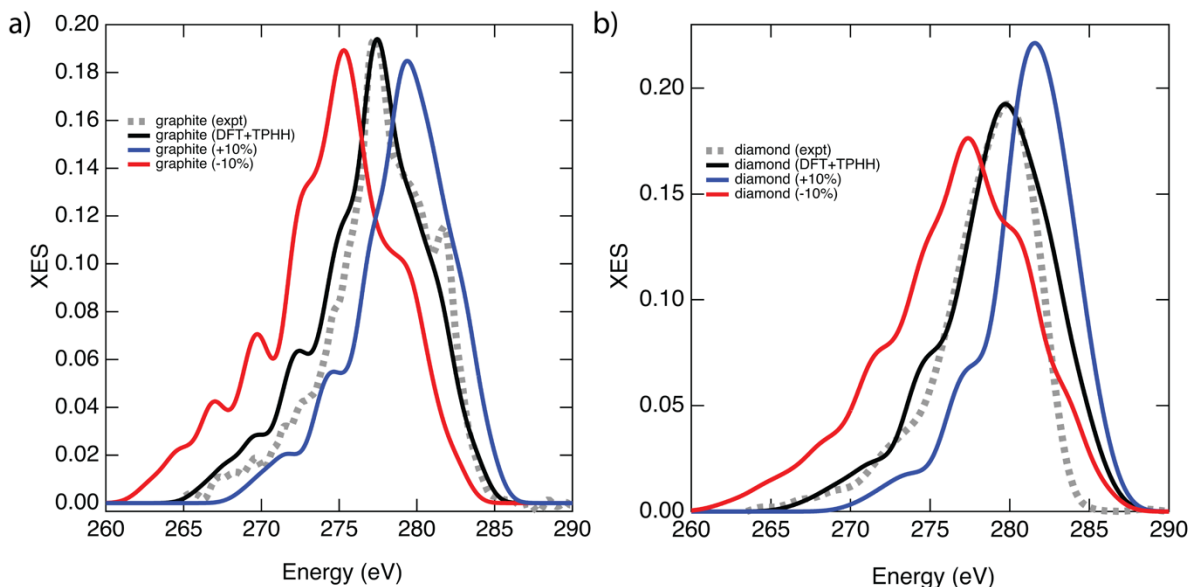


Figure 6.10. Resulting XES spectra for (a) graphite and (b) diamond at 308 eV with theoretical modelling of applied mechanical strains. Under tensile strain the spectra narrow and undergo a blue shift. Under compressive strain the spectra broaden and undergo a red shift. PBE XC functional along with 6-311 GXX basis set was used for the modeled spectra. All modeled spectra are shifted by -0.5 eV and 1.2 eV for graphite and diamond, respectively.

In attempts to explain the intensity fluctuations observed in the transient spectra, we also perform the spectral simulations for a diamond cell with local distortions, which were based on normal modes of vibrations around a carbon atom with its first nearest neighbor (forming C_5 unit). XES spectra are sensitive to local structure, so localized distortions were applied along each of the 15 identified modes (Figure 6.11). Modes 10-12 had the strongest response, corresponding to the C-C-C symmetrical bend and C-C symmetrical stretch vibrations. The difference XES spectra show the change in intensity as a function of energy between the undistorted and distorted C_5 unit (Figure 6.12). Modes 10-12 show an obvious decrease in signal from 265-280 eV and an increase from 280-285 eV, which may explain the intensity variation observed in the experimental data. The spectral response due to the remaining modes (1-9, 13-15) is very small. To further verify the dependence of spectral response with the amplitude of the normal mode displacements, we have also carried out similar XES simulations with an increased amplitude of 0.15 Bohr. The difference XES for these three modes show intensity nearly three times of those obtained for 0.05 Bohr. Thus, the local distortion-based normal modes show a nearly flat response in the difference spectra, indicating they are not responsible for the observed experimental intensity fluctuations.

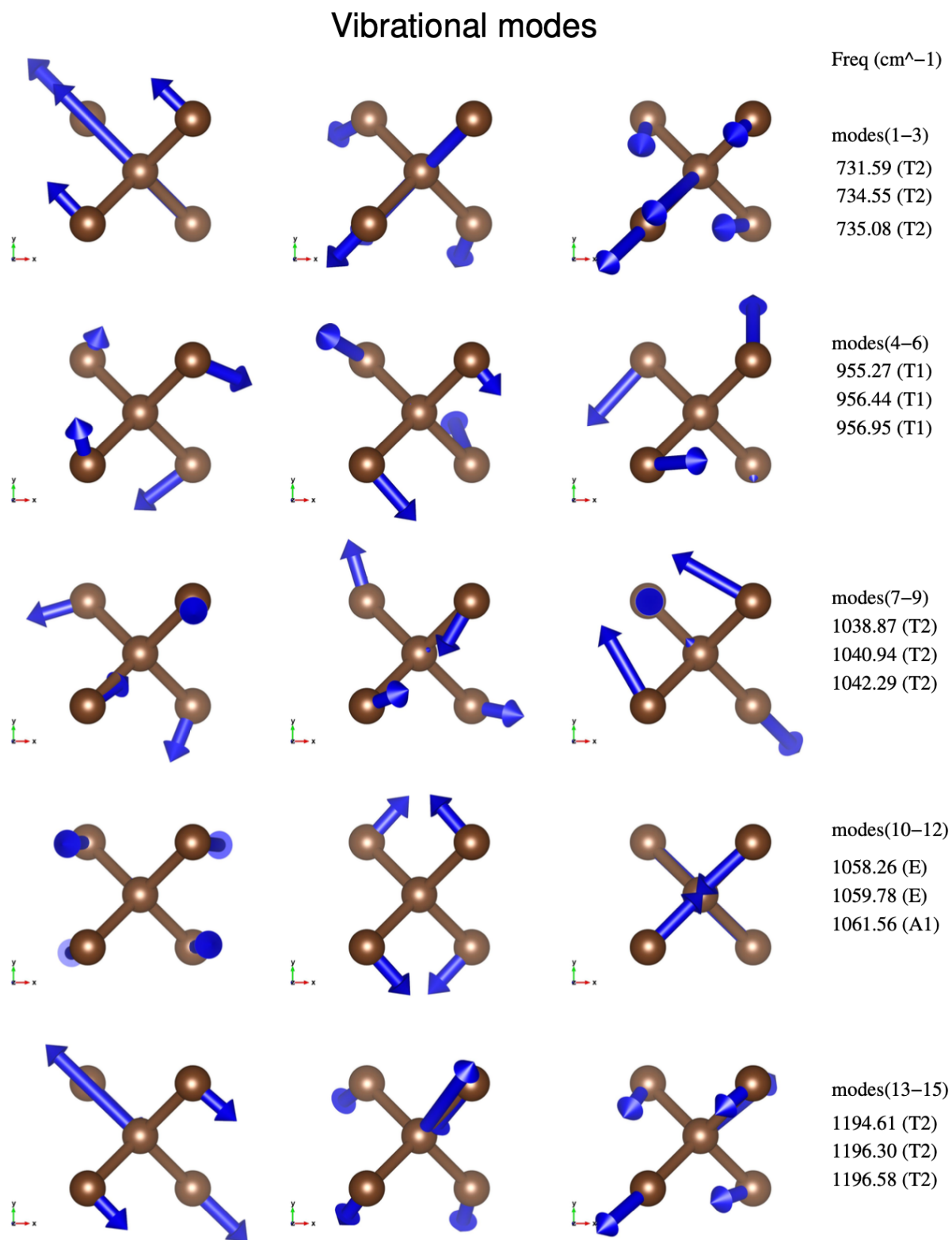


Figure 6.11: Normal modes of vibration for a C₅ unit inside a frozen environment of diamond.

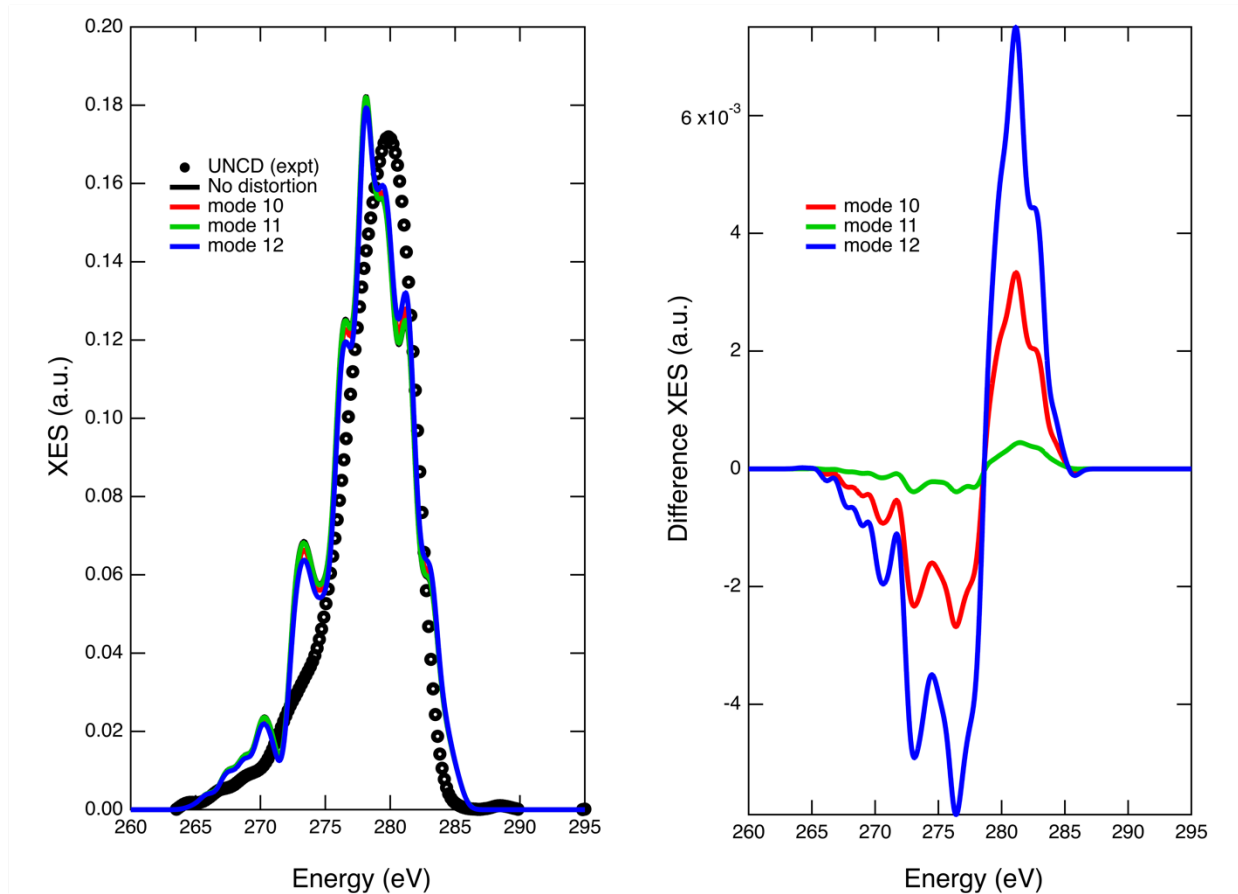


Figure 6.12. Calculated XES spectra following distortion of different normal modes with an amplitude of displacement. Modes 10-12 are expected to have the strongest XES spectral response and represent C-C-C symmetrical bending and C-C symmetrical stretching vibrations.

Comparing the theoretical spectra to the experimental results, it appears that we did not actually measure spectra of liquid carbon in the experiments. The improved agreement between spectral simulations based on higher (3 or 4-fold) coordination and normal mode analysis indicates that the carbon in the experiments exists in a crystalline or nano-crystalline state.

6.7 Conclusions

Tr-RIXS and tr-XES spectra of laser-melted carbon were measured for a-C and UNCD thin film samples at PAL-XFEL with intent to provide insight into the liquid structure of carbon. Utilizing time resolved techniques (RIXS and XES) that directly probe the electronic structure, we aimed to determine the dependence of the liquid state on temperature, pressure, and density by scanning at different delay times. By comparing our time-resolved measurements to benchmark measurements of the unmelted samples performed with a suite of x-ray spectroscopies, we find no evidence of changes to the electronic structure. Decreases in the time-resolved intensities for a-C and UNCD are attributed to transition blocking, subsequent relaxation, and eventual ablation of the samples. Additionally, comparison of experimental results to spectra calculated from MD trajectories at 7000 K shows that the experimental spectra resemble 3,4 – coordinated carbon, rather than the doubly-coordinated carbon dominant in the simulations. Normal mode analysis,

which shows that vibrational stretching and bending modes of the diamond lattice result in changes in intensity in the XES spectra, provided evidence for the small fluctuations in intensity observed in the experimental data. For UNCD, while the signal never dipped below that measured at $t = 0$ ps, most likely due to the greater thickness of the samples used, while increases in signal at 20 ps may be indicative of the formation of nanoscale structures formed the ablation plume. No changes to the peak position or shape were observed, making it highly unlikely that any changes to the electronic structure occurred within our temporal resolution. As such, we conclude that no obvious changes occur to the electronic structure of the studied carbon samples, and that the samples appear to be in a crystalline state following an optical melting pulse under the specified conditions.

References

- (1) Hull, C. J.; Raj, S. L.; Saykally, R. J. The Liquid State of Carbon. *Chem. Phys. Lett.* **2020**, *749*, 137341. <https://doi.org/10.1016/j.cplett.2020.137341>.
- (2) Types of Nuclear Reactors. In *Nuclear Energy: Principles, Practices, and Prospects*; Bodansky, D., Ed.; Springer New York: New York, NY, 2005; pp 171–192. https://doi.org/10.1007/0-387-26931-2_8.
- (3) *Lithium-Ion Batteries: Science and Technologies*; Yoshio, M., Brodd, R. J., Kozawa, A., Eds.; Springer New York: New York, NY, 2009. <https://doi.org/10.1007/978-0-387-34445-4>.
- (4) Zhang, Z.; Simionesie, D.; Schaschke, C. Graphite and Hybrid Nanomaterials as Lubricant Additives. *Lubricants* **2014**, *2* (2), 44–65. <https://doi.org/10.3390/lubricants2020044>.
- (5) De Heer, W. A.; Poncharal, P.; Berger, C.; Gezo, J.; Song, Z.; Bettini, J.; Ugarte, D. Liquid Carbon, Carbon-Glass Beads, and the Crystallization of Carbon Nanotubes. *Science* **2005**, *307* (5711), 907–910. <https://doi.org/10.1126/science.1107035>.
- (6) Narayan, J.; Bhaumik, A. Novel Phase of Carbon, Ferromagnetism, and Conversion into Diamond. *J. Appl. Phys.* **2015**, *118* (21), 215303. <https://doi.org/10.1063/1.4936595>.
- (7) Gorrini, F.; Cazzanelli, M.; Bazzanella, N.; Edla, R.; Gemmi, M.; Cappello, V.; David, J.; Dorigoni, C.; Bifone, A.; Miotello, A. On the Thermodynamic Path Enabling a Room-Temperature, Laser-Assisted Graphite to Nanodiamond Transformation. *Sci. Rep.* **2016**, *6* (1), 35244. <https://doi.org/10.1038/srep35244>.
- (8) Bhaumik, A.; Sachan, R.; Narayan, J. High-Temperature Superconductivity in Boron-Doped Q-Carbon. *ACS Nano* **2017**, *11* (6), 5351–5357. <https://doi.org/10.1021/acsnano.7b01294>.
- (9) Malvezzi, A. M.; Bloembergen, N.; Huang, C. Y. Time-Resolved Picosecond Optical Measurements of Laser-Excited Graphite. *Phys. Rev. Lett.* **1986**, *57* (1), 146–149. <https://doi.org/10.1103/PhysRevLett.57.146>.
- (10) Reitze, D. H.; Wang, X.; Ahn, H.; Downer, M. C. Femtosecond Laser Melting of Graphite. *Phys. Rev. B* **1989**, *40* (17), 11986–11989. <https://doi.org/10.1103/PhysRevB.40.11986>.
- (11) Malvezzi, A. M.; Romanoni, M. The Optical Properties of Graphite under Intense Picosecond Laser Illumination. *Int. J. Thermophys.* **1992**, *13* (1), 131–140. <https://doi.org/10.1007/BF00503361>.
- (12) Reitze, D. H.; Ahn, H.; Downer, M. C. Optical Properties of Liquid Carbon Measured by Femtosecond Spectroscopy. *Phys. Rev. B* **1992**, *45* (6), 2677–2693. <https://doi.org/10.1103/PhysRevB.45.2677>.
- (13) Mincigrucci, R.; Principi, E.; Bencivenga, F.; Foglia, L.; Gessini, A.; Kurdi, G.; Simoncig, A.; Masciovecchio, C. Transient EUV Reflectivity Measurements of Carbon upon Ultrafast Laser Heating. *Photonics* **2017**, *4* (4), 23. <https://doi.org/10.3390/photonics4020023>.

- (14) Johnson, S. L.; Heimann, P. A.; MacPhee, A. G.; Lindenberg, A. M.; Monteiro, O. R.; Chang, Z.; Lee, R. W.; Falcone, R. W. Bonding in Liquid Carbon Studied by Time-Resolved X-Ray Absorption Spectroscopy. *Phys. Rev. Lett.* **2005**, *94* (5), 057407. <https://doi.org/10.1103/PhysRevLett.94.057407>.
- (15) Principi, E.; Krylow, S.; Garcia, M. E.; Simoncig, A.; Foglia, L.; Mincigrucchi, R.; Kurdi, G.; Gessini, A.; Bencivenga, F.; Giglia, A.; et al. Atomic and Electronic Structure of Solid-Density Liquid Carbon. *Phys. Rev. Lett.* **2020**, *125* (15), 155703. <https://doi.org/10.1103/PhysRevLett.125.155703>.
- (16) Raj, S.; Devlin, S.; Mincigrucchi, R.; Schwartz, C.; Principi, E.; Bencivenga, F.; Foglia, L.; Gessini, A.; Simoncig, A.; Kurdi, G.; et al. Free Electron Laser Measurement of Liquid Carbon Reflectivity in the Extreme Ultraviolet. *Photonics* **2020**, *7* (2), 35. <https://doi.org/10.3390/photonics7020035>.
- (17) Brown, C. R. D.; Gericke, D. O.; Cammarata, M.; Cho, B. I.; Döppner, T.; Engelhorn, K.; Förster, E.; Fortmann, C.; Fritz, D.; Galtier, E.; et al. Evidence for a Glassy State in Strongly Driven Carbon. *Sci. Rep.* **2014**, *4* (1), 5214. <https://doi.org/10.1038/srep05214>.
- (18) Park, S. H.; Yoon, J.; Kim, C.; Hwang, C.; Kim, D.-H.; Lee, S.-H.; Kwon, S. Scientific Instruments for Soft X-Ray Photon-in/Photon-out Spectroscopy on the PAL-XFEL. *J. Synchrotron Radiat.* **2019**, *26* (4), 1031–1036. <https://doi.org/10.1107/S1600577519004272>.
- (19) Gallo, P.; Amann-Winkel, K.; Angell, C. A.; Anisimov, M. A.; Caupin, F.; Chakravarty, C.; Lascaris, E.; Loerting, T.; Panagiotopoulos, A. Z.; Russo, J.; et al. Water: A Tale of Two Liquids. *Chem. Rev.* **2016**, *116* (13), 7463–7500. <https://doi.org/10.1021/acs.chemrev.5b00750>.
- (20) Beye, M.; Sorgenfrei, F.; Schlotter, W. F.; Wurth, W.; Föhlisch, A. The Liquid-Liquid Phase Transition in Silicon Revealed by Snapshots of Valence Electrons. *Proc. Natl. Acad. Sci.* **2010**, *107* (39), 16772–16776. <https://doi.org/10.1073/pnas.1006499107>.
- (21) Nowak, S. H.; Armenta, R.; Schwartz, C. P.; Gallo, A.; Abraham, B.; Garcia-Esparza, A. T.; Biasin, E.; Prado, A.; Maciel, A.; Zhang, D.; et al. A Versatile Johansson-Type Tender x-Ray Emission Spectrometer. *Rev. Sci. Instrum.* **2020**, *91* (3), 033101. <https://doi.org/10.1063/1.5121853>.
- (22) Tirsell, K. G.; Karpenko, V. P. A General Purpose Sub-keV X-Ray Facility at the Stanford Synchrotron Radiation Laboratory. *Nucl. Instrum. Methods Phys. Res. Sect. Accel. Spectrometers Detect. Assoc. Equip.* **1990**, *291* (1–2), 511–517. [https://doi.org/10.1016/0168-9002\(90\)90113-K](https://doi.org/10.1016/0168-9002(90)90113-K).
- (23) Qiao, R.; Li, Q.; Zhuo, Z.; Sallis, S.; Fuchs, O.; Blum, M.; Weinhardt, L.; Heske, C.; Pepper, J.; Jones, M.; et al. High-Efficiency *In Situ* Resonant Inelastic x-Ray Scattering (iRIXS) Endstation at the Advanced Light Source. *Rev. Sci. Instrum.* **2017**, *88* (3), 033106. <https://doi.org/10.1063/1.4977592>.
- (24) Wiesenfeld, J. M.; Stone, J.; Marcuse, D.; Burrus, C. A.; Yang, S. Temperature Dependence of Hydroxyl Formation in the Reaction of Hydrogen with Silica Glass. *J. Appl. Phys.* **1987**, *61* (12), 5447–5454. <https://doi.org/10.1063/1.338234>.
- (25) Hutter, J.; Iannuzzi, M.; Schiffmann, F.; VandeVondele, J. Cp2k: Atomistic Simulations of Condensed Matter Systems. *Wiley Interdiscip. Rev. Comput. Mol. Sci.* **2014**, *4* (1), 15–25. <https://doi.org/10.1002/wcms.1159>.
- (26) Thompson, A. P.; Aktulga, H. M.; Berger, R.; Bolintineanu, D. S.; Brown, W. M.; Crozier, P. S.; In 'T Veld, P. J.; Kohlmeyer, A.; Moore, S. G.; Nguyen, T. D.; et al. LAMMPS - a Flexible Simulation Tool for Particle-Based Materials Modeling at the Atomic, Meso, and

- Continuum Scales. *Comput. Phys. Commun.* **2022**, *271*, 108171.
<https://doi.org/10.1016/j.cpc.2021.108171>.
- (27) Lindsey, R. K.; Fried, L. E.; Goldman, N. ChIMES: A Force Matched Potential with Explicit Three-Body Interactions for Molten Carbon. *J. Chem. Theory Comput.* **2017**, *13* (12), 6222–6229. <https://doi.org/10.1021/acs.jctc.7b00867>.
- (28) Kohn, W.; Sham, L. J. Self-Consistent Equations Including Exchange and Correlation Effects. *Phys. Rev.* **1965**, *140* (4A), A1133–A1138.
<https://doi.org/10.1103/PhysRev.140.A1133>.
- (29) Lindsey, R.; Bastea, S.; Hamel, S.; Lyu, Y.; Goldman, N.; Lordi, V. ChIMES Carbon 2.0: A Transferable Machine-Learned Interatomic Model Harnessing Multifidelity Training Data. March 26, 2024. <https://doi.org/10.26434/chemrxiv-2024-s1fs5-v2>.
- (30) Díaz, J.; Anders, S.; Zhou, X.; Moler, E. J.; Kellar, S. A.; Hussain, Z. Analysis of the π^* and σ^* Bands of the X-Ray Absorption Spectrum of Amorphous Carbon. *Phys. Rev. B* **2001**, *64* (12), 125204. <https://doi.org/10.1103/PhysRevB.64.125204>.
- (31) Muramatsu, Y.; Hirono, S.; Umemura, S.; Ueno, Y.; Hayashi, T.; Grush, M. M.; Gullikson, E. M.; Perera, R. C. C. Soft X-Ray Emission and Absorption Spectra in the C K Region of Sputtered Amorphous Carbon Films. *Carbon* **2001**, *39* (9), 1403–1407.
[https://doi.org/10.1016/S0008-6223\(00\)00260-8](https://doi.org/10.1016/S0008-6223(00)00260-8).
- (32) Abrasonis, G.; Berndt, M.; Krause, M.; Kuepper, K.; Munnik, F.; Kolitsch, A.; Möller, W. Soft X-Ray Absorption and Emission Spectroscopic Investigation of Carbon and Carbon:Transition Metal Composite Films. *J. Phys. Chem. C* **2008**, *112* (44), 17161–17170.
<https://doi.org/10.1021/jp805209r>.
- (33) Ma, Y.; Wassdahl, N.; Skytt, P.; Guo, J.; Nordgren, J.; Johnson, P. D.; Rubensson, J.-E.; Boske, T.; Eberhardt, W.; Kevan, S. D. Soft-x-Ray Resonant Inelastic Scattering at the C K Edge of Diamond. *Phys. Rev. Lett.* **1992**, *69* (17), 2598–2601.
<https://doi.org/10.1103/PhysRevLett.69.2598>.
- (34) Haerle, R.; Riedo, E.; Pasquarello, A.; Baldereschi, A. sp^2/sp^3 Hybridization Ratio in Amorphous Carbon from C 1s Core-Level Shifts: X-Ray Photoelectron Spectroscopy and First-Principles Calculation. *Phys. Rev. B* **2001**, *65* (4), 045101.
<https://doi.org/10.1103/PhysRevB.65.045101>.
- (35) De Vos, E. W.; Neb, S.; Niedermayr, A.; Burri, F.; Hollm, M.; Gallmann, L.; Keller, U. Ultrafast Transition from State-Blocking Dynamics to Electron Localization in Transition Metal β -Tungsten. *Phys. Rev. Lett.* **2023**, *131* (22), 226901.
<https://doi.org/10.1103/PhysRevLett.131.226901>.
- (36) García, M. M.; Jiménez, I.; Vázquez, L.; Gómez-Aleixandre, C.; Albella, J. M.; Sánchez, O.; Terminello, L. J.; Himpsel, F. J. X-Ray Absorption Spectroscopy and Atomic Force Microscopy Study of Bias-Enhanced Nucleation of Diamond Films. *Appl. Phys. Lett.* **1998**, *72* (17), 2105–2107. <https://doi.org/10.1063/1.121290>.
- (37) Morar, J. F.; Himpsel, F. J.; Hollinger, G.; Hughes, G.; Jordan, J. L. Observation of a C- 1s Core Exciton in Diamond. *Phys. Rev. Lett.* **1985**, *54* (17), 1960–1963.
<https://doi.org/10.1103/PhysRevLett.54.1960>.
- (38) Chang, Y. K.; Hsieh, H. H.; Pong, W. F.; Tsai, M.-H.; Lee, K. H.; Dann, T. E.; Chien, F. Z.; Tseng, P. K.; Tsang, K. L.; Su, W. K.; et al. Electronic and Atomic Structures of the Si-C-N Thin Film by x-Ray-Absorption Spectroscopy and Theoretical Calculations. *Phys. Rev. B* **1998**, *58* (14), 9018–9024. <https://doi.org/10.1103/PhysRevB.58.9018>.

- (39) Kumar, N.; Kozakov, A. T.; Dash, S.; Tyagi, A. K.; Lin, I. N. Microstructure, Chemical Bonds, and Friction Properties of Nanocrystalline Diamond Films Deposited in Two Different Plasma Media. *Phys. Solid State* **2013**, *55* (10), 2076–2087. <https://doi.org/10.1134/S1063783413100181>.
- (40) Walter, M.; Mangolini, F.; McClimon, J. B.; Carpick, R. W.; Moseler, M. Fermi Level Pinning by Defects Can Explain the Large Reported Carbon 1s Binding Energy Variations in Diamond.
- (41) Hull, C.; Raj, S.; Lam, R.; Katayama, T.; Pascal, T.; Drisdell, W. S.; Saykally, R.; Schwartz, C. P. Early Time Dynamics of Laser-Ablated Silicon Using Ultrafast Grazing Incidence X-Ray Scattering. *Chem. Phys. Lett.* **2019**, *736*, 136811. <https://doi.org/10.1016/j.cplett.2019.136811>.

